

**Spontaneous emission within wavelength-scale
microstructures**

Submitted by
Jonathan Arthur Edward Wasey

to the University of Exeter
as a thesis for the degree
of Doctor of Philosophy
in Physics

June 2001

This thesis is available for Library use on the understanding that it is copyright material and that no quotation from the thesis may be published without proper acknowledgement.

I certify that all material in this thesis which is not my own work has been identified and that no material has previously been submitted and approved for the award of a degree by this or any other University.

Abstract

The behaviour of an emitter can be drastically altered by placing it in a structure that is on a scale comparable to the wavelength of the emission. Both the spontaneous emission rate and the spatial distribution of the emitted radiation can be modified in this manner. This modification of the spontaneous emission of an emitter has major applications in devices such as light emitting diodes (LEDs). This thesis focuses on methods for determining the efficiency of emission of light from such devices and methods for increasing this efficiency.

Conjugated polymers are frequently used as the emissive material in optical devices such as the LED. As such, we focus our attention on parameters appropriate for organic microcavity LED structures. We investigate how well different microcavity structures perform in controlling emission from sources within them. In particular, we consider the use of either metals or dielectric Bragg stack reflectors as the partially transmitting mirror in a cavity LED.

Thin films of emissive polymers often have significant optical birefringence. We establish a suitable model for radiative emission from such birefringent films and successfully compare it with experimental data. The effects of the orientation of the dipole moment and birefringence upon the emission from films of polymer material are thereby calculated.

We extend our study beyond the efficiency of emission from planar structures with an assessment of the effectiveness of using periodic corrugation to increase the efficiency of a photoluminescent device. Through measurements and analysis of the emission from these devices we determine that the Bragg scattering of light that is otherwise confined to the fully guided modes of a structure can result in an increase in efficiency.

Contents

Abstract.....	0
Contents.....	2
List of figures.....	4
Acknowledgements	9
Chapter 1 Introduction.....	10
Chapter 2 Background.....	14
2.1 Introduction	14
2.2 Modes of planar systems	16
2.2.1 Surface modes	16
2.2.2 Waveguide modes	20
2.2.3 Metal clad microcavity	27
2.2.4 Fresnel coefficients	29
2.3 Dipole emission	33
2.3.1 Fields of an emitter in free space	36
2.3.2 Fields of an emitter in a cavity	37
2.3.3 Cavity modification to SpE	39
2.3.4 Coupling to cavity modes	40
2.3.5 Far field radiation	43
2.4 Summary	44
Chapter 3 Efficiency of emission from planar microcavities	45
3.1 Introduction	45
3.2 Assessing the radiative efficiency of different structures	47
3.2.1 The single interface	48
3.2.2 Multi-layer cavities	52
3.3 Discussion	58
3.4 Summary	60
Chapter 4 Emission from birefringent polymer films.....	61
4.1 Introduction	61
4.2 Theory	63

4.2.1 Vertical orientation of dipole moment.....	64
4.2.2 Horizontal orientation of dipole moment.....	66
4.3 Experiment.....	70
4.4 Discussion.....	72
4.5 Birefringence and mode dispersion.....	77
4.6 Summary.....	79
Chapter 5 Radiative efficiency of absorbing polymer films.....	81
5.1 Introduction.....	81
5.2 Modelling the emission.....	84
5.2.1 Assumptions made in the model.....	84
5.2.2 Spectral width.....	86
5.2.3 Excitation profile.....	88
5.2.4 Intrinsic emission spectrum of MEH-PPV.....	89
5.2.5 Emission pathways: experimental details.....	91
5.3 Discussion.....	93
5.4 Predictions of the model for photoluminescence (PL).....	95
5.5 Using the model to explore electroluminescence (EL).....	98
5.6 Summary.....	104
Chapter 6 Effects of corrugation on polymer emission.....	106
6.1 Introduction.....	106
6.2 Method of Candezon et al.	108
6.3 Experimental.....	109
6.4 Results and discussion.....	111
6.4.1 Weak corrugation (samples A and B).....	112
6.4.2 Stronger corrugation (sample C).....	120
6.4.3 Integrated emission intensity.....	122
6.5 Summary.....	124
Chapter 7 Summary and future work.....	126
7.1 Summary.....	126
7.2 Future work.....	127
Publications and presentations.....	130
References.....	132
Appendices.....	137

List of figures

Figure 2.1	Lifetime of a monolayer of Eu^{3+} ions above a metal mirror, as a function of ion/mirror separation.	15
Figure 2.2	A TM polarised electromagnetic wave incident on a planar interface with resulting reflected and transmitted waves.	17
Figure 2.3	Charge distribution and profile of the E_z field component associated with an SPP mode.	19
Figure 2.4	A planar slab waveguide structure.	20
Figure 2.5	Possible electric field profiles in a slab waveguide as a function of in-plane wavevector.	22
Figure 2.6	The field profiles for the first three TM and TE guided modes of an air/dielectric/metal waveguide.	26
Figure 2.7	Charge distributions and electric field lines for the SPP modes of a metal-clad cavity.	28
Figure 2.8	Electromagnetic wave incident on a planar interface with resulting reflected and transmitted waves.	29
Figure 2.9	Transmitted and reflected fields for a multi-layered structure resulting from a plane wave of unit amplitude.	30
Figure 2.10	Reflectance at normal incidence, as a function of guide thickness, for an air/silica/silver structure.	31
Figure 2.11	TM polarised reflectance, as a function of incident angle in silica, for a silica/silver/air structure.	32
Figure 2.12	Schematic of an emitter located within a planar microcavity.	37
Figure 2.13	The decay rate and the dispersion of the modes to which an emitter couples as a function of cavity thickness for the perpendicular dipole orientation. The emitter is centrally located in a metal-clad microcavity.	41

Figure 2.14	The decay rate and the dispersion of the modes to which an emitter couples as a function of cavity thickness for the parallel dipole orientation. The emitter is centrally located in a metal-clad microcavity.	42
Figure 3.1	Basic structure of the system (involving an emissive polymer layer) that is examined in chapter 3.	46
Figure 3.2	The rate and amount of power radiated into a low index region as a function of emitter interface separation. The emitters are located in a high refractive index material close to the interface with a low index region.	48
Figure 3.3	The fraction of total power that is radiated by an emitter up to the critical angle for transmission into the low index region, and the actual amount of power transmitted into that region, as functions of emissive layer index.	49
Figure 3.4	The fraction of total power that is radiated by an emitter up to the critical angle for transmission into the low index region as a function of dipole orientation.	51
Figure 3.5	The fraction of total power that is radiated out of the $\lambda/2$ Al/polymer/ITO/DBR system as a function of both emitter position in the emissive layer and number of layer pairs which make up the standard DBR.	53
Figure 3.6	The fraction of total power that is radiated out of the $\lambda/2$ Al/polymer/ITO/DBR system as a function of both emitter position in the emissive layer and number of layer pairs which make up the omni-directional DBR.	54
Figure 3.7	The fraction of total power that is radiated out of the $\lambda/2$ Al/polymer/Au system as a function of both emitter position in the emissive layer and Au layer thickness.	56
Figure 3.8	Angle dependent radiation pattern for three types of top cavity mirror, for both isotropic and horizontally oriented emitters.	57

Figure 4.1	Schematic of an emitter located within a planar microcavity where the layers of the structure may be birefringent.	64
Figure 4.2	The photoluminescence spectra from a ~30nm thick MEH-PPV film on a black-backed silica substrate as a function of detection angle.	71
Figure 4.3	The experimentally determined radiation pattern for the MEH-PPV sample (at 680nm), and the Lumogen dye doped polycarbonate sample (at 650nm).	72
Figure 4.4	The radiation pattern for the MEH-PPV sample at 680nm plotted with (a) a standard and modified Lambertian function and (b) the results of our model.	74
Figure 4.5	The radiation pattern for the Lumogen dye doped polycarbonate sample at 650nm plotted with a standard Lambertian function and the results of our model.	76
Figure 4.6	The dispersion of modes for a birefringent dielectric layer bound by regions of air and metal.	78
Figure 4.7	The dispersion of modes for an isotropic dielectric layer bound by regions of air and metal.	78
Figure 5.1	A functional representation of the complex refractive index (both in-plane and out of plane) for a spun film of MEH-PPV.	86
Figure 5.2	(a) The measured emission spectrum (at 15°) for a thin MEH-PPV film. (b) The calculated modification to the polymers intrinsic spectrum. (c) The deduced intrinsic spectrum for MEH-PPV.	91
Figure 5.3	A schematic of the four types of sample used to examine the different emissive pathways for emission from a polymer film.	92
Figure 5.4	The calculated radiative efficiency of a composite emitter for different sample configurations, as a function of emitter location within the polymer layer.	94

Figure 5.5	Calculated efficiency of the emission from the photo-excited air/MEH-PPV/silica system for (a) a spread of composite emitters and (b) a single emitter at a fixed position.	97
Figure 5.6	Schematic of the green LED structure of Kim et al., which includes the optical parameters used in our model.	98
Figure 5.7	Contributions to the total power lost by an emitter within the green LED, as a function of the normalised in-plane wavevector.	101
Figure 5.8	The probability of a singlet exciton decaying to produce a photon that is emitted from the diode surface, as a function of the quantum efficiency.	102
Figure 5.9	The variation of α and the contributions to the total power lost by a singlet exciton, as a function of emitter position in the polymer layer for $q=1$.	103
Table 5.1	The power emitted by the different sample configurations, normalised to the power emitted by the bare sample, along with results of our theoretical model.	95
Figure 6.1	A schematic of the sample structures we fabricated. One half of the sample was corrugated and the other was left flat.	110
Figure 6.2	An example of the angle dependent emission spectra measured from our corrugated samples.	112
Figure 6.3	A schematic of the mode dispersion that we expect for a flat sample region. The polymer is birefringent, the in-plane index being greater than the normal to the plane index.	113
Figure 6.4	The greyscale indicates the mode dispersion for the flat sample region. The hollow square data corresponds to peaks in the detected emission from the corrugated region of sample A that has been adjusted so as to be represented in the extended zone.	114

Figure 6.5	A schematic of the effects of Bragg scattering of the SPP mode in our samples. The possible band gap generation where modes cross is indicated.	116
Figure 6.6	The grey scale indicates the mode dispersion for the corrugated region of sample A, based on a reflectivity model of the system. The hollow square data corresponds to peaks noted in the angle dependent emission spectra measured for the sample.	117
Figure 6.7	The grey scale indicates the mode dispersion for the corrugated region of sample B, based on a reflectivity model of the system. The hollow square data corresponds to peaks noted in the angle dependent emission spectra measured for the sample.	118
Figure 6.8	The grey scale indicates the mode dispersion for the corrugated region of sample C, based on a reflectivity model of the system. The hollow square data corresponds to peaks noted in the angle dependent emission spectra measured for the sample.	120
Figure 6.9	The emission spectrum integrated over all angles, for the corrugated regions of samples B and C, and for a flat region for comparison. The area under each curve gives a measure of the total intensity of the emission from each sample.	122
Table 6.1	The parameters defining the corrugation profiles for our samples, as derived by fitting theory to the measured reflectivity data from a region of corrugated photoresist coated only with optically thick gold.	111

Acknowledgements

I must start by acknowledging the source of all of the experimental data in chapters 4, 5, and 6 of this thesis- my thanks to Alexei Safonov. In addition to providing me with his results, he also proved refreshingly entertaining on the number of occasions that we crossed paths.

It should go without saying, but mention it I shall, that my supervisor, Bill Barnes, has been most excellent. Supportive, constructive and enthusiastic (as well as tolerant) are other words that come to mind. Trevor is another remarkably helpful character I would like to thank. Roy also deserves some special mention for his helpfulness and for being the person who first tempted me with thoughts of staying around the department. Rob Hicken deserves acknowledgement as my second supervisor. There are lots of other people that have been part of department and have made it such a good place to wander about. My thanks go to Martin, Benny, Ben, Piers, Mike J, Phil, Alister, Nathan, Hazel, Sharon, Ian, Pete V, Pete C, John, Mel, Tony and Hobbit. Whenever I have visited the office everyone up there has been helpful and friendly, for which I am grateful. Other people who I should thank, but haven't, are also thanked.

Kate has been supportive to a huge extent, thank you. Mum and Dad, thanks for all you have done for me over the years, in particular for all the encouragement you have given me. I know it is as much as a relief for you as it is for me to get this thing finally finished.

Chapter 1

Introduction

Light emission from thin films is the basis of many optical devices, such as the light emitting diode (LED). The effect of placing an emitter in a structure having dimensions comparable to the wavelength of the emission can drastically change the behaviour of the emitter. This is evident if we consider the probability of spontaneous emission for a two-state emitter, as given by Fermi's Golden Rule [Brorson et al. (1990)]:

$$\Gamma_{ij} \propto |\mathbf{M}_{ij}|^2 \rho(\omega_{ij}) \quad (1.1)$$

where Γ_{ij} is the rate of transition from an excited state i to a lower energy state j (which results in the emission of a photon), \mathbf{M}_{ij} is a matrix element which relates the states i and j through their wavefunctions (and the time dependent contribution to the emitters potential energy), and ρ is the density of states available at the transition frequency, ω , between the states i and j . The process of spontaneous emission is intrinsically quantum mechanical in origin, and the transition rate given by equation (1.1) can be obtained by considering the total Hamiltonian of a quantum emitter, $\hat{H} = \hat{H}_0 + \hat{H}'$ (\hat{H}_0 and \hat{H}' are the time-independent and time-dependent parts of the Hamiltonian respectively), where the time-dependence is treated as a first order perturbation. The term 'spontaneous emission' implies the absence of an external applied field, such that no external perturbation exists to enable a change of state of the emitter. However, it is contributions from both the non-zero fields of the vacuum, the zero-point radiation of quantum electrodynamics, and the radiation reaction field, the field produced by a charged particle at the position of the particle, that provide the perturbation and stimulate the emission [Milonni (1994)].

We have defined an initial and final state for the emitter in terms of the quantised energy levels of the emitter (these are distinct eigenstates of \hat{H}_0). However, the final energy eigenstate of the emitter is degenerate, and there are in fact many final states available to the emitter. This must be the case if we are

to account for all of the possible directions into which the photon may be emitted; all of these final states correspond to a single eigenstate of \hat{H}_0 . These final states are distinguished by the direction of the momentum imparted to the emitter according to the direction of the emitted photon (the momentum that the emitter gains through the emission of a photon can be determined by the conservation of momentum). The density of states of the vacuum field is therefore introduced when the continuum of final states is accounted for. The density of states can generally be regarded, classically, as the ability of the space around the emitter to support an emitted photon. ρ , the photonic mode density (PMD), is then clearly defined by the boundary conditions of the system. The spontaneous emission rate as normally defined assumes that the emitter is situated in infinite free space. The presence of an interface (typically at ranges corresponding to the wavelength of emission) modifies the PMD and thereby alters the decay rate of an emitter. Looking at equation (1.1), it is clear that the decay rate of an emitter can also be affected by changing \mathbf{M} . The wavefunction for any particular state of the emitter (and therefore each element of \mathbf{M}) is modified by the presence of an interface at distances comparable to the decay constant of an atomic wavefunction i.e. of the order of 0.1nm. In this work we will be concerned with emitter/interface separations $>1\text{nm}$, and will therefore be influencing ρ , the PMD.

Although a classical approach cannot account for the phenomenon of spontaneous emission, it can, for example, be used to make a calculation of the spontaneous emission rate for an electric dipole transition of an emitter. By considering, classically, the ratio of the power radiated by an oscillating electron (electric dipole) to the energy of a photon with the same frequency, an emissive rate can be determined. The work of Yeung and Gustafsen (1996) provides an important demonstration of the validity of a classical derivation of the spontaneous emission rate. They calculate the lifetime of an excited atom near an absorbing dielectric surface using the exact solution of a microscopic Hamiltonian model that includes the effects of dispersion, local-field corrections and near-field Coulomb interactions. The only significant difference between the two approaches is the statistical nature of the quantum mechanical predictions.

This is a very significant piece of work in that the exact quantum calculation is complex and less easy to perform than its classical counterpart. The excellent agreement justifies the use of a classical approach, which in the work presented here is applied to the modelling of spontaneous emission within wavelength-scale structures. As discussed, the classical approach is generally simpler to employ and lends itself to describing the macroscopic structures that we consider in this work.

We know, from equation (1.1), that the behaviour of an emitter can be modified by its environment. The present work focuses on a study of emitters in structures (specifically microcavities) that modify the PMD at the emission frequency. A significant amount of work has been already done in modelling spontaneous emission from molecules embedded in such structures [Chance et al. (1978), Lukosz (1980), Ford and Weber (1984), Benisty et al. (1998)]. However, we are predominantly concerned with the efficiency with which power can be extracted from structures (as far field radiation) where the emissive materials are conjugated polymers. Conjugated polymers are of great interest as the light-emitting material in LED devices because of the ease in which thin films of the material can be produced (in solution) [Samuel (2000)]. Owing to the relatively high refractive index of the majority of light emitting materials, much of the emitted energy remains trapped in the emissive layer due to total internal reflection. As such, modifying the spontaneous emission of a molecule has major applications in devices such as LEDs, where both the decay rate and decay routes of optical emitters may be optimised, to produce large increases in device efficiency.

This thesis is structured as follows. Chapter 2 introduces the guided modes typically associated with planar structures and classical theory for modelling the behaviour of an emitter within a microcavity. Chapter 3 investigates optimum LED configurations where the top mirror (partially transparent) is treated as either a distributed Bragg stack or a metal. The effects on performance of varying the parameters of the top mirror, the cavity thickness, emitter orientation and position are all investigated. In chapter 4 the effects of the birefringence of thin films of an organic light-emitting polymer are investigated. The importance of birefringence and emitter orientation upon accurately modelling the emission from a thin polymer film is assessed, and the

effects of birefringence on mode dispersion are also detailed. In chapter 5 a comprehensive model, incorporating spectral width of emission and a spread in emitter locations, for emission from polymer films is presented. This model is used to analyse the efficiency of photoluminescent and electroluminescent polymer devices. In chapter 6 the use of periodic corrugation in a photo-excited polymer structure is investigated. The effects of scattering light otherwise coupled to trapped guided modes of the structure into far field radiation are assessed, and changes in efficiency are measured. Chapter 7 is a summary of the work presented and includes proposed areas for further work.

Chapter 2

Background

2.1 Introduction

In this chapter, we describe the basic effects associated with emission from within typical planar cavities. For an excited emitter in free space, relaxation to a lower energy may result in spontaneous radiative emission (the effect of internal non-radiative decay is considered later on). The confinement of an emitter within a microcavity, or the proximity of an emitter to a nearby interface, results in some change to this emission. The direction and rate of emission can both be modified. In the case of a microcavity, emission for particular directions and energies, corresponding to the modes of the structure, may be enhanced whilst all others are suppressed. For an emitter above a metal mirror, at particularly small separations ($\ll \lambda$) the dominant decay route will be to bulk modes in the metal. As the distance increases decay may be dominated by non-radiative coupling to the surface modes of the metal. At greater distances the sole effect will be due to the interference between radiative fields that are reflected and directly emitted.

In figure 2.1 the modified spontaneous emission lifetime [$=1/(\text{modified decay rate})$] of a monolayer of Eu^{3+} ions above a silver mirror is shown as a function of ion-mirror separation. A transparent spacer layer was used to separate the emitters and the metal. Excited Eu^{3+} ions have a radiative decay that is dominated by a narrow 614nm emission, which corresponds to an electric dipole transition. This means that emission at that single wavelength is all that need be considered to adequately model the system. Furthermore, the dipole moment associated with the emission is considered to have an isotropic distribution. This is because the

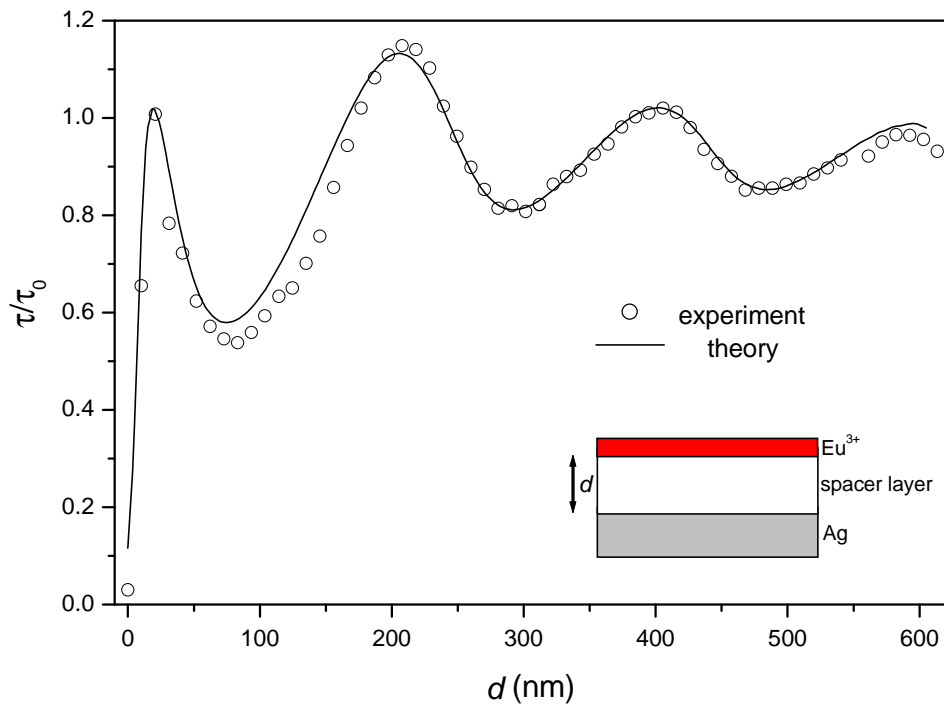


Figure 2.1 Lifetime, τ , of a monolayer of Eu^{3+} ions as a function of the separation distance between the monolayer and the silver mirror. The open circles are experimental data, and the line is obtained from a theoretical model described in section 2.3. τ_0 is the lifetime of the ions in free space. From Andrew (1998).

dipole moment of the ion freely rotates and, due to the long lifetime of the excited state ($\sim 0.9\text{ms}$), can sample all possible orientations. In figure 2.1 we see that for $d > 50\text{nm}$, there is a clear oscillation in the lifetime. This corresponds to the fields reflected from the mirror (that act to drive the emitter) going in and out of phase with the emitter. The oscillation period of 200nm equates to an optical path length, in the spacer material, of one half of the wavelength of emission. For $d < 50\text{nm}$, there is a significant decrease in lifetime (increase in decay rate) as the ion-mirror separation decreases, which corresponds to an increase in the coupling to the surface mode of the mirror.

The electromagnetic modes of a structure to which an emitter may couple are defined by the geometry and materials of the system. The field profile of a particular mode, the orientation and position of the emitter, will

determine the coupling strength between the emitter and that mode. In order to appreciate the mode structure of a typical cavity system, the conditions for waveguiding in a film, and for the existence of surface bound modes are outlined below in section 2.2. A well known classical approach to modelling the decay of an emitter within a microcavity is then detailed in section 2.3. This model is used to highlight typical features seen in the behaviour of a cavity bound emitter, in the context of coupling to the available cavity modes.

To pre-empt possible confusion, the (italic) variable n corresponds to the perpendicular component of the wavevector, and not to a refractive index.

2.2 Modes of planar systems

A simple approach is taken towards identifying the dispersion of surface and guided modes in a planar system. In general, the materials considered are linear and non-magnetic. In this section, all materials are isotropic (the effect of birefringence is the subject of chapter 4).

2.2.1 Surface modes

Consider the planar interface between two semi-infinite media, as depicted in figure 2.2. Assuming there is no free charge in the system, Maxwell's equations can be used to show that the normal component of the electric displacement \mathbf{D} is continuous across the interface. The electric field \mathbf{E} at any point is related to \mathbf{D} by

$$\mathbf{D} = \epsilon_j \epsilon_0 \mathbf{E} \quad (2.1)$$

where ϵ_0 is the permittivity of free space and ϵ_j is the relative permittivity of the j th medium (generally a complex quantity). If the top region is a dielectric with a positive real part of ϵ_j , and the bottom region is a metal with a negative real part of ϵ_j , then there is a difference in the sign of the normal component of \mathbf{E} across the interface. This sign change corresponds to a sheet of polarisation charge at the interface. This means that any field, with a normal component of electric field, that is applied to a metal/dielectric interface will result in such surface bound polarisation charge. The coupling between an electromagnetic

wave and a surface charge oscillation defines a surface plasmon polariton (SPP).

By considering a harmonic time variation of the fields in the system, the dispersion relation for the SPP can be derived. The following approach is taken from R  ether (1988).

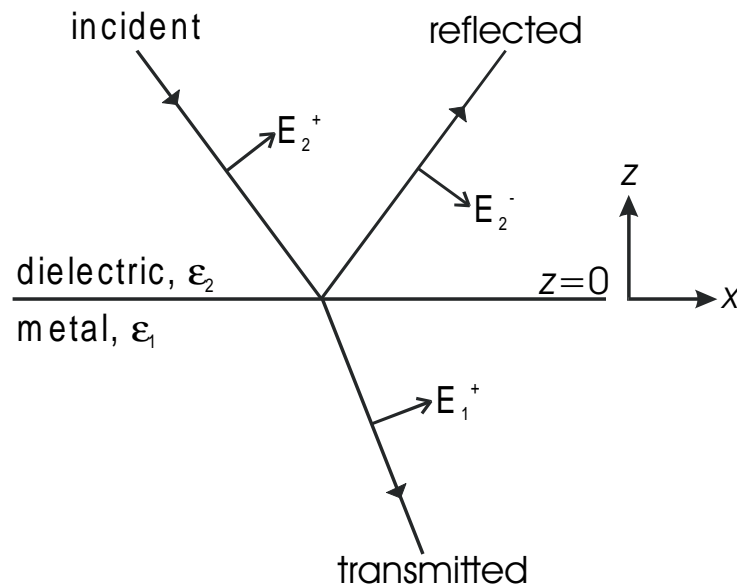


Figure 2.2 A TM polarised electromagnetic wave incident on a planar interface, with the resulting reflected and transmitted waves.

Figure 2.2 shows a TM polarised electromagnetic wave incident on the planar interface between a dielectric with a relative permittivity ϵ_2 , and a metal with a relative permittivity ϵ_1 . The subsequent reflected and transmitted waves are also shown. Only the TM polarisation need be considered, as a component of \mathbf{E} normal to the interface is required to provide the necessary polarisation charge at the interface. In solving for the fields of a surface mode only one electromagnetic wave needs to be considered in each medium. As such, the fields of \mathbf{E}_2^- are set to zero. The resulting electromagnetic fields can be expressed in the following manner

$$\begin{aligned}
 z > 0 \quad \mathbf{E}_2 &= (E_{x2}, 0, E_{z2}) \exp i(u_2 x + n_2 z - \omega t) \\
 \mathbf{H}_2 &= (0, H_{y2}, 0) \exp i(u_2 x + n_2 z - \omega t)
 \end{aligned} \tag{2.2}$$

$$\begin{aligned}
z < 0 \quad \mathbf{E}_1 &= (E_{x1}, 0, E_{z1}) \exp i(u_1 x - n_1 z - \omega t) \\
\mathbf{H}_1 &= (0, H_{y1}, 0) \exp i(u_1 x - n_1 z - \omega t)
\end{aligned} \tag{2.3}$$

where \mathbf{H} is the magnetic field, ω is the frequency of oscillation, and \mathbf{k} is the wavevector of the mode with $\mathbf{k}=(u,0,n)$, such that u and n are the parallel and perpendicular components of the wavevector respectively.

Upon substituting these field terms into Maxwell's curl equation

$$\nabla \wedge \mathbf{H} = \epsilon_i \epsilon_0 \frac{\partial \mathbf{E}}{\partial t} \tag{2.4}$$

we get the following expressions relating \mathbf{E} and \mathbf{H}

$$n_2 H_{y2} = -\omega \epsilon_0 \epsilon_2 E_{x2} \tag{2.5}$$

$$n_1 H_{y1} = \omega \epsilon_0 \epsilon_1 E_{x1} \tag{2.6}$$

The boundary conditions arising from Maxwell's equations are that the tangential components of \mathbf{E} and \mathbf{H} be continuous across the interface. Application of these conditions shows that $E_{x1}=E_{x2}$ and $H_{y1}=H_{y2}$. An expression corresponding to the conservation of momentum parallel to the interface is also obtained

$$u_1 = u_2 = u \tag{2.7}$$

From equations (2.5) and (2.6) it can be shown that

$$\epsilon_1 n_2 = -\epsilon_2 n_1 \tag{2.8}$$

From the wave equation, the wavevector can be expressed as

$$k_i^2 = u^2 + n_i^2 = \epsilon_i \left(\frac{\omega}{c} \right)^2 \quad i=1,2 \tag{2.9}$$

Combining equations (2.8) and (2.9) gives the dispersion relation for the SPP mode. For some frequency ω , this mode occurs for a particular value of in-plane wavevector u given by

$$u_{SPP} = \frac{\omega}{c} \sqrt{\frac{\epsilon_1 \epsilon_2}{\epsilon_1 + \epsilon_2}} \tag{2.10}$$

In general, both ϵ_1 and ϵ_2 can be complex. In describing a realistic system the relative permittivity of the metal will be complex, so the media can be described by $\epsilon_2 \geq 1$ and $\epsilon_1 = \epsilon_1' + i\epsilon_1''$. By including the absorption explicitly in equation

(2.10), the real and imaginary components of u_{SPP} can be identified. If the metal we consider is a good one, that is to say absorption and field penetration in the metal are both low, then $|\epsilon'_1| \gg \epsilon''_1$, and by writing $u_{SPP} = u'_{SPP} + i u''_{SPP}$, equation (2.10) gives

$$u'_{SPP} = \frac{\omega}{c} \left(\frac{\epsilon'_1 \epsilon_2}{\epsilon'_1 + \epsilon_2} \right)^{1/2} \quad (2.11)$$

and

$$u''_{SPP} = \frac{\omega}{c} \left(\frac{\epsilon'_1 \epsilon_2}{\epsilon'_1 + \epsilon_2} \right)^{3/2} \frac{\epsilon''_1}{2\epsilon_1'^2} \quad (2.12)$$

For the SPP to be a propagating mode in the plane of the interface, u'_{SPP} must be real. Equation (2.11) shows that for this to be true and $\epsilon'_1 < 0$, then $|\epsilon'_1| > \epsilon_2$. With these conditions satisfied it is clear from equation (2.11) that $u'_{SPP} > \sqrt{\epsilon_2} (\omega/c)$, which means that the SPP mode has a greater parallel momentum than a grazing photon of the same frequency in the dielectric immediately above. This means that no photon in the dielectric region is capable of coupling directly to the SPP mode, the SPP mode is non-radiative. Looking at equation (2.9) it is clear that the perpendicular component of the wavevector (n_z) for the SPP mode is always complex. The fields of this mode must therefore decay exponentially away from the metal/dielectric interface, as we would expect for a non-radiative mode. The form of the fields and the associated charge distribution for a SPP mode are shown in figure 2.3.

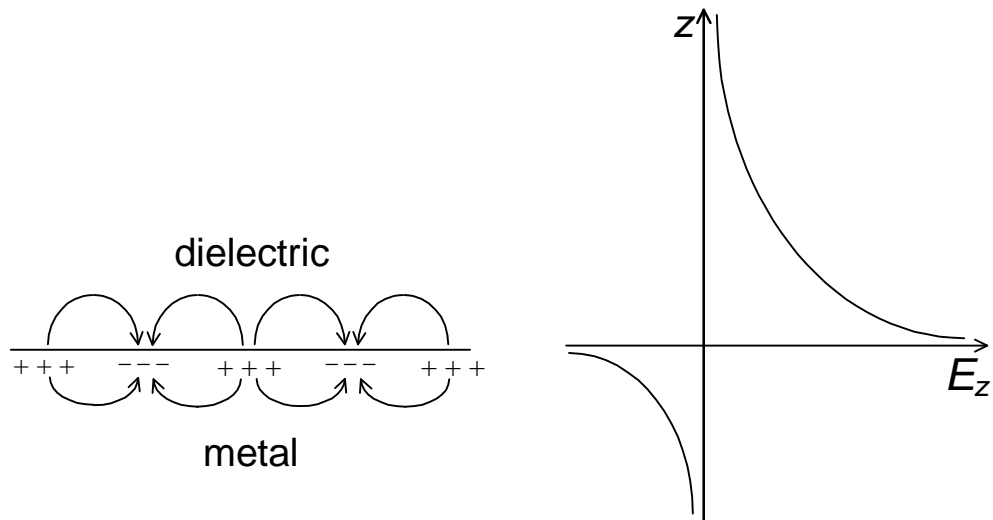


Figure 2.3 Charge distribution and profile of the E_z field component associated with a SPP mode.

2.2.2 Waveguide modes

Similar to SPP modes, waveguide modes are confined electromagnetic waves. Typical waveguide structures constitute a guiding region, in which the mode propagates, bound by regions in which the fields of the mode decay exponentially. In figure 2.4 the form of a simple planar slab waveguide is shown. By considering the electromagnetic fields in this structure the dispersion relations for any waveguide modes present may be derived as follows.

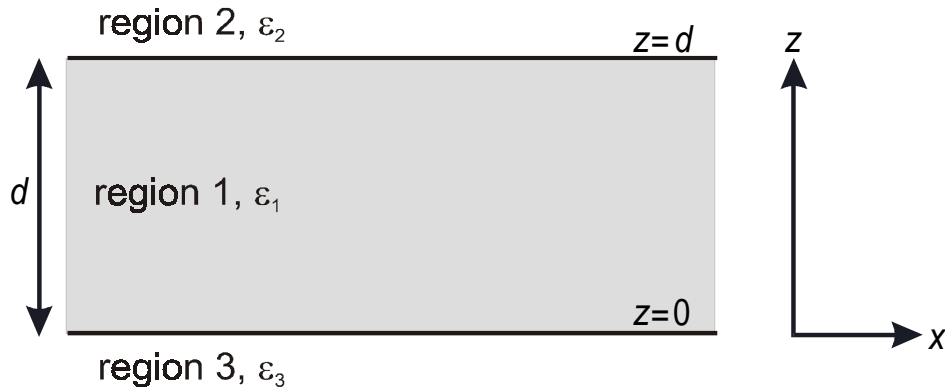


Figure 2.4 A planar slab waveguide structure.

Assuming a harmonic time dependence of the fields, the waveguide modes will be solutions of the vector wave equation

$$\nabla^2 \mathbf{F}(\mathbf{r}) + \omega^2 \epsilon \mu \mathbf{F}(\mathbf{r}) = 0 \quad (2.13)$$

where the variable $\mathbf{F} = (F_x, F_y, F_z)$ represents both \mathbf{E} and \mathbf{H} since they both satisfy the same expression for a source-free region. Solutions to the wave equation are chosen to be waves propagating in the x-direction,

$$\mathbf{F}(\mathbf{r}, t) = \mathbf{F}(z) \exp i(ux - \omega t) \quad (2.14)$$

where u is again the tangential component of the wavevector. From equation (2.13), and using the relation $\omega^2 \epsilon \mu = \epsilon_i k_0^2$ (where $k_0 = \omega/c$), the fields in each of the three regions are governed by

$$\frac{\partial^2}{\partial z^2} \mathbf{F}_i(z) + (\epsilon_i k_0^2 - u^2) \mathbf{F}_i(z) = 0 \quad i=1,2,3 \quad (2.15)$$

The solution for equation (2.15) takes the standard form

$$F_{xi}(z) = F_{xi}^+ \exp(in_i z) + F_{xi}^- \exp(-in_i z) \quad (2.16)$$

with similar expressions for F_y and F_z , where $n_i = \epsilon_i k_0^2 - u^2$.

Before going on to an exact solution of the waveguide dispersion, we investigate the general form of the solution to equation (2.15) and its dependency on the value of the tangential wavevector. A structure, as in figure 2.4, that acts as a slab waveguide would be a dielectric layer bounded by either lower refractive index dielectric regions or metals. In both cases the fields of a guided mode are confined to the vicinity of the central guiding layer in which the mode propagates. A good metal will exclude the fields of the mode, and an adjacent dielectric with a lower refractive index will provide strong confinement when total internal reflection occurs. Consider the dielectric slab (in figure 2.4) to be bound above by a dielectric with a lower refractive index (such that $\epsilon_1 > \epsilon_2 \geq 1$), and below by a metal. Referring to equation (2.16), the solution of equation (2.15) can be classified into three distinct forms, though in each the fields always decay exponentially into the metal. Possible field profiles are also shown for each type of solution in figure 2.5.

a) $0 < u^2 < \epsilon_2 k_0^2$ Radiative modes

This regime is below the cut-off for total internal reflection at the top dielectric interface, and the fields in both dielectric regions have a sinusoidal solution. As a result, modes are not confined solely to the slab and are referred to as *radiative* or *partially guided* (and sometimes in the literature as *leaky*).

b) $\epsilon_2 k_0^2 < u^2 < \epsilon_1 k_0^2$ Fully guided modes

This regime is above the cut-off for total internal reflection at the top dielectric interface, and the fields have a sinusoidal form in the guiding slab and an exponential form in the dielectric above. In this case the mode is confined to the guiding slab and is called a *fully guided* mode. A necessary condition for this to occur is $\epsilon_1 > \epsilon_2$.

c) $\epsilon_1 k_0^2 < u^2$ Surface modes

In this case the fields have an exponential form throughout the structure, since the in-plane wavevector exceeds the value for a propagating wave in all

regions. There are no waveguide solutions. The only possible modes are surface modes, as depicted in figure 2.5 and discussed above in section 2.2.1.

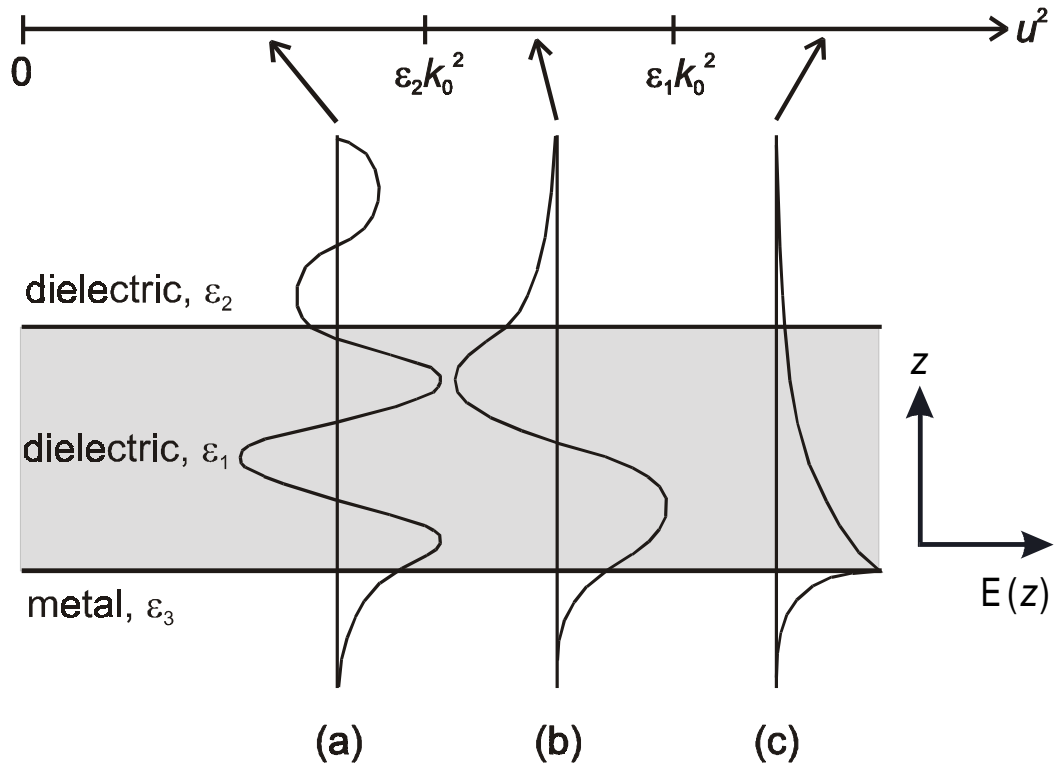


Figure 2.5 Possible field profiles $E(z)$ in the slab waveguide, depicted in figure (2.4), for different values of the tangential wavevector u .

Due to the lack of field confinement in the z -direction when $0 < u^2 < \epsilon_2 k_0^2$, the value of u for which a radiative mode will occur is continuous. That is to say, there is no restriction on the direction of a propagating mode in the topmost dielectric region, and since such a mode always corresponds to some finite field profile within the guide, a continuum of radiative modes is possible. However, when $\epsilon_2 k_0^2 < u^2 < \epsilon_1 k_0^2$ there are only a discrete number of fully guided modes possible. This results from the confinement of the field to the guiding layer, where both interfaces totally reflect a wave incident from within the guide. A mode can only occur within the guide at discrete values of u for which these reflected fields are all in-phase. The number and position of these modes is determined by the frequency ω , the thickness of the guiding layer d , and the relative permittivity ϵ_i of the different regions in the structure. The dispersion

relation for these fully guided modes is now derived. Starting with Maxwell's curl equations, and looking for solutions of the form of equation (2.14), we obtain

$$\begin{aligned}
 \frac{\partial}{\partial z} E_y &= -i\omega\mu H_x & \frac{\partial}{\partial z} H_y &= i\omega\varepsilon E_x \\
 uE_y &= \omega\mu H_z & uH_y &= \omega\varepsilon E_z \\
 \frac{\partial}{\partial z} H_x - iuH_z &= i\omega\varepsilon E_y & \frac{\partial}{\partial z} E_x - iuE_z &= i\omega\mu H_y
 \end{aligned} \tag{2.17}$$

These equations can be grouped into two independent sets, one involving the components H_x , H_z , E_y , and the other involving E_x , E_z , H_y , which correspond to the two uncoupled polarisations for this geometry. These sets define the transverse electric (TE or s) and the transverse magnetic (TM or p) polarisations respectively. The solution for each set will be considered separately. It is clear that for each polarisation the solution is fully defined by a single component, since the other two components are obtained directly from equation (2.17).

TE waveguide modes

From equation (2.16), the electric field through the structure must take the form

$$\begin{aligned}
 E_y(z) &= E_{y2}^- \exp(-in_2 z) & z > d \\
 E_y(z) &= E_{y1}^+ \exp(in_1 z) + E_{y1}^- \exp(-in_1 z) & d > z > 0 \\
 E_y(z) &= E_{y3}^+ \exp(in_3 z) & 0 > z
 \end{aligned} \tag{2.18}$$

where the coefficients for terms that are non-finite as $z \rightarrow \pm\infty$ have already been set to zero. By applying the boundary conditions, that H_x ($\propto \partial E_y / \partial z$) and E_y are continuous across the interfaces, the following dispersion relation for the TE fully guided modes is obtained,

$$\tan n_1 d = -in_1 \left(\frac{n_2 + n_3}{n_1^2 + n_2 n_3} \right) \tag{2.19}$$

In general, this expression can not be solved explicitly and numerical methods must be used to obtain approximate solutions. However, it is worthwhile to consider some specific case by which it is possible to get an explicit solution. If we treat the metal region as a perfect metal, such that $\varepsilon_3 \rightarrow -\infty$, then $n_3 \rightarrow i\infty$.

Now consider the case where $n_2 = 0$, that is the cut-off point for which the mode changes from propagating in the top most dielectric to being evanescent in that region. When $n_3 \rightarrow i\infty$ and $n_2 = 0$, from equation (2.19), we see that $\tan n_1 d \rightarrow -\infty$, which is satisfied when

$$n_1 d = (2j+1)\frac{\pi}{2} \quad (2.20)$$

where j is some positive integer that defines the order of the mode, which corresponds to the number of nodes in the electric field in the guiding layer. At cut-off ($n_2 = 0$), we know that $n_1 = \sqrt{\epsilon_1 - \epsilon_2} \omega/c$. Since equation (2.20) defines the thickness of waveguide for the j th order mode at cut-off, we can write

$$d \geq \frac{\pi c(2j+1)}{2\omega\sqrt{\epsilon_1 - \epsilon_2}} \quad (2.21)$$

For a given guide thickness d , this inequality puts a limit on the number of fully guided TE modes supported by the structure. The maximum value of j that satisfies this inequality corresponds to the highest order mode. Clearly, d can be so small that no modes for a given frequency can be supported. The field profiles for the first three TE guided modes are shown in figure 2.6.

TM waveguide modes

The method for obtaining the dispersion relation for the TM guided modes is very similar. From equation (2.16), the magnetic field through the structure must take the form

$$\begin{aligned} H_y(z) &= H_{y2}^- \exp(-in_2 z) & z > d \\ H_y(z) &= H_{y1}^+ \exp(in_1 z) + H_{y1}^- \exp(-in_1 z) & d > z > 0 \\ H_y(z) &= H_{y3}^+ \exp(in_3 z) & 0 > z \end{aligned} \quad (2.22)$$

By applying the boundary conditions, that E_x and H_y are continuous across the interfaces, the following dispersion relation for the TM fully guided modes is obtained,

$$\tan n_1 d = -\epsilon_1 n_1 \left(\frac{\epsilon_3 n_2 + \epsilon_2 n_3}{\epsilon_2 \epsilon_3 n_1^2 + \epsilon_1^2 n_2 n_3} \right) \quad (2.23)$$

As with equation (2.19), numerical methods are generally required to find solutions to this expression. Again, we consider the specific case of a perfect

metal ($\epsilon_3 \rightarrow -\infty$, $n_3 \rightarrow \sqrt{\epsilon_3} k_0$). This time at cut-off ($n_2 = 0$), from equation (2.23), we see that $\tan n_1 d \rightarrow 0$, which is satisfied when

$$n_1 d = j \pi \quad (2.24)$$

This leads to an expression where the maximum value for j satisfying the inequality represents the highest order TM mode supported by the guide, and corresponds to the number of modes that are allowed

$$d \geq \frac{j \pi c}{\omega \sqrt{\epsilon_1 - \epsilon_2}} \quad (2.25)$$

Unlike the TE case, there is no limit on d below which no TM modes are supported. Specifically, the $j=0$ case corresponds to an SPP mode at the metal/dielectric interface, as discussed in section 2.2.1.

The field profiles for the first three TE and TM guided modes for an air/dielectric/metal structure are shown in figure 2.6. A realistic metal is considered, and as such the field penetration into the metal is shown. The process for obtaining exact field profiles would be to find the values for u that satisfy the dispersion relations, equation (2.19) for TE and equation (2.23) for TM. The appropriate values for u could then be substituted back into equations (2.18) and (2.22), for the TE and TM cases respectively. The remaining field components could then all be found from equations (2.17).

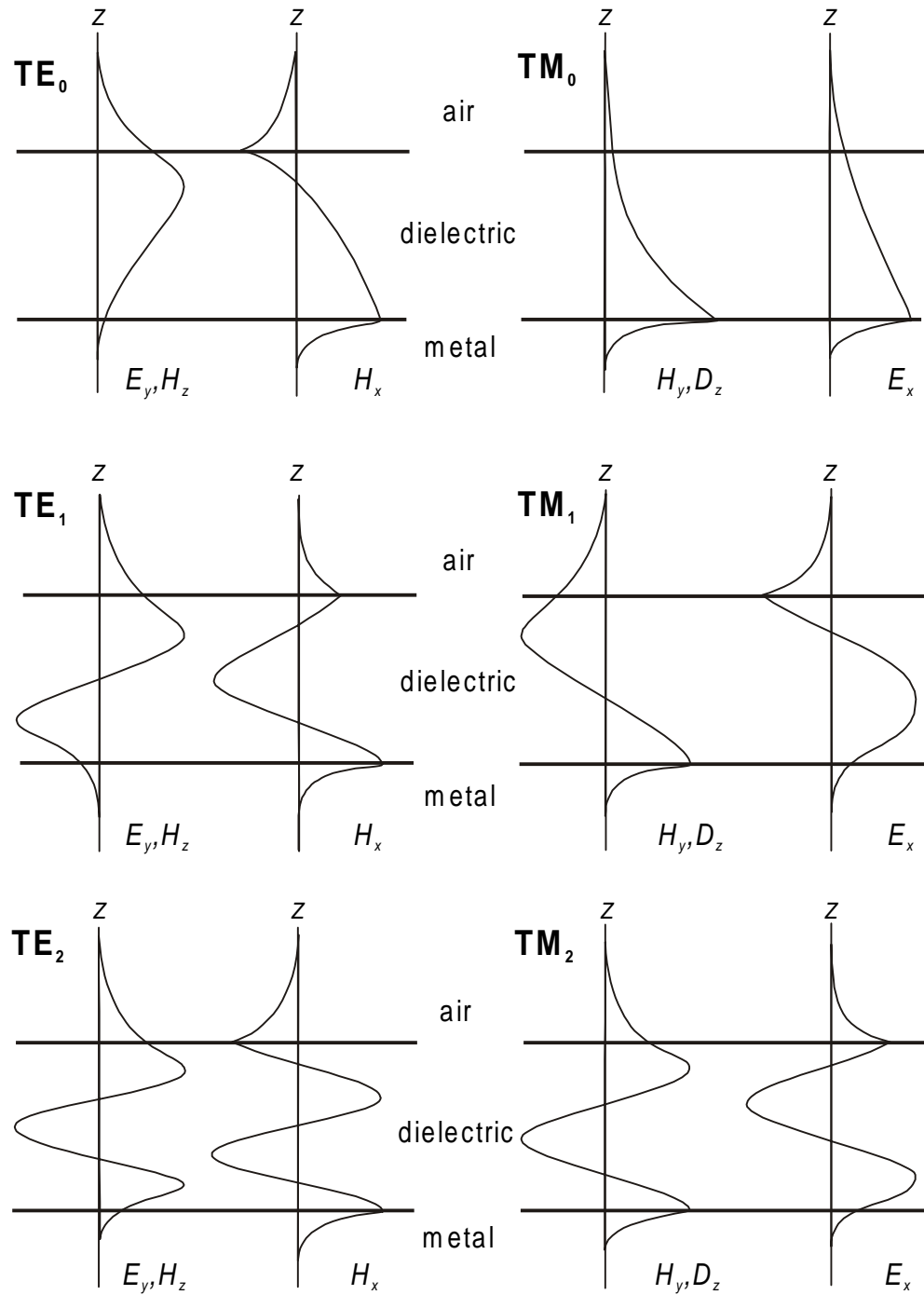


Figure 2.6 Field profiles for the first three TE and TM guided modes of an air/dielectric/metal planar waveguide.

2.2.3 Metal clad microcavity

The surface bound modes at a dielectric/metal interface and the modes of an asymmetric metal-clad waveguide have already been described in sections 2.2.1 and 2.2.2 respectively. Now consider a fully metal-clad waveguide, where a dielectric layer is bounded by semi-infinite regions of metal above and below. Radiative modes are not present, as all fields decay exponentially into the metal regions. The dispersion relations of equations (2.19) and (2.23) still apply to this geometry, but now apply for all values of the tangential wavevector corresponding to propagation in the guiding layer, $0 < u^2 < \epsilon_1 k_0^2$. These dispersion relations, for the TE and TM polarised waveguide modes, reduce to the same expression

$$\tan n_1 d = 0 \quad (2.26)$$

when perfect metals ($\epsilon_2, \epsilon_3 \rightarrow -\infty$) are considered. The lowest thickness, d , for which a waveguide mode will be supported occurs when $u=0$ ($n_1 = \sqrt{\epsilon_1} \omega/c$). From equation (2.26) the lowest value for d for which the j th order mode occurs is given by

$$d = \frac{j \pi c}{\omega \sqrt{\epsilon_1}} \quad (2.27)$$

For a given frequency, there is a guide thickness below which no waveguide modes are possible, often referred to as the cut-off condition.

The metal clad microcavity also supports SPP modes. In section 2.2.1, the dispersion relation for a surface bound SPP mode at a single dielectric/metal interface was derived. In the present fully metal-clad structure there are two such interfaces and we now consider the form of the SPP modes that may be expected. When the guide layer is thin ($\sim \lambda_1$) then the fields associated with the modes of each interface overlap. This interaction means that the modes are coupled [Welford and Sambles (1988)]. There are two fundamental solutions that may result in this case. The charge distribution for each is depicted in figure 2.7. The symmetric SPP solution (a) corresponds to the short range SPP mode (SRSP), which has higher field intensities in the metal regions. Since metals have greater losses, the relatively high fields in the metals mean a reduced propagation distance that defines the SRSP. The anti-

symmetric SPP solution (b) has a larger proportion of its fields in the dielectric, resulting in lower losses. Therefore, the anti-symmetric solution has a greater propagation distance, and is referred to as the long range SPP mode (LRSP). If the guide layer is very thick ($\gg \lambda_1$) then the situation is reduced to that of a single uncoupled SPP mode at each interface. The dispersion for these modes is equivalent to that of the single interface case.

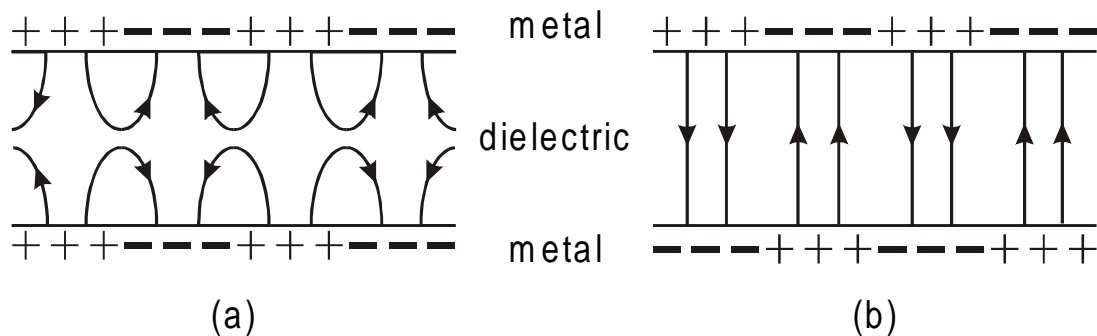


Figure 2.7 Charge distributions and electric field lines for the SPP modes of a metal-clad cavity. The symmetric (a) and anti-symmetric (b) solutions are shown.

Looking at figure 2.7 (b) it is clear that the fields of the LRSP correspond to those of the parallel plate capacitor in the long wavelength limit, and there is no cut-off. With regard to figure 2.7 (a), it would seem that there must be some guide thickness below which a symmetric charge distribution ceases to be viable, as the like charges at close proximity will repel one another away from the interfaces. As such, the SRSP does have a cut-off, and the fields for this mode at cut-off are identical to those of the lowest order TE guided mode. For both the symmetric and anti-symmetric charge distributions, the fields at each interface for both solutions must reduce to those of figure 2.3, the single interface case, when the guide thickness becomes much greater than the wavelength of the mode.

The metal-clad cavity has no modes associated with it that may propagate into the far field (i.e. no radiative modes). In the following section we look at a method for obtaining information about the mode structure of systems that do support radiative modes.

2.2.4 Fresnel coefficients

The mode structure of a system may be clearly evident in the reflective and transmissive properties of that system. Experimentally, the dispersion of the modes is often obtained from reflection and/or transmission measurements [Salt (2000)]. We start by defining the Fresnel coefficients for a single planar interface. These coefficients relate the electric fields of reflected and transmitted waves to that of a plane wave incident on a planar interface. Figure 2.8 shows a wave incident on a planar interface with resulting reflected and transmitted waves for the two orthogonal, s (TE) and p (TM), polarisations.

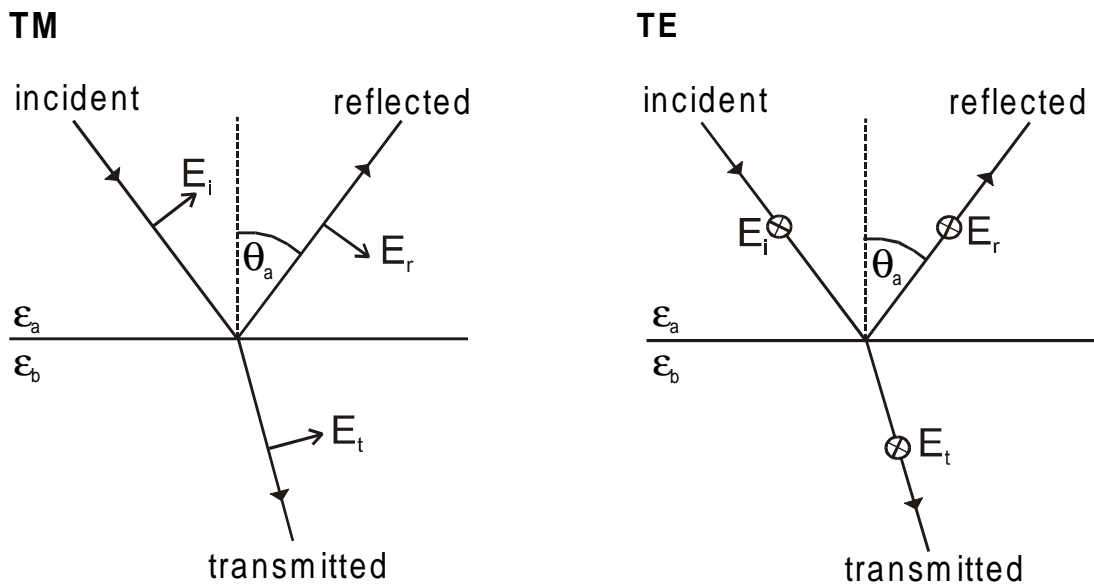


Figure 2.8 TM and TE polarised electromagnetic waves incident on planar interfaces, with the resulting reflected and transmitted waves.

For a plane wave incident on a planar interface, we may expect some reflected and transmitted fields to result. The form of these resulting fields can be found by applying the boundary conditions. The boundary conditions are that the tangential components of the \mathbf{E} and \mathbf{H} fields must be continuous across the interface. The coefficients of the electric field for the reflected (r) and transmitted (t) waves are given by [Pedrotti and Pedrotti (1993)],

$$\begin{aligned}
 r_{s,ab} &= \frac{E_r}{E_i} = \frac{n_a - n_b}{n_a + n_b} & t_{s,ab} &= \frac{E_t}{E_i} = \frac{2n_a}{n_a + n_b} \\
 r_{p,ab} &= \frac{E_r}{E_i} = \frac{n_b \epsilon_a - n_a \epsilon_b}{n_b \epsilon_a + n_a \epsilon_b} & t_{p,ab} &= \frac{E_t}{E_i} = \frac{2n_a \sqrt{\epsilon_a \epsilon_b}}{n_b \epsilon_a + n_a \epsilon_b} \quad (2.28)
 \end{aligned}$$

where, from equation (2.9), n_i is the normal component of the wavevector in the i th medium, and the subscript s or p denotes the polarisation. These coefficients are functions of the tangential wavevector, u . For values of n_i corresponding to propagating waves, we can write $n_i = k_i \cos \theta_i$, where θ is the angle of propagation. We are interested in the transmission and reflection coefficients for structures with multiple interfaces, and so coefficients similar to those of equation (2.28) need to be found. There are a number of methods for determining these. One such approach is the transfer matrix method of Azzam and Bashara. Another is to consider an arbitrary two-interface structure. It is simple to obtain effective reflection and transmission coefficients for such a structure in terms of its single interface coefficients [Pedrotti and Pedrotti (1993)] (equations below with $j=1$). This two-interface structure is equivalent to a single interface in that it is totally described by basic reflection and transmission coefficients. Because of this, coefficients for a multi-layered structure can be constructed using an iterative process relying on the original two-interface expressions.

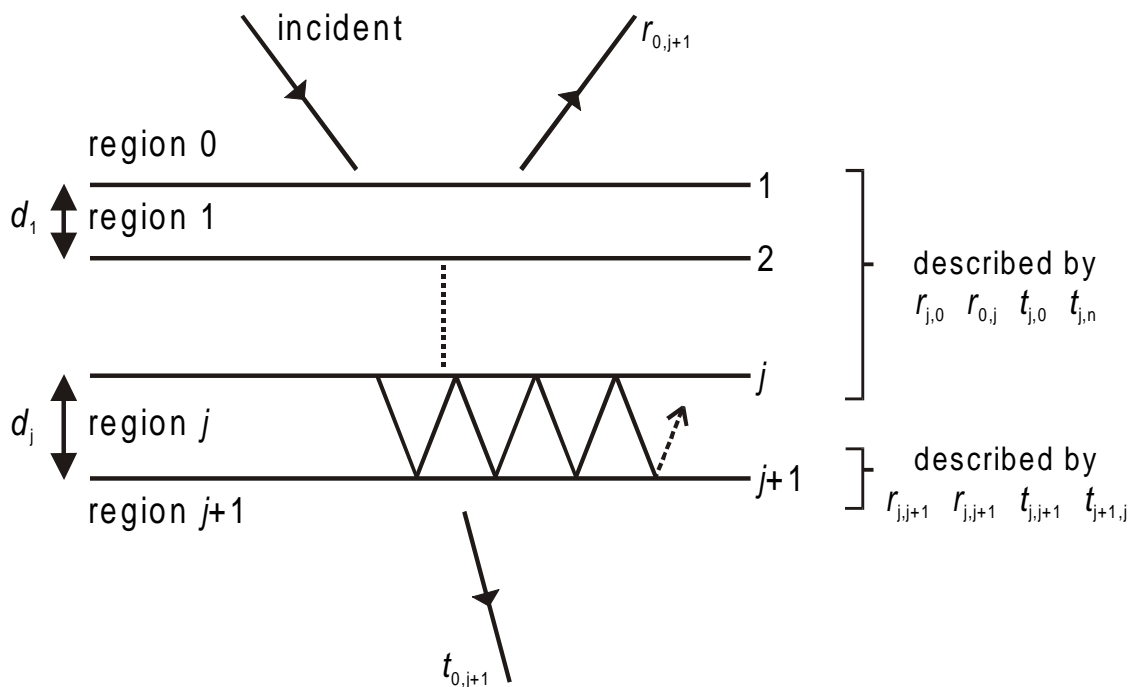


Figure 2.9 Transmitted and reflected fields for a multi-layered structure resulting from a plane wave, of unit amplitude, incident from region 0. The effective coefficients for the first j interfaces are known.

From figure 2.9, the effective transmission and reflection coefficients for a structure comprised of N interfaces can be arrived at, with

$$t_{0,j+1} = \frac{t_{0,j} t_{j,j+1} r_{j,j+1} \exp(in_j d_j)}{1 - r_{j,j+1} r_{j,0} \exp(2in_j d_j)}$$

$$r_{0,j+1} = r_{0,j} + \frac{t_{0,j} t_{j,0} r_{j,j+1} \exp(2in_j d_j)}{1 - r_{j,j+1} r_{j,0} \exp(2in_j d_j)} \quad j=1,2,\dots,N-1 \quad (2.29)$$

and similar expressions for $t_{j+1,0}$ and $r_{j+1,0}$.

By considering a propagating wave incident on a structure, features seen in reflection and/or transmission can be seen to correspond to a coupling to modes of the structure. With such an approach only radiative modes may be studied. A couple of specific examples are examined below.

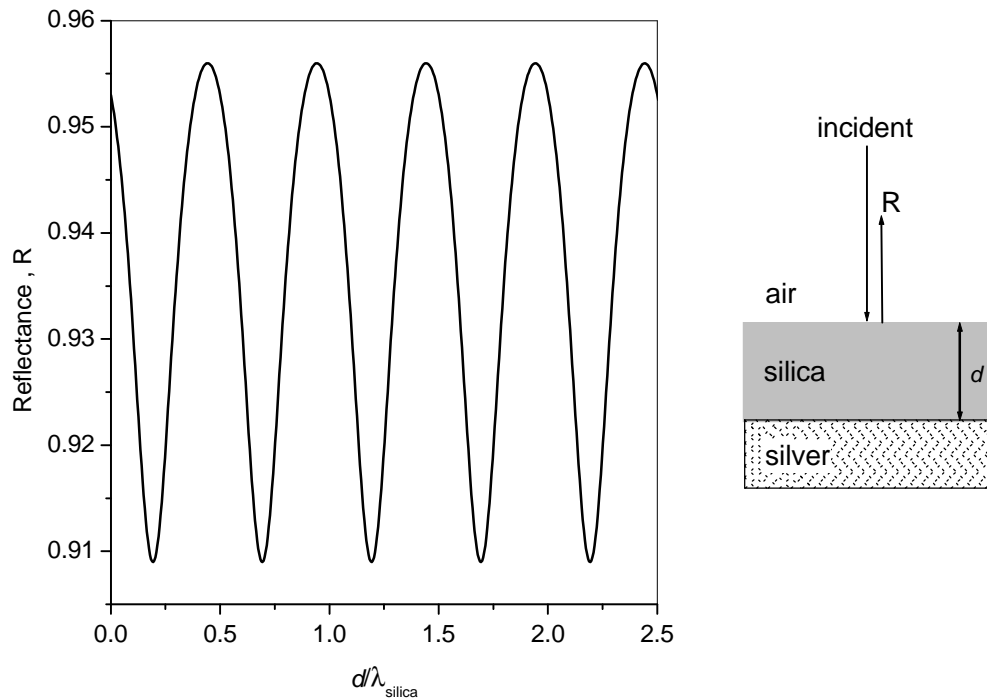


Figure 2.10 Reflectance, R , at normal incidence as a function of guide thickness, d . The structure is a silica ($\epsilon=2.12$) guiding layer bounded above by air ($\epsilon=1$) and below by silver ($\epsilon=-15+1.5i$).

In figure 2.10 the reflectance, $R=|r|^2$, at normal incidence is calculated for an air/silica/silver structure as a function of the silica guiding layer thickness, d . The troughs seen in R as guiding layer thickness is increased correspond to new partially guided modes being introduced. These features are regularly spaced by $d = \lambda_{\text{silica}}/2$, this corresponds to an equivalent phase condition for the waves guided in the silica. Guided modes occur when a wave and all resulting reflections are in phase in the guided layer, this gives constructive interference. If this phase condition is not met, then a wave in the guiding layer will be almost totally out of phase with some of its subsequent reflections. The width of the features seen in R corresponds to the width of the mode. For a lossless guiding region, the width of a waveguide mode is related to the magnitudes of the reflection coefficients as experienced by a guided wave. The lower the magnitude the broader the mode.

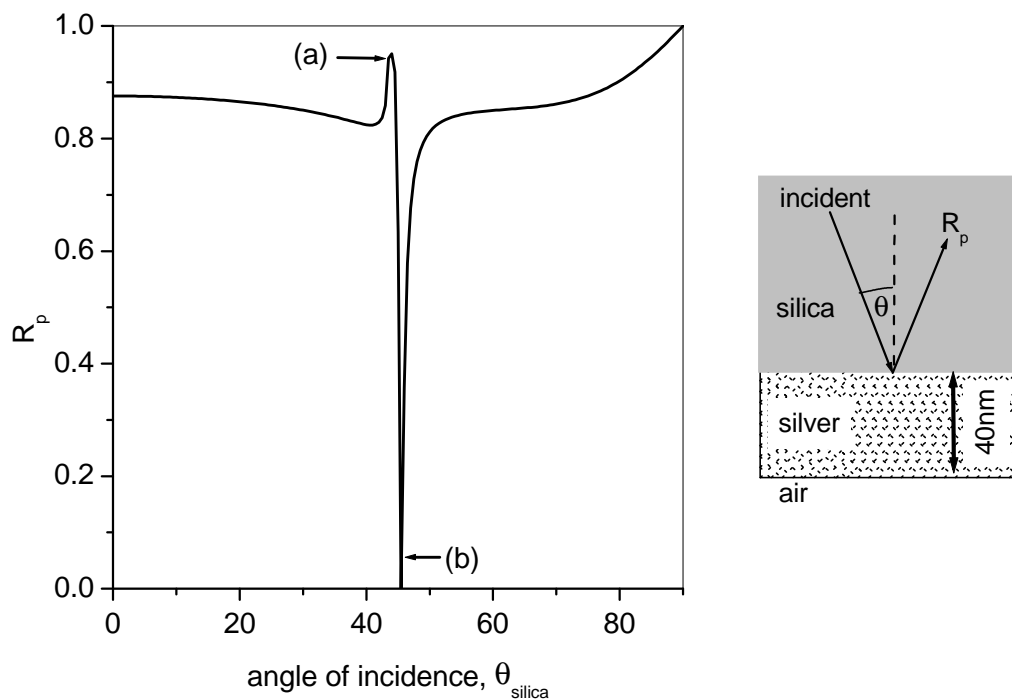


Figure 2.11 TM polarised reflectance, R_p , as a function of incident angle, θ , in the silica for a free space wavelength of 600nm. The structure is a 40nm thick silver ($\epsilon = -15 + 1.5i$) layer bounded above by silica ($\epsilon=2.12$) and below by air ($\epsilon=1$).

In figure 2.11 the reflectance for the TM polarisation, R_p , is plotted against angle of incidence for a wave incident from a region of silica onto a 40nm thick metal layer above a region of air. The sharp edge (a) at the left of the peak corresponds to a *critical edge* that defines the angle at which the wave changes from being propagating in the air to being evanescent. The narrow trough (b) is due to coupling to the SPP mode at the metal/air interface, and the drop in the reflectance corresponds to energy lost to absorption in the metal as the SPP mode propagates along the interface. This mode has fields that decay exponentially in both the metal and air, but which are sinusoidal in the silica. The higher index of the silica provides the extra momentum necessary for coupling radiation to this mode, which means that the mode is now radiative. The SPP mode that may be expected at the silica/metal interface is not evident in this plot. This is because the tangential wavevector of this mode exceeds that of any propagating wave in the silica. The width of the feature relates to the width of the mode, and is largely due to the absorption of the metal.

So far, in this chapter, we have looked at the types of modes that are typically present in planar structures. The dispersion relation for the surface bound SPP mode at a single metal/dielectric interface was derived, and the effect of coupling two such modes in a metal-clad waveguide structure was considered. The dispersion relations for the guided modes of a simple three layer guiding structure were also arrived at.

In the following section, we consider the behaviour of an electric dipole emitter. In particular, we look at a model that accounts for the modes of a planar structure and how such an emitter couples to them. This model will allow us to look at emissive structures.

2.3 Dipole emission

In this section we present an outline of a theory for modelling SpE in a planar microcavity. We use a classical theory that models the effects of nearby planar interfaces on the decay rate of an excited molecule using Maxwell's equations and appropriate boundary conditions [Born and Wolf (1970), Chance et al. (1978)]. This approach allows an examination of the different routes by

which power may be lost by the emitter; these include far field radiation, and absorption in the mirrors [Novotny (1997)].

The emitters are considered to be electric dipole oscillators, since many radiative molecular transitions are electric dipole in nature.

Several assumptions are made in this model:

- ◆ the media considered are isotropic in nature and are characterised by a dielectric permittivity ϵ ,
- ◆ the medium in which the dipole sits is non dissipative (i.e. purely real permittivity),
- ◆ the interfaces are infinite planes,
- ◆ the wavelength of the radiation λ and separation between emitter and any interface must both be large compared with the size of the dipole (point dipole approximation).

These assumptions are appropriate for modelling a wide range of physical situations. Again, we treat all of the materials as non-magnetic, since this holds for the systems considered in subsequent chapters.

The following analysis provides a general technique for calculating the effect of an emitter's environment on its decay rate. Using Kuhn's model for the behaviour of an electric dipole above a plane mirror [Kuhn (1970)], the dipole is treated as a forced damped harmonic oscillator. We say forced since the reflected field acts to drive the emission, and damped since the emitter radiates power. This model can be applied more generally to the case of an emitter in a microcavity. The equation of motion for the dipole is given by

$$\frac{d^2 p}{dt^2} + \omega^2 p = \frac{e^2}{m} E_R - D_0 \frac{dp}{dt} \quad (2.30)$$

where p is the dipole moment, ω is the oscillation frequency in the absence of all damping, e is the electric charge, m is the effective mass of the dipole, E_R is the component of the reflected electric field in the direction of the dipole, at the dipole site, and D_0 is the damping constant (inverse lifetime) in the absence of any interfaces.

The reflected field and dipole oscillate at the same complex frequency, such that a solution should take the form

$$\rho(t) = \rho_0 \exp[-(i\omega + i\Delta\omega + D/2)t] \quad (2.31)$$

$$E_R(t) = E_0 \exp[-(i\omega + i\Delta\omega + D/2)t] \quad (2.32)$$

where $\Delta\omega$ and D are the frequency shift and damping rate, respectively, in the presence of an interface.

Substituting equations (2.31) and (2.32) into (2.30), equating real and imaginary components, and noting that $\Delta\omega$ is very small (\sim MHz for optical transitions) compared to ω , we get

$$\Delta\omega \approx \frac{D^2}{8\omega} - \frac{DD_0}{4\omega} - \frac{e^2}{2\rho_0 m\omega} \text{Re}(E_0) \quad (2.33)$$

$$D = D_0 + \frac{e^2}{\rho_0 m\omega} \text{Im}(E_0) \quad (2.34)$$

We have the damping rate in the absence of any interfaces as [Kuhn (1970)]

$$D_0 = \frac{e^2 k_0^3 \sqrt{\epsilon_1}}{6\pi\epsilon_0 m\omega} \frac{1}{q} \quad (2.35)$$

where ϵ_1 is the relative permittivity of the medium in which the dipole is located, q is the quantum efficiency of the emitting state, and k_0 is given by $k_0 = \omega/c$. Equation (2.35) is obtained from a calculation of the time averaged power loss of the dipole, b_0 (see equation (2.48)). Equation (2.35) may be re-expressed in terms of the magnitude of the dipole moment, ρ_0 , using the relation $\rho_0^2 = 2e^2\hbar/m\omega$, which can be obtained by equating the kinetic energy of the oscillating charge to the energy of a photon of the same frequency. The damping rate is then given by $D_0 = b_0/\hbar\omega$. We can then re-express equation 2.34 as

$$\frac{D}{D_0} = 1 + \frac{6\pi\epsilon_0 q}{\rho_0 k_0^3 \sqrt{\epsilon_1}} \text{Im}(E_0) \quad (2.36)$$

where q , the quantum efficiency of the emission, essentially represents the probability of the emitter decaying radiatively in the case where the media in which the dipole is located is infinite (i.e. no interfaces). The value $(1-q)$ is therefore the probability of intrinsic non-radiative decay.

To find the relative change in the decay rate of the dipole upon introducing a nearby interface we need only determine the reflected electric field at the dipole site. Before the fields due to an emitter in a cavity can be calculated, we must know what the fields of an emitter in an infinite medium are.

2.3.1 Fields of an emitter in free space

We assume an implicit harmonic time dependence $\exp(-i\omega t)$ of all field components. The fields of an oscillating electric dipole in an homogeneous, isotropic medium are cylindrically symmetric and can be simply represented through the use of a Hertz vector $\mathbf{\Pi}$, such that [Sommerfeld (1949)],

$$\mathbf{\Pi} = \frac{\mathbf{p}_0 \exp(ikr)}{4\pi\epsilon r} \quad (2.37)$$

where k is the wavenumber, corresponding to ω , in the region of interest, \mathbf{p}_0 is the dipole moment, and r is the distance between the dipole and the point of observation. In terms of the Hertz vector the electric and magnetic fields are given by

$$\mathbf{E} = k^2\mathbf{\Pi} + \nabla\nabla \cdot \mathbf{\Pi} \quad (2.38)$$

$$\mathbf{H} = -i\omega\epsilon\nabla \wedge \mathbf{\Pi} \quad (2.39)$$

These fields satisfy the vector Helmholtz equation (wave equation),

$$(\nabla^2 + k^2)\mathbf{\Pi} = 0 \quad (2.40)$$

everywhere, except at the dipole site. Equation (2.37) can be re-expressed in cylindrical co-ordinates (ρ, ϕ, z) , in terms of eigenfunctions of equation (2.40), using the Sommerfeld expansion [Sommerfeld (1949), Chance et al. (1978)] such that,

$$\mathbf{\Pi} = \frac{i\mathbf{p}_0}{4\pi\epsilon} \int_0^\infty \frac{u}{n} J_0(uy) e^{in|z|} du \quad (2.41)$$

where J_0 is the zeroth order Bessel function, u is a variable of integration which corresponds to the value of the tangential wavevector, and $n=(k^2-u^2)^{1/2}$ corresponds to the component of the wavevector normal to the plane, with $\text{Im}(n) \geq 0$. This plane wave expansion facilitates solving the appropriate electromagnetic boundary conditions when considering the dipole near a planar

interface. The integrand is not continuous on the path of integration, so that the point where $u=k$ must be excluded when evaluating the integral numerically.

2.3.2 Fields of an emitter in a cavity

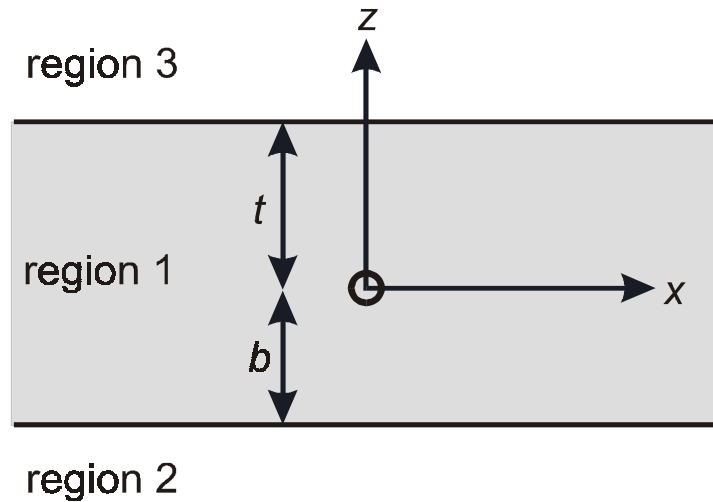


Figure 2.12 Geometry of the cavity problem. The dipole is at a height b above the bottom interface, and a distance t from the upper interface. The cavity thickness is given by $d = b + t$. The dipole lies at the origin of the co-ordinate axes.

The fields resulting from the introduction of a cavity environment, as depicted in figure 2.12, can then readily be determined in the manner used by Sommerfeld. This approach involves constructing a Hertz vector with our known source term, equation (2.41), and extra terms corresponding to reflected and transmitted fields in the system, an extension of equation (2.41), subject to the boundary conditions which must be satisfied at the interfaces $z=t, -b$ (see figure 2.12). These boundary conditions are that the tangential components of \mathbf{E} and \mathbf{H} are continuous at the interfaces. The corresponding boundary conditions for the Hertz vector can be found using equations (2.38) and (2.39); and are found to be that $\nabla \cdot \boldsymbol{\Pi}$, $k^2 \Pi_x$, $k^2 \Pi_z$ and $k^2 \partial \Pi_x / \partial z$ are continuous across the interfaces.

The resulting expressions for the two orthogonal orientations of emitter, described as those either perpendicular or parallel to the interfaces in the cavity

system, are thereby obtained. For the perpendicular dipole the Hertz vector is $\mathbf{\Pi}=(0,0,\Pi_z)$, where

$$\Pi_z = \frac{\rho_{0z}}{4\pi\epsilon_0\epsilon_1} \int_0^\infty W(u,z) J_0(up) du \quad (2.42)$$

with

$$W(u,z) = \begin{cases} i \frac{u}{n_1} \sqrt{\frac{\epsilon_1}{\epsilon_3}} T_{\perp p \uparrow} e^{in_3(z-t)+in_1 t} & z > t \\ i \frac{u}{n_1} \left[e^{-in_1|z|} + R_{\perp p \uparrow} e^{in_1(z+2b)} + R_{\perp p \downarrow} e^{-in_1(z-2t)} \right] & -b < z < t \\ i \frac{u}{n_1} \sqrt{\frac{\epsilon_1}{\epsilon_2}} T_{\perp p \downarrow} e^{-in_2(z+b)+in_1 b} & z < -b \end{cases} \quad (2.43)$$

and for the parallel dipole (oriented along the x -axis say) we have $\mathbf{\Pi}=(\Pi_x,0,\Pi_z)$, where

$$\Pi_x = \frac{\rho_{0x}}{4\pi\epsilon_0\epsilon_1} \int_0^\infty X(u,z) J_0(up) du \quad (2.44)$$

$$\Pi_z = \cos\phi \frac{\rho_{0x}}{4\pi\epsilon_0\epsilon_1} \int_0^\infty Y(u,z) J_1(up) du \quad (2.45)$$

with

$$X(u,z) = \begin{cases} i \frac{u}{n_1} \frac{\epsilon_1}{\epsilon_3} T_{\parallel s \uparrow} e^{in_3(z-t)+in_1 t} & z > t \\ i \frac{u}{n_1} \left[e^{-in_1|z|} + R_{\parallel s \uparrow} e^{in_1(z+2b)} + R_{\parallel s \downarrow} e^{-in_1(z-2t)} \right] & -b < z < t \\ i \frac{u}{n_1} \frac{\epsilon_1}{\epsilon_2} T_{\parallel s \downarrow} e^{-in_2(z+b)+in_1 b} & z < -b \end{cases} \quad (2.46)$$

and

$$Y(u,z) = \begin{cases} \left(\sqrt{\frac{\epsilon_1}{\epsilon_3}} T_{\parallel p \uparrow} - \frac{n_3}{n_1} \frac{\epsilon_1}{\epsilon_3} T_{\parallel s \uparrow} \right) e^{in_3(z-t)+in_1 t} & z > t \\ (R_{\parallel p \uparrow} - R_{\parallel s \uparrow}) e^{in_1(z+2b)} - (R_{\parallel p \downarrow} - R_{\parallel s \downarrow}) e^{-in_1(z-2t)} & -b < z < t \\ \left(-\sqrt{\frac{\epsilon_1}{\epsilon_2}} T_{\parallel p \downarrow} + \frac{n_2}{n_1} \frac{\epsilon_1}{\epsilon_2} T_{\parallel s \downarrow} \right) e^{-in_2(z+b)+in_1 b} & z < -b \end{cases} \quad (2.47)$$

The terms R , T and n_i are defined in appendix **A**. In the appendix, R and T are expressed in terms of the Fresnel reflection and transmission coefficients (section 2.2.4) for each interface in the system.

It should be appreciated that, though we have considered a simple 3-layer system, these expressions can easily be extended to account for more complicated systems. The effect of either interface in our 3-layer system is described simply by its Fresnel reflection and transmission coefficients. The effects of a multi-layer structure, such as a dielectric Bragg stack for example, can be reduced to identifying effective reflection and transmission coefficients for that structure [Sipe (1981)]. In this way it is possible to effectively treat multiple layers as a single interface (see section 2.2.4). As such, a more complex multi-layer system can be reduced to the 3-layer system outlined here.

Having determined the fields in this system, we are then able to determine the Poynting vector. The energy flux into the far field, and through an interface bounding a lossless region containing the emitter, may each be evaluated in this way. We are thus able to obtain expressions for the decay rate of the emitter and for the power radiated into the far field [Tomas and Lenac (1993)]. The decay rate of the emitter may also be found using equation (2.36), which makes use of the component of the reflected electric field in the direction of the dipole, at the dipole site.

2.3.3 Cavity modification to SpE

The time averaged power loss of a dipole located in an infinite medium corresponding to region 1 (see figure 2.12), is given by,

$$b_0 = \frac{\rho_0^2 \omega k_0^3 \sqrt{\epsilon_1}}{12\pi\epsilon_0} \frac{1}{q} \quad (2.48)$$

where q is the quantum efficiency of the emitter (such that $(1-q)b_0$ is the non-radiative power loss of the emitter). Equation (2.48) may be obtained by construction of a Poynting vector which, when integrated over a surface surrounding the dipole, would give the time averaged radiative power loss of the emitter b_r (where $b_r = qb_0$). By obtaining the total decay rates of vertical and horizontal dipole emitters [Chance et al. (1978)], normalised with respect to the rate in the absence of the microcavity, we find an expression for the decay rate of an isotropic distribution of emitters as,

$$\frac{b}{b_0} = (1 - q) + \frac{1}{2} \frac{q}{k_1^3} \operatorname{Re} \int_0^\infty \left[\begin{array}{l} u^2 (1 + R_{\perp\rho\uparrow} e^{2in_1 b} + R_{\perp\rho\downarrow} e^{2in_1 t}) \\ + k_1^2 (1 + R_{//s\uparrow} e^{2in_1 b} + R_{//s\downarrow} e^{2in_1 t}) \\ + n_1^2 (1 + R_{//\rho\uparrow} e^{2in_1 b} + R_{//\rho\downarrow} e^{2in_1 t}) \end{array} \right] \frac{u}{n_1} du \quad (2.49)$$

where $k_1 = \sqrt{\epsilon_1} \omega/c$. The contributions from each dipole orientation, where \perp and $//$ correspond to vertical and horizontal orientations respectively, are clearly grouped within the square brackets of the integrand. For many cases of interest the dipole orientation is isotropic, by which we mean a dipole whose moment rotates and samples all directions in space in a time much shorter than the fluorescence lifetime. This case may be described by a combination of vertical and horizontal emitters, weighted by a factor of 1/3 and 2/3 respectively.

2.3.4 Coupling to cavity modes

In this section, we will consider how an emitter couples to the modes of a microcavity. To do this we use the example of a dipole emitter located within a symmetric metal-clad cavity. The system comprises two semi-infinite regions of metal ($\epsilon_{\text{metal}} = -15 + 1.5i$) separated by a layer of air ($\epsilon = 1$) of thickness d . By using the model described in section 2.3.3, we may determine how strongly a dipole emitter couples to the modes of the cavity. By considering the field profiles of these modes, and the position and orientation of the emitter, the coupling conditions are investigated.

In figures 2.13 and 2.14, the decay rate is plotted as a function of mirror separation for dipoles oriented perpendicular and parallel to the mirrors respectively. In each case, the emitter oscillates with a single frequency, corresponding to a free space wavelength λ , and is located in the centre of the cavity. For simplicity we set $q=1$. Also shown in each figure is a grey scale that relates to the contribution to the decay rate as a function of in-plane wavevector u . The greyscale corresponds to the integrand of equation (2.49), where dark is high and white is low. In both figures particular modes of the structure are clearly indicated by the strong coupling of the emitters to the modes (these are the very dark features in the greyscale plots).

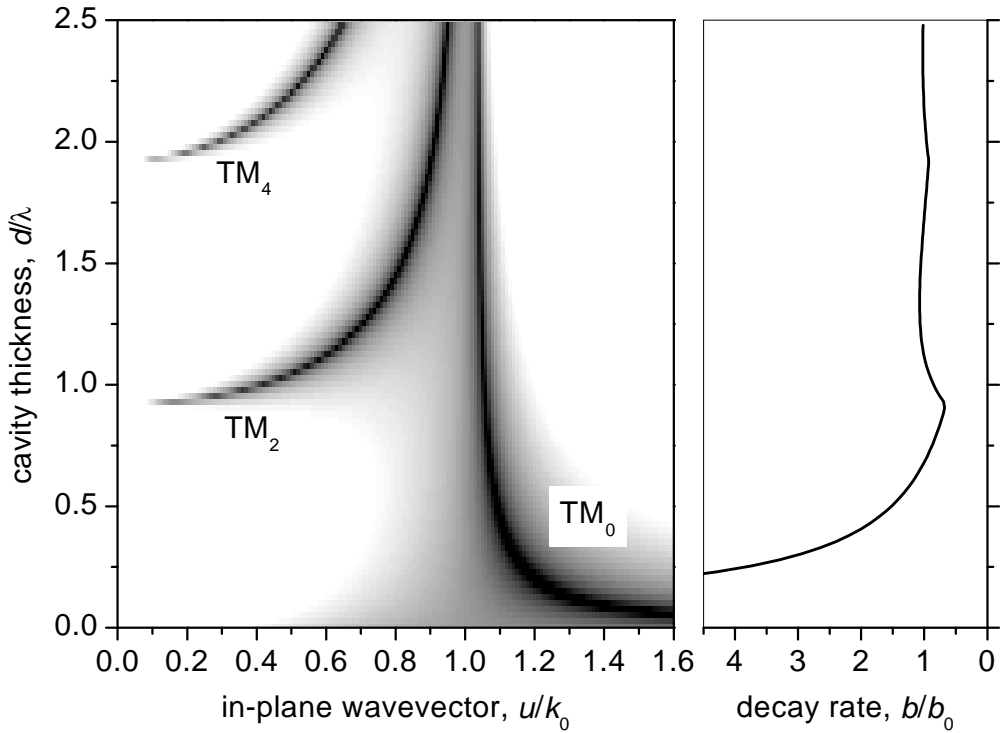


Figure 2.13. For an emitter with a perpendicular dipole orientation that is located in the middle of a metal-clad microcavity, the greyscale indicates the dispersion of the modes to which the emitter couples. The decay rate of the emitter as a function of cavity thickness is also shown.

From figure 2.13, we see that the perpendicularly oriented dipole moment only couples to the even labelled TM polarised modes. The emitter can only couple to TM modes as only the z -component of the \mathbf{E} field can act to drive the emitter. It is because of the symmetry of the cavity that the odd labelled TM modes have a node in the E_z component of the field at the middle of the cavity, which is where the dipole is located. Conversely, the even labelled TM modes have an anti-node of the E_z field component at the dipole site, which accounts for the very strong coupling between the dipole and these modes. The effect of introducing new modes as the cavity thickness is increased is seen as an increase in the decay rate of the emitter, if the emitter can couple to them, as they represent additional decay routes. It is also clear that the perpendicular emitter can always couple to the LRSP (section 2.2.3) mode (TM_0) of the structure, and that the power lost to this mode is very large for small mirror separations ($d < \lambda/4$).

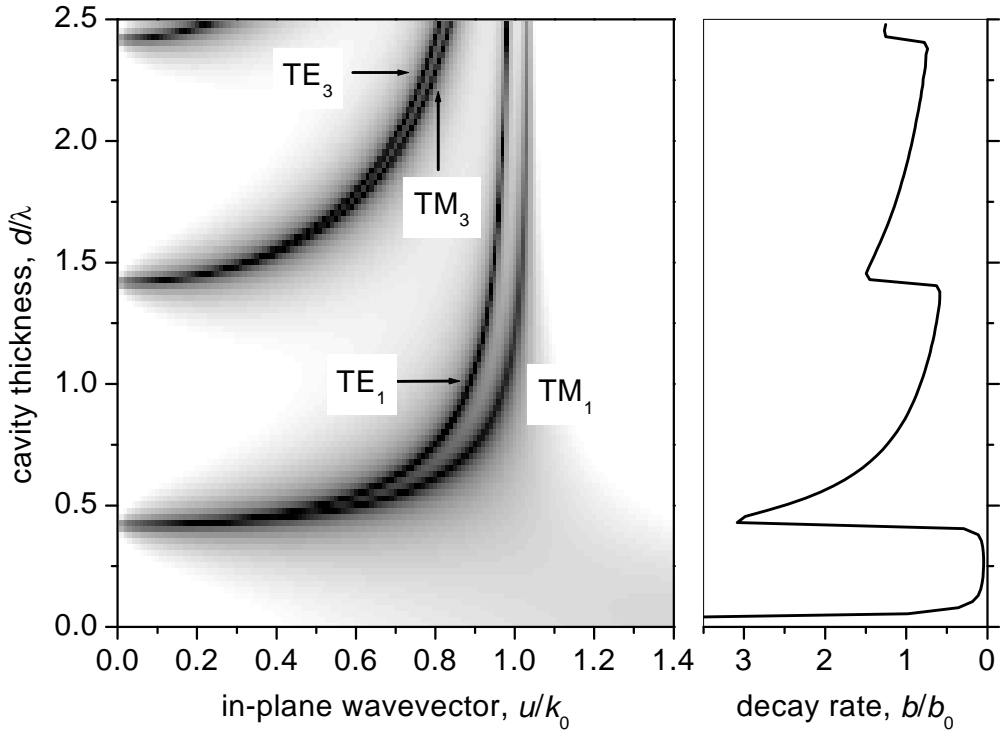


Figure 2.14 For an emitter with a parallel dipole orientation that is located in the middle of a metal-clad microcavity, the greyscale indicates the dispersion of the modes to which the emitter couples. The decay rate of the emitter as a function of cavity thickness is also shown.

In figure 2.14, the decay rate for the dipole oriented parallel to the mirrors is shown as a function of mirror separation. The emitter, in this case, couples only to the odd labelled TE and TM modes of the cavity. The orientation of the dipole means that only an \mathbf{E} field component in the plane of the mirrors can affect the emitter. For both polarisations the even labelled modes have a node in the tangential component of the \mathbf{E} field at the emitter site, due to the symmetry of the structure. Unlike the perpendicular dipole orientation, there is a cavity thickness ($d < \lambda/2$) below which there are no cavity modes for the parallel dipole to couple to. The introduction of new cavity modes that the emitter can couple to results in a more significant increase in the decay rate of the parallel dipole than the perpendicular dipole orientation. This is partly because the horizontal dipole couples to both polarisations, when the perpendicular dipole can only couple to the TM modes. But, it is also because the modes are

introduced near cut-off, at normal incidence ($u=0$), which is a direction in which the perpendicular dipole can not couple.

This section has been concerned with the conditions for coupling between an emitter and the modes of a microcavity. The structure that we investigated was a symmetric metal-clad cavity. This is a structure that does not have radiative modes associated with it, as all fields decay exponentially away from the cavity. In the next section we will consider the effects of a microcavity with at least one partially transmitting mirror, which means that an emitter in such a structure may couple to radiative modes.

2.3.5 Far field radiation

Referring to figure 2.12, assuming region 3 is non-dissipative, the energy radiating into region 3 can be determined. Since the fields in the far field region (region 3) are known (section 2.3.2), a Poynting vector can be constructed. Using this Poynting vector, the power flux through an appropriate surface, and hence the power radiated into that far field region, can be calculated [Novotny (1997)]. The general form of the Poynting vector calculation is given by

$$P = \frac{1}{2} \text{Re} \left[\int_S (\mathbf{E} \wedge \mathbf{H}^*) \cdot \mathbf{n}_s ds \right] \quad (2.50)$$

where P is the time averaged power flow through a surface S , and ds is an element of surface area, and \mathbf{n}_s is a unit vector that is perpendicular to the surface S . The energy radiating into region 3 due to an isotropic distribution of emitters (i.e. an isotropic dipole moment that is equivalent to a large sample of randomly-oriented emitters), having first determined the contribution from each of the two orthogonal orientations, is therefore given by

$$\frac{b_3}{b_0} = \frac{q}{4k_1^3} \int_0^{k_3} u n_3 \left(k_1^2 \frac{\epsilon_1}{\epsilon_3} \left| \frac{T_{//s\uparrow}}{n_1} e^{in_1 t} \right|^2 + \left| T_{//p\uparrow} e^{in_1 t} \right|^2 + u^2 \left| \frac{T_{\perp p\uparrow}}{n_1} e^{in_1 t} \right|^2 \right) du \quad (2.51)$$

where the terms T and n_i are given in appendix **A**. As with the previous decay rate expression, the contributions from each orientation of emitter, and polarisation, can easily be distinguished within the integrand. Equation (2.51) is equivalent to the results given by Tomas and Lenac (1993). In the above

equation, the variable of integration u can be changed to θ_3 , the angle of propagation in region 3, according to the relation $u=k_3\sin\theta_3$, and the integral can be re-expressed to give

$$\frac{b_3}{b_0} = \frac{q^{\pi/2}}{4} \int_0^{\pi/2} F(u) \sin\theta_3 d\theta_3 \quad (2.52)$$

where $F(u)$ is a relative measure of the intensity into a particular solid angle characterised by θ_3 , given by

$$F(u) = \frac{k_3 n_3^2}{k_1^3} \left(k_1^2 \frac{\epsilon_1}{\epsilon_3} \left| \frac{T_{//s\uparrow}}{n_1} e^{in_1 t} \right|^2 + |T_{//p\uparrow} e^{in_1 t}|^2 + u^2 \left| \frac{T_{\perp p\uparrow}}{n_1} e^{in_1 t} \right|^2 \right) \quad (2.53)$$

Equation (2.53) is equivalent to the model used by Drexhage (1974) in determining the radiation patterns from emitters placed within planar systems. The range of integration in equation (2.52) can be restricted, allowing the amount of energy radiated within a chosen angular range to be calculated.

2.4 Summary

The decay of an excited molecule can be greatly modified by a microcavity environment. For an emitter in a cavity, decay (not including any intrinsic decay) will only be to modes that the structure supports. We have looked at the SPP and waveguide modes that are commonly present in guiding structures, and the dispersion for both the TM and TE polarised modes in a two-interface guiding structure have been derived. By considering a dipole in a metal-clad waveguide, the conditions for the coupling between an emitter and these modes have been investigated. Essentially, an electric dipole can only couple to a mode that has a non-zero component of its electric field in the direction of the dipole moment, at the emitter site. Finally, in this chapter, we presented some expressions for calculating the power radiated into the far field by an emitter in a cavity. In chapter 3 we use such expressions to investigate how well different microcavity structures perform in controlling emission from sources embedded within them.

Chapter 3

Efficiency of emission from planar microcavities

3.1 Introduction

In this chapter, a computational model, based on the theory outlined in section 2.3, is used to investigate the different routes by which power is lost by an optical emitter placed in a microcavity environment. We focus our attention on parameters appropriate for organic microcavity light emitting diode structures. A key issue is extraction of power from sources within thin films, since many emissive devices (e.g. the light emitting diode) have a layered structure. In addition, a cavity can modify the direction and overall rate of an emitter's decay. The cavity geometry may then be exploited, since an appropriate structure could restrict emission to favourable directions (corresponding to radiation into the far field), that would result in a more efficient device. For a dielectric layer bound by regions of air, only light emitted below the critical angle for propagation in the air has a chance of escaping the dielectric layer. The greater the refractive index of such an emitting layer, the smaller the range of angles within the dielectric that may result in radiation into the air.

We make a quantitative investigation of the $1/2n^2$ model (where n is a refractive index) used by many workers in evaluating the fraction of power radiated from a thin film of emitting material. We also show the limitations of the $1/2n^2$ model, emphasising the important role of the orientation of the dipole moment of the emitters. Multi-layer systems, involving dielectric Bragg stack reflectors and metal mirrors, are compared for their efficiency in producing useful radiation. Both a standard Bragg reflector and the recently developed omni-directional Bragg stack (which is highly reflecting from 0° to 90° angle of incidence for a range of frequencies) are considered. It is shown that metal mirrors, though lossy, may still be effective for producing useful radiation from microcavities.

It has been shown above (see chapter 2.3) that spontaneous emission is not an intrinsic property of an emitter, but can be modified by the structure of the emitter's environment [Purcell (1946)]. The effects of nearby planar interfaces on the decay rate of a dipole emitter have been extensively investigated [Drexhage (1974), Chance et al. (1987), Sipe (1981), Tomas and Lenac (1997)]. Modifying the spontaneous emission of a molecule has major applications in devices such as light emitting diodes (LEDs), where the interest is in optimising both the decay rate and decay routes of optical emitters [Abram et al. (1998), Meschede (1992), Baba et al. (1991)]. In particular, an efficient emissive device requires that the fraction of the total power that radiates into the far field, usually within a specific solid angle, be as large as possible.

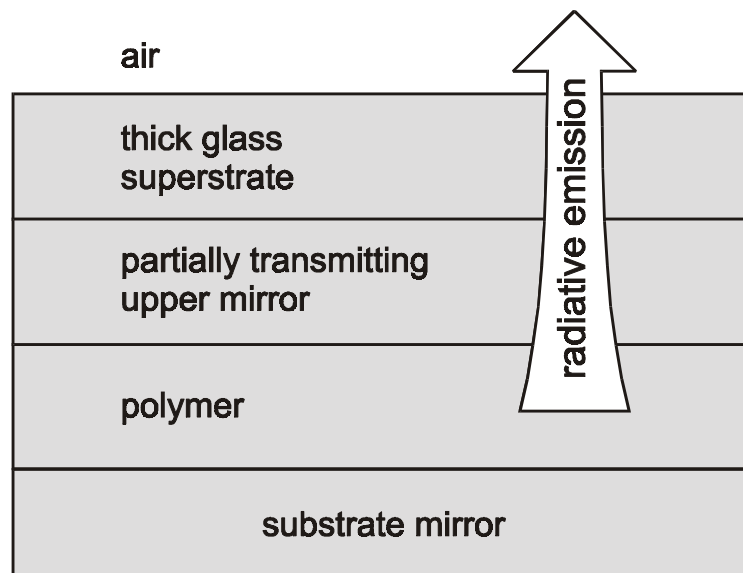


Figure 3.1 Basic structure of the system examined in this chapter. The emitters reside in the polymer layer.

Microcavities have been extensively exploited in this regard [Dodabalapur (1997)]. The emissive layer is bounded by two mirrors, at least one of which is partially transmissive, see figure 3.1. Typically the mirrors are either dielectric Bragg stack reflectors (DBRs) or metals; the best choice is investigated here and to some extent depends on the emissive materials being used [Becker et al. (1997)]. Further, some devices require electrical contacts in addition to mirrors, especially the LED, so that a compromise between electrical and optical performance may be necessary. Whilst producing relatively high

reflectivity for a wide range of incident angles, metals also introduce loss into the structure. Dielectric stack mirrors typically have lower losses, but are highly reflecting only over a limited angle range. This limitation may be overcome if materials of sufficiently high average refractive index and sufficiently high refractive index contrast are used, thereby producing an omni-directional DBR [Fink et al. (1998), Russel et al. (1999), Chigrin et al. (1999)], however such contrast has not yet been demonstrated in practical optical devices. Omni-directional DBRs have been theoretically shown to offer high reflection for all angles of propagating incident light. As such, the use of omni-directional DBRs has been suggested as a way to provide microcavities with strong optical confinement. In this chapter we investigate the effect of different microcavity structures on the power radiated into the far field of the system by emitters placed within the cavity; we take care to account for the different loss mechanisms within the structures considered. In contrast to other recent work, we concentrate here on structures and materials appropriate to LEDs in which conjugated polymers form the emissive material.

3.2 Assessing the radiative efficiency of different structures

In this section a number of different multi-layer structures are investigated with a view to optimising the fraction of the emitted power that emerges as useful radiation, generally defined as power radiating into a particular far field region of the system. The modelling in each case assumes there is no intrinsic power lost by the electric dipole emitters, i.e. $q=1$. For each system considered, the emitters radiate with a wavelength of 614 nm in free space. All values for rates and power radiated into a particular region are normalised with respect to b_0 (equation 2.48). In section 3.2.1 we investigate the effect a single interface has on an emitter. In section 3.2.2 we investigate the effectiveness of various LED structures to help build our physical understanding.

3.2.1 The single interface

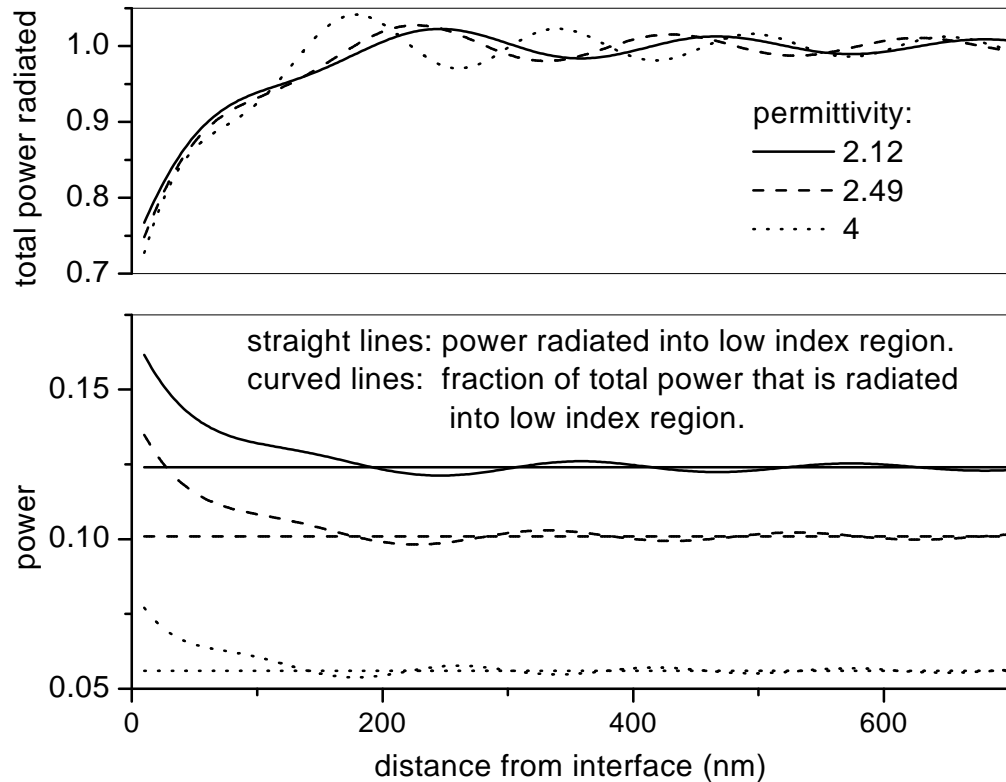


Figure 3.2 Emitters are located in a high refractive index material close to the interface with a low index material ($\epsilon=1$). The rate and amount of power radiated into the low index region are plotted as functions of the emitter-interface separation distance. Data are shown for three values of the permittivity of the high index region: $\epsilon=2.12$ (silica), $\epsilon=2.49$ (characteristic of the LB films used in Drexhage type experiments), and $\epsilon=4$ (typical of some of the polymers used in microcavity LEDs).

We start by analysing the simple system of a layer of randomly-oriented incoherent emitters located near the interface between two lossless dielectric media. The emitters are located in the medium of higher index, and the low index medium is air ($\epsilon=1$). The presence of this interface imposes a limitation on the power radiated into the low index region, this is because for in-plane wavevectors $>k_0$ (angles greater than the critical angle) total internal reflection occurs. In figure 3.2 we have plotted both the total power radiated and the

amount of power radiated into the low index region, as functions of the separation distance between the emitters and the interface. Data are shown for three different values of the permittivity of the high index region. The amount of power propagating into the low index region, for each system, is independent of the separation between emitter and interface, as indicated by the straight lines in figure 3.2. This is because no interference conditions apply to the radiation transmitted through the interface. In contrast power radiated into the high index region is subject to the interference condition between the direct radiation from the emitter and the radiation reflected from the interface. As a result the amount of power radiated into the high index region does depend on the separation distance. Consequently the total power, and thus the fraction of power radiated into the low index region, also depends on the separation, as shown in figure 3.2. As expected the amount of power that is transmitted into the low index region falls with increasing index, we also note that the horizontal orientation makes a greater contribution than the vertical one (see figure 3.3).

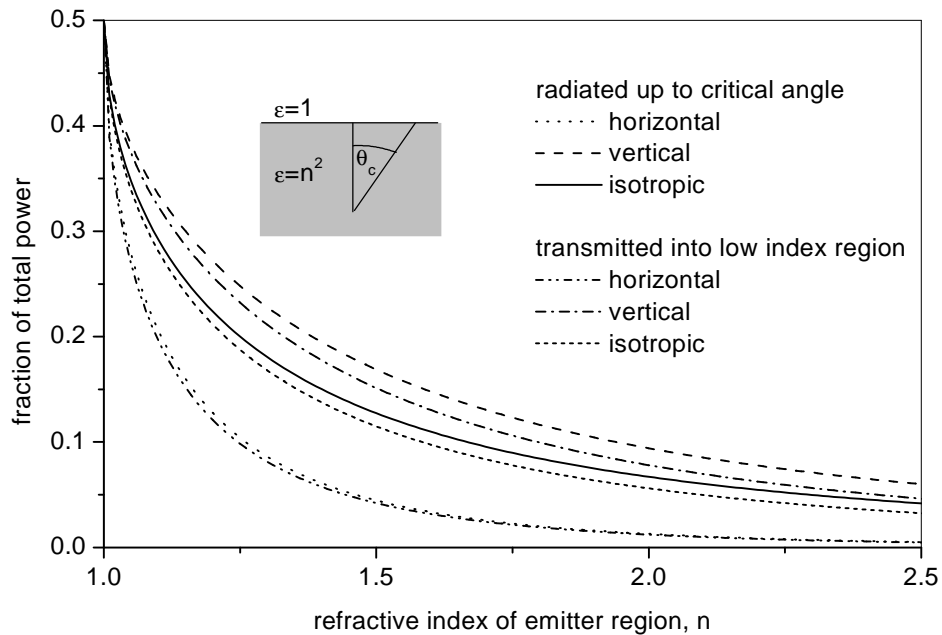


Figure 3.3 The fraction of total power that is radiated by the emitter up to the critical angle (θ_c) for transmission into the low index region, and the actual amount of power transmitted into the low index region, as functions of the index of the emitter region. Results for vertical and horizontal dipole orientations and an isotropic distribution are plotted.

Radiation from the emitter may escape into the low index region provided the angle of emission is less than the critical angle, all emission at higher angles is totally internally reflected and is therefore confined to the high index region. However, in this single interface system not all radiation at angles below the critical angle escapes into the low index region, some is reflected. The amount that is transmitted is shown in figure 3.3, where we have plotted the amount of power radiated into the low index region, as a function of the index of the emitter medium. Results are shown for the vertical and horizontal dipole orientations and an isotropic distribution.

Many planar emissive systems comprise a thin film of emissive material supported on a reflecting substrate. Typically this mirror has simply been assumed to provide a mechanism for ensuring that all radiation emitted with angles less than the critical angle (initially emitted in the upward **and** downward directions) is eventually radiated. The total solid angle for which this criterion is satisfied we refer to as the solid angle of radiation, Ω_R , where $\Omega_R = 4\pi(1 - \cos \theta_c)$. Provided the emitters radiate isotropically, and the refractive index of the film is high, then this solid angle is well approximated by $1/(2n^2)$ of the total [Greenham et al. (1994)]. We refer to this as the $1/(2n^2)$ model. This simple geometric model ignores the phase relationship between the source and reflected fields, which should be taken into account if an accurate calculation is to be performed.

Assuming for the moment that this phase condition is not important, as in the case of a very thick emissive layer, the power radiated upward at angles less than the critical angle for the two dipole orientations, is given by

$$\frac{b_{\perp}(\theta_c)}{b_0} = \frac{1}{4} (2 + \cos^3 \theta_c - 3 \cos \theta_c) \quad (3.1)$$

$$\frac{b_{\parallel}(\theta_c)}{b_0} = \frac{1}{8} (4 - \cos^3 \theta_c - 3 \cos \theta_c) \quad (3.2)$$

Equations (3.1) and (3.2) are obtained by calculating the energy flux through the appropriate surfaces. The results for the vertical and horizontal dipole orientations and an isotropic distribution are also shown in figure 3.3, as

we expect, these values are greater than the corresponding amounts of power transmitted into the low index region through the single interface.

These results are now compared with those obtained from the $1/(2n^2)$ model. The $1/(2n^2)$ result is obtained by combining equations (3.1) and (3.2) to obtain the result for an isotropic distribution of emitters. The $\cos\theta_c$ terms are then represented by a binomial expansion in terms of $1/n$, where we retain only terms up to the lowest order in $1/n$. This is a valid approximation for large values of the refractive index of the emitter medium, n . The final result needs multiplication by a factor of two, to account for radiation initially propagating in the downward direction.

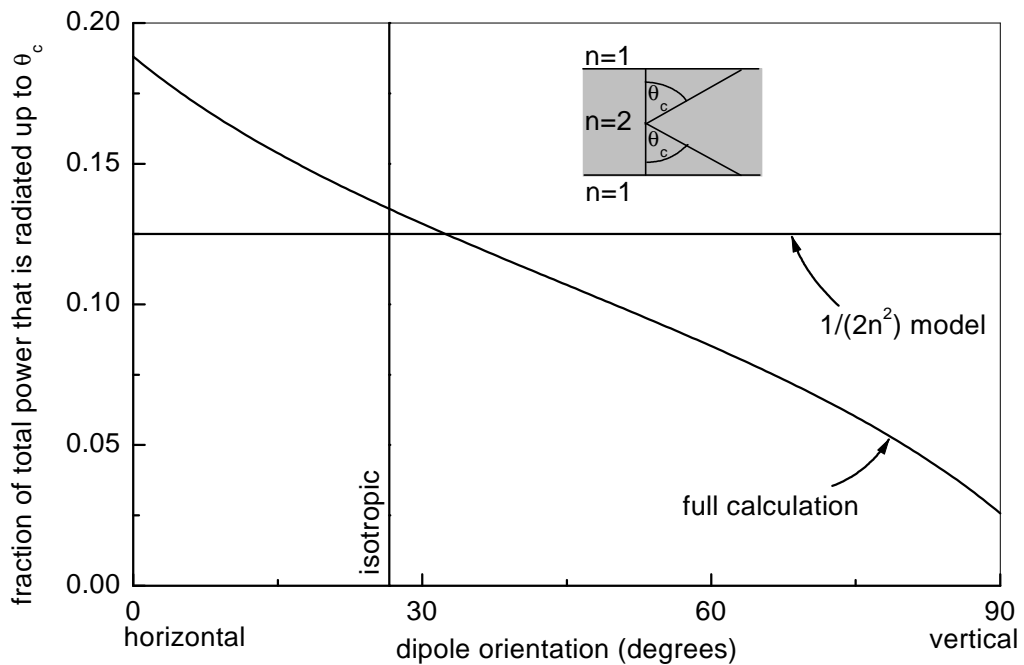


Figure 3.4 The fraction of total power that is radiated by the emitter up to the critical angle for transmission into the low index region, as a function of dipole orientation. The emitter layer has an index $n=2$, and is embedded in a low index region, which is air.

In figure 3.4, the result of the $1/(2n^2)$ model is shown. We consider an emissive medium with a typical polymer index of $n=2$ [Gymer et al. (1993)], radiating into air. For comparison we also show the result of a calculation for the power that is radiated into all angles less than the critical angle, in both upward

and downward directions, using the model outlined above, from equations (3.1) and (3.2). Results are shown as a function of dipole orientation, the orientation corresponding to an isotropic distribution of dipole emitters is also indicated.

Figure 3.4 shows that there is a strong dependence of the fraction of total power that is radiated into the air on the dipole orientation. For polymers such as PPV and excitons in quantum wells the dipole moment is predominantly horizontal [McBranch et al. (1995)]. If the $1/(2n^2)$ model is used in this case then it will lead to an overestimate of the radiative efficiency (the total amount of power radiated within the polymer layer). This can be by as much as a factor of 3/2, in the high index limit and where the dipole moment of the emitters is horizontally oriented. Looking back at figure 3.3, the importance of dipole orientation can again be seen, vertically orientated emitters clearly make no significant contribution when the ratio of the indices is large. This result is an important one and has been noted before [Tomas and Lenac (1993), Benisty et al. (1998)], it indicates that the orientation of the dipole moment in thin film emissive devices has an important bearing on their effective radiative efficiency.

3.2.2 Multi-layer cavities

Now some typical polymer LED structures are considered. For simplicity we restrict ourselves to a single emission frequency, and examine two cases for the dipole orientation, the horizontal and the isotropic case (these are the two common orientations in practical systems). The system comprises an emissive layer corresponding to the polymer ($\epsilon=4$) upon an Aluminium substrate ($\epsilon = -70 + 30i$) which forms one of the required electrical contacts. The polymer layer is bound above by a thin layer of either Indium-Tin Oxide (ITO, $\epsilon=3.5+0.05i$) or Au, which provides the other electrical contact, and a glass superstrate completing the structure. We consider the effects of varying the 'strength' of this upper mirror, by varying the Au layer thickness and placing different DBR mirrors above the ITO layer. Each standard (omni-directional) DBR is made from m -pairs of dielectric layers, with a $\lambda/4$ thick low index layer $\epsilon=2.12$ ($\epsilon=9$) above a $\lambda/4$ thick high index layer $\epsilon=5.13$ ($\epsilon=25$) constituting a single pair. The effects of the cavity environment on an emitter are modelled for an emitter located at different positions in the emissive layer. Only polymer layer

thickness are considered that correspond to cavities that support a single cavity guided mode; these cavities are approximately $\lambda/2$ thick.

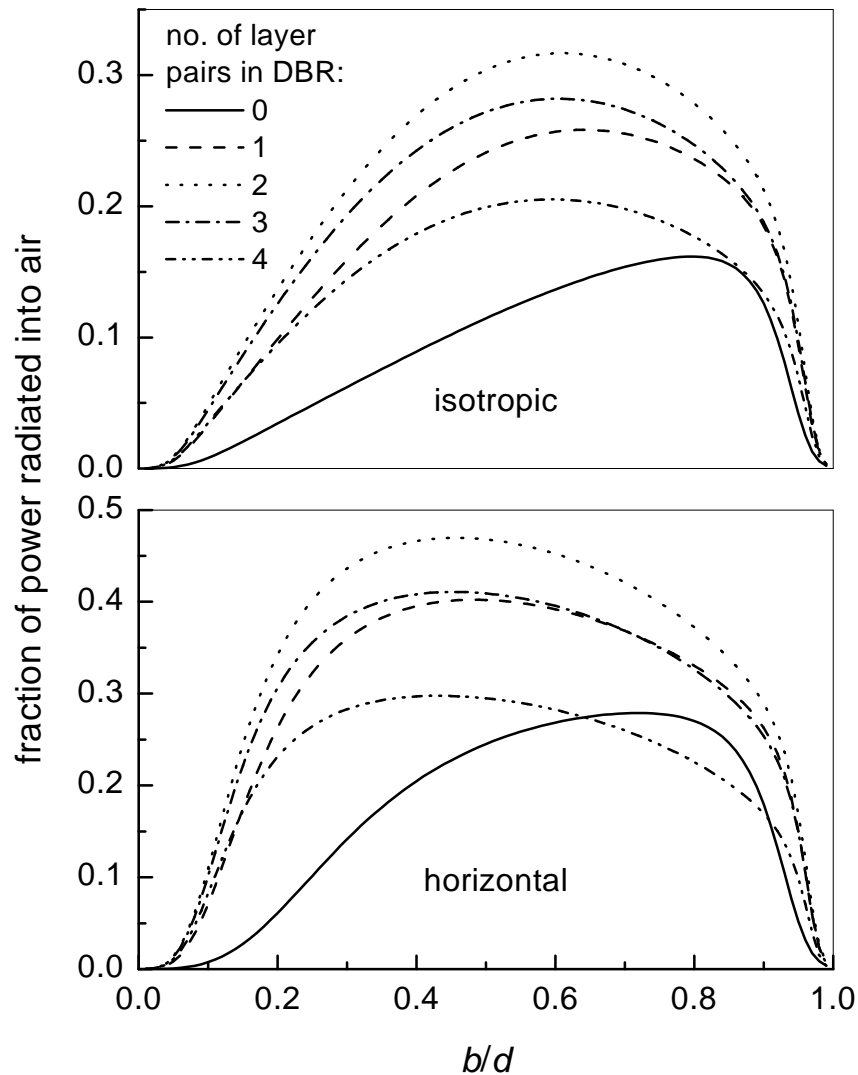


Figure 3.5 The fraction of the total power that is radiated out of the $\lambda/2$ Al/polymer/ITO/DBR system, as a function of the emitter's position in the emissive layer (described by the distance of the emitter above the Al substrate, b , divided by the emissive layer thickness, d). Data are shown for 0, 1, 2, 3 and 4 layer pairs, which make up the standard DBR. The emissive layer is 73, 112, 118, 118 and 120 nm thick respectively for the case of the isotropic emitters, and 59, 110, 117, 117 and 123 nm thick for the horizontally oriented emitters. These thicknesses are chosen to optimise the fraction of power radiated into the air.

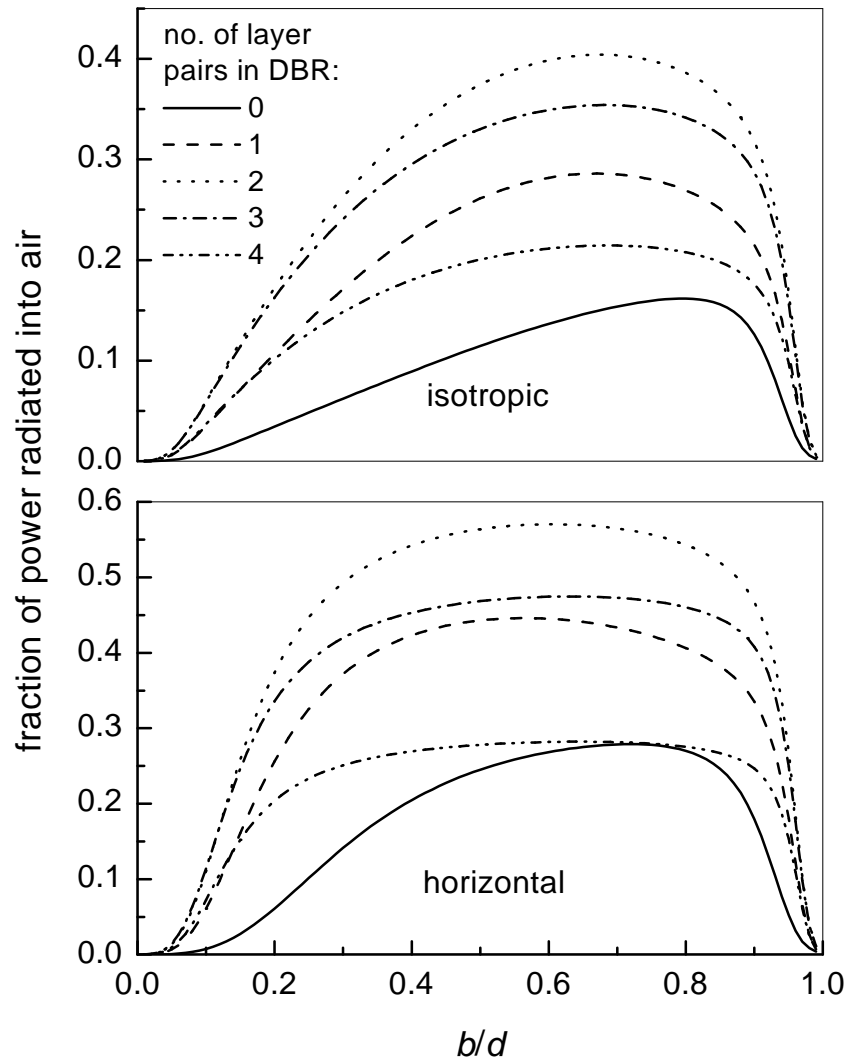


Figure 3.6 The fraction of the total power that is radiated out of the $\lambda/2$ Al/polymer/ITO/DBR system, as a function of the emitter's position in the emissive layer. Data are shown for 0, 1, 2, 3 and 4 layer pairs, which make up the omni-directional DBR. The emissive layer is 73, 106, 110, 111 and 111 nm thick respectively, for the case of the isotropic emitters, and 59, 101, 107, 109 and 109 nm thick for the horizontally oriented emitters.

First consider the system of an Al substrate, polymer layer, 40nm ITO layer, m -pair dielectric stack, topped by a thick silica layer, as shown in figure 3.1. In figures 3.5 and 3.6, we have plotted the fraction of an emitter's total power that is radiated into the air half space, for the standard and omni-directional DBRs respectively. This has been done as a function of the emitter's

position in the emissive layer. The results are shown when using 0, 1, 2, 3, and 4 layer-pairs in the DBR to see how the top mirror affects emission. In each case the emissive layer thickness was slightly altered to maximise the fraction of power radiated, since the field confinement within the cavity is altered by changing the top mirror. There is clearly an optimum number of two pairs to be used given all the other parameters in the model, this is similar to the findings of Benisty et al. (1998), and is true for both the standard and omni-directional DBR. The thickness of the ITO layer has a significant effect on the thickness of the emissive layer that should be used to obtain the maximum coupling of the emitter to radiation in the air. This is because the indices of both media (ITO and polymer) are approximately equal and it is really the composite thickness of the two layers that determines the order of the cavity modes that are supported. Our choice of an ITO layer thickness of 40nm means that the lowest order cavity mode has a field maximum in the polymer layer where the emitters can be driven more effectively. If the ITO layer thickness were much greater, then the lowest order cavity mode would have a field maximum in the ITO, which would be of little use in driving the emitters effectively.

We next consider what happens when the DBR mirror and ITO layer are changed for a mirror made from gold ($\epsilon = -11.5 + 1.15i$) (gold is an effective electron injecting contact for LEDs based on polymers). In figure 3.7 the fraction of an emitter's total power that is radiated into the air is plotted as a function of the emitter's position in the emissive layer. The results for different thicknesses of the Au layer are shown, and again in each case the emissive layer thickness was slightly altered to maximise the fraction of power radiated. There is an optimum thickness of about 20nm to be used for the gold mirror.

The similarity of the results for DBR and metal top mirrors, which are structurally quite different, may seem surprising. The metal clad cavity performs in a manner comparable to the system constructed with a standard Bragg mirror. However, it is clearly the structure involving the omni-directional mirror that performed best.

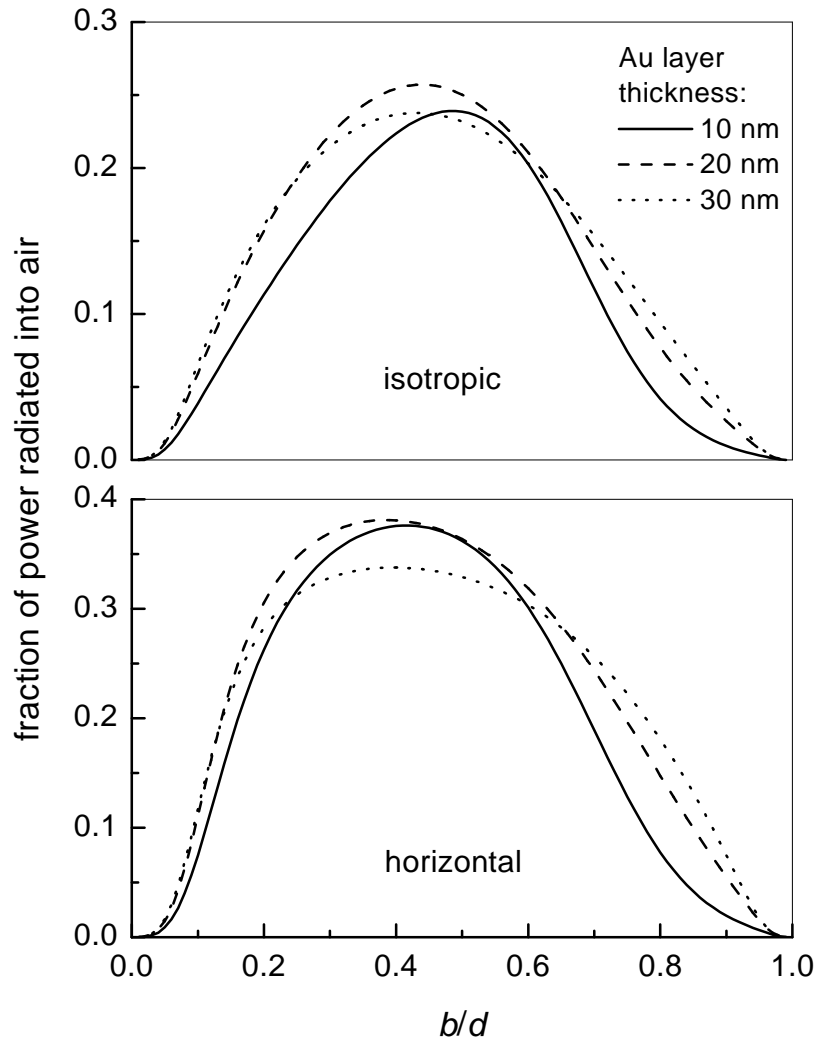


Figure 3.7 The fraction of the total power that is radiated out of the $\lambda/2$ Al/polymer/Au system, as a function of the emitter's position in the emissive layer. Data are shown for an Au layer thickness of 10, 20 and 30nm. The emissive layer is 112, 117 and 119 nm thick respectively, for the case of the isotropic emitters, and 108, 115 and 118 nm thick for the horizontally oriented emitters.

One effect of having a more reflecting top mirror, achieved by either having more layer pairs in the Bragg stack or increasing the Au layer thickness, is to sharpen the modes in the system. For low order cavity systems, where there may be just a single partially guided mode, it is then possible to control the width of this mode and direct the power radiated from the cavity within a

desired angular range. For systems with a lossy bottom mirror, it is clear that there is a trade off between narrowing the angular width of these radiative modes and extracting a significant total amount of power as far field radiation. A desirable LED structure will generally involve a large proportion of the emitter's energy being radiated perpendicular to the surface, with minimal losses to high angles and non-radiative modes.

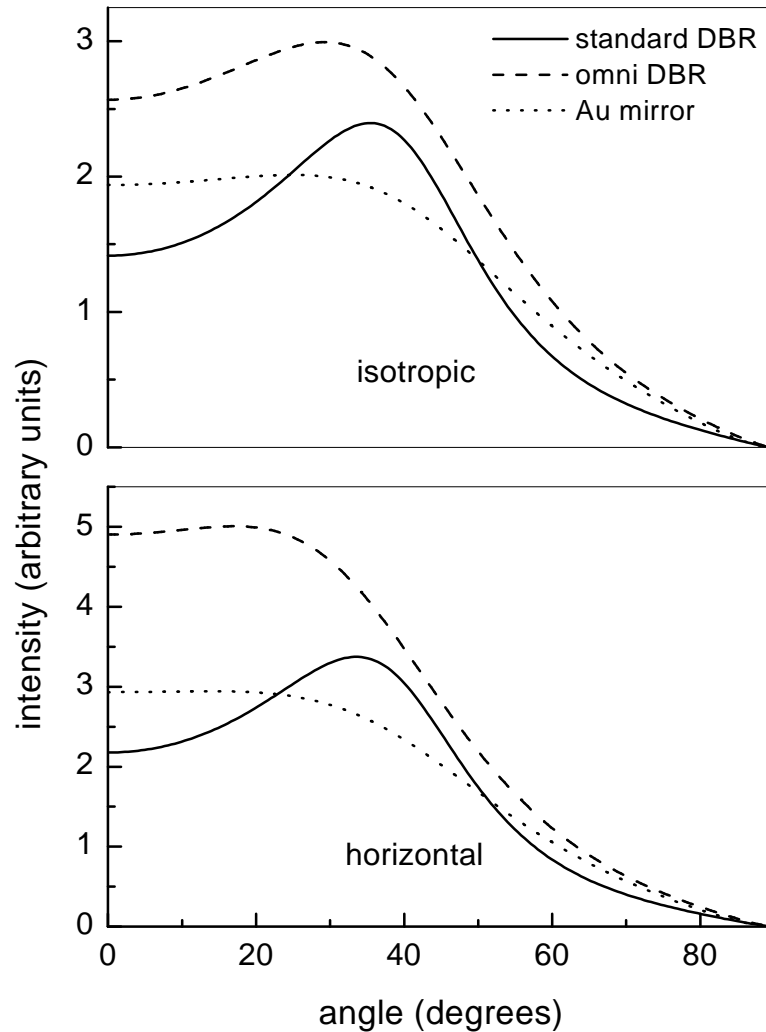


Figure 3.8 The angle dependent radiation pattern for the three types of top mirror, for both isotropic and purely horizontally oriented emitters. In each case the system is chosen to maximise the fraction of power radiated into the air. There were two layer-pairs in both the standard and omni-directional DBR, and the Au mirror was 20 nm thick. The emissive layer thickness for each system is given in figures 3.5, 3.6, and 3.7 respectively. The position of the emitter in the emissive layer is defined by b/d . For the isotropic emitters this value is 0.61,

0.68, and 0.44, for the horizontal emitters it is 0.46, 0.6, and 0.39, for the standard and omni-directional DBR and Au mirror respectively.

In figure 3.8, the energy per unit of solid angle has been plotted for each of the three different types of top mirror and the two types of emitter. The system modelled in each case corresponds to the top mirror configuration, the emissive layer thickness, and the emitter position, that produces the largest fraction of power radiated into the air (these parameters are easily found from the results in figures 3.5, 3.6, and 3.7). These radiation patterns give a relative indication of the amount of power being radiated, and in what direction it is propagating within the air. These plots clearly indicate the greater effectiveness of emitters having horizontally oriented dipole moments.

Modelling of the thick silica superstrates was achieved using a ray optics model and ignoring the interference effects of rays reflected within the thick layer [Bulovic (1998)]. The thick top layer of silica was included in the modelling as a likely feature of any fabricated device.

3.3 Discussion

Using a classical model, a number of different systems were modelled to compare the efficiencies of using standard Bragg reflectors, omni-directional Bragg reflectors and metal mirrors, in the construction of a cavity device, where the emissive layer has a high refractive index typical of polymer LED structures. This was done to determine the potential that each type of structure has from the view of a device application.

The importance of dipole orientation was highlighted as a significant factor in any emissive microcavity system, the horizontal emitters contributing the majority of power radiated into the far field. Consequently, it is important to properly account for the dipole orientation if an accurate determination of the efficiency of any particular device is to be obtained. The significance of the orientation of the emitters in a system was highlighted in an investigation of the $1/(2n^2)$ model, often used in evaluating the efficiency of a device. Where the distribution of emitters varies far from the isotropic distribution assumed in the model, we showed that the $1/(2n^2)$ model should be treated with care.

For each type of top mirror used in the cavity structure that was investigated the parameters for that mirror were explored. In the case of the DBRs the number of layers in the DBR was changed, and for the gold mirror it was the thickness of the gold that was varied. The thickness of the emissive layer was then optimised so that the largest fraction of power was radiated into the air. From the results obtained, the omni-directional DBR gave the best performance, then the standard DBR, and finally the gold mirror. For the horizontally oriented emitters, the optimised fraction of power radiated into the far field for those three structures was 57%, 47%, and 38% respectively.

We can offer some insight into the reasons for the different performance of these structures. The feature defining the most effective configuration for each of the different structures is the reflective qualities of the top mirror. In each case we can vary the amplitude of the reflected field by changing either the thickness of the gold layer or number of layers in the DBR. The omni-directional DBR out performs the standard DBR essentially because the cavity modes (most importantly the partially guided mode) are more effectively confined by the omni-directional DBR. The omni-directional DBR produces a phase shift in the reflected field that is greater than that produced by the standard DBR, which means that a cavity just large enough to support a single guided mode will be smaller when using the omni-directional DBR. The better the confinement of the partially guided mode, the more compressed the field profile will be in the cavity, corresponding to a higher field amplitude, and so the stronger an emitter will couple to it.

The gold mirror produces an even larger phase shift in the reflected field, resulting in a smaller optimum cavity thickness than either of the DBRs [Abram (1998)]. However, the gold mirror still performed relatively poorly because of the large absorption associated with it. In addition, the gold mirror has a SPP mode (see section 2.2) associated with it that provides an additional route by which energy may be lost from the emitter. The fields of an SPP mode decay exponentially with distance away from the interface. Power loss to the SPP mode associated with the Aluminium mirror affects all three structures. This can be seen in figures 3.5-7 as a reduction in the fraction of power radiated into the air as the position of the emitter is moved closer to the Aluminium (lower values of b/d). A similar quenching, but of much shorter range, is evident close to the

ITO for the DBR structures (high values of b/d in figures 3.5 and 3.6). This arises due to the intrinsic absorption we have assumed for the ITO ($\epsilon=3.5+0.05i$) [Persson and Persson (1980)]. The effect of the SPP mode associated with the gold mirror can be seen in figure 3.7.

3.4 Summary

It has been shown that microcavity devices may be used to improve the radiative efficiency of thin film emissive systems. We have also shown that the best performance that may be achieved for a particular device depends on the nature of the materials that one is able to use. If materials are available that allow for the construction of an omni-directional DBR, our modelling indicates this to be the best choice. If, however, a metal needs to be used, e.g. for simplicity, we have shown that a significant fraction of power may still be radiated into the far field by appropriate design of the microcavity. We have highlighted the importance of considering dipole orientation and position within the cavity in assessing device performance. The work of chapters 4 and 5 examines the effect of birefringence (known to exist in the polymeric materials being considered [Gymer (1993)]) and finite spectral width of the emission [Dodabalapur (1997)] on these results.

Chapter 4

Emission from birefringent polymer films

4.1 Introduction

Polymers are frequently used as the emissive material in optical devices such as the light emitting diode. The long chain molecular structure of typical polymer materials together with the spin coating technique by which thin layers are fabricated results in significant optical birefringence. In this chapter, an outline is given of a classical model for spontaneous emission from within such birefringent materials in planar multi-layer structures. We compare the results obtained using this model with experimental data on the radiation pattern produced by a thin film of the conjugated polymer poly[2-methoxy, 5-(2'-ethyl-hexyloxy) 1,4 phenylenevinylene] (MEH-PPV). As a control the radiation pattern from the dye Lumogen, dispersed as a guest in an optically isotropic thin film of polycarbonate, was measured. The effects of birefringence and the orientation of the dipole moment of the polymer are then investigated in order to understand the departure from the expected Lambertian radiation pattern that we observe from MEH-PPV. In addition, the model detailed in this chapter is used to consider the effects of birefringence on the dispersion of the non-radiative modes of a polymer waveguide.

Light emission from thin films is the basis of many optical devices, such as the LED. A significant amount of work has been done in modelling spontaneous emission from molecules embedded in such films [Chance et al. (1978), Lukosz (1980), Ford and Weber (1984), Benisty et al. (1998)]. The pattern of the emitted radiation is usually assumed to be Lambertian. Implicit in this assumption are two approximations, firstly that optical birefringence in the film can be ignored and secondly that the dipole moments that produce the emission have no preferred orientation in the film. However, for light emitting layers made of conjugated polymers, the usual method of fabrication makes use of spin coating. This results in the polymer chains lying predominantly in the plane of the film [McBranch et al. (1995), Becker et al. (1997)], with two

important consequences. Firstly, such films are anisotropic, the refractive index in the plane of the film and normal to the plane being different [Gymer et al. (1993), Boudrioua et al. (2000)]. Secondly, the dipole moments responsible for emission lie predominantly in the plane of the film [McBranch et al. (1995), Becker et al. (1997)]. The importance of conjugated polymers as a class of light emitting materials makes an assessment of the impact of birefringence and dipole orientation on their radiative performance highly relevant to attempts to better understand their properties and device efficiency.

Such an assessment has not been carried out before, primarily for two reasons. Firstly, light emitted by many planar conjugated polymer devices is dominated by radiation from the lowest order, TE-polarised, guided mode of the structure. It has thus been assumed that the polymer may be modelled as an isotropic material, using an appropriate choice for the polymer index [Greenham et al. (1994)]. Secondly, the theoretical modelling required to avoid the assumptions mentioned above is somewhat more involved, although the technique has been available in the literature for many years [Chance et al. (1978), Novotny (1997)] (see chapter 2).

As shown in this chapter, dipole orientation in particular can have a significant impact on the radiation produced by these devices (see also chapter 3). Furthermore, an understanding of these effects is shown to be even more important when recently developed techniques to improve device efficiency are employed. In such cases, light that would otherwise be lost as waveguided light in the structure is scattered out, either by random roughness [Windisch et al. (1999)], or periodically corrugated surfaces [Matterson (1999)] (see chapter 6). We shall see that a full understanding of birefringence and dispersion of the polymer films is required to fully account for the results of the experiments that are looked at in this chapter.

In this chapter, we present a model for spontaneous emission from within thin birefringent layers. The anisotropy of the materials used in typical polymer LED structures is thereby accounted for. This model allows us to examine in detail the effect of birefringence and dipole orientation on the radiative properties of thin polymer films. We do this by comparing results from experimental measurements with predictions based on the theory. Measurements are reported for the emission spectrum from a thin film of the

conjugated polymer MEH-PPV as a function of the emission angle. As a control the measured emission from a polycarbonate film doped with the dye Lumogen® is shown. This system displays no birefringence, and the dipole moments associated with the Lumogen take no preferred orientation in the film. The results of these measurements are also compared to our theoretical model.

In section 4.2 a theory is outlined for modelling planar multi-layer systems in which the materials may be birefringent, having different permittivities perpendicular and parallel to the interfaces of the layers. In section 4.3 the fabrication of the thin film samples, and how measurements of their radiation patterns were obtained, are discussed. The results of these measurements are reported. These results, and comparisons with theoretical modelling, are discussed in section 4.4. In section 4.5 modelling is used to show the effects of birefringence on the non-radiative (fully guided) modes of a cavity structure.

4.2 Theory

Treating the emitters as oscillating electric dipoles, we determine the \mathbf{E} and \mathbf{H} fields due to such sources. For an emitter in a thin layer, the fields reflected back to the emitter's site by the boundaries of the layer act to drive the emitter, resulting in a modification of the emission process (section 2.3). By determining the reflected \mathbf{E} field at the emitter's location, we calculate the effect of the environment (the multi-layer system) on the spontaneous emission rate of the emitter [Kuhn (1970)]. The emission into the far field of the system (i.e. radiation), using an approach similar to one reported elsewhere [Novotny (1997)], is also calculated. The model accounts for coupling to all guided and surface modes within the system. However, it does not account for subsequent re-excitation of any emitters as a result of the decay of another emitter (photon recycling effects [Benisty et al. (1998)]), which may be a feature of some devices.

Assuming an harmonic time component $\exp(-i\omega t)$ common to all field terms, Maxwell's equations for a non-magnetic, anisotropic material are,

$$\nabla \wedge \mathbf{E} = i\omega\mu_0\mathbf{H} \quad (4.1)$$

$$\nabla \wedge \mathbf{H} = -i\omega\epsilon_0 \underline{\mathbf{g}} \mathbf{E} \quad (4.2)$$

In a Cartesian co-ordinate system, we consider an electric dipole, oscillating with frequency ω , in a lossless material with dielectric permittivity tensor $\underline{\mathbf{g}}$, given by,

$$\underline{\mathbf{g}} = \begin{pmatrix} \epsilon_{//} & \mathbf{0} & \mathbf{0} \\ \mathbf{0} & \epsilon_{//} & \mathbf{0} \\ 0 & 0 & \epsilon_{\perp} \end{pmatrix} \quad (4.3)$$

The permittivity of the medium in the xy -plane is given by $\epsilon_{//}$, and in the z -direction by ϵ_{\perp} (see figure 4.1). In the next two sections we consider two orthogonal orientations of dipole moment, vertical (\perp) and horizontal ($//$) with respect to the plane of the layer. The fields due to dipoles of any other orientation can be found using some combination of these two.

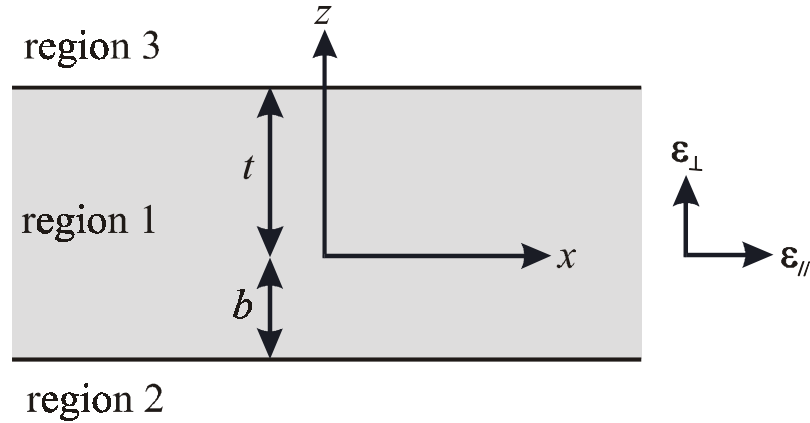


Figure 4.1 The cavity system. An emitter is located at the origin of the co-ordinate axis. Top and bottom interfaces are at $z=t$ and $z=-b$ respectively. The emissive layer thickness is given by $d=t+b$. The permittivity of any layer is described by a component perpendicular, ϵ_{\perp} , and parallel, $\epsilon_{//}$, to the layers in the system.

4.2.1 Vertical orientation of dipole moment

The fields of a dipole oriented parallel to the axis of the medium (the z -axis), following the method of Clemmow (1966), are given by,

$$\mathbf{H} = ik_0 \nabla \wedge \mathbf{\Pi} \quad (4.4)$$

where $\mathbf{\Pi}=(0,0,\Pi_z)$, is expanded in terms of plane waves, and,

$$\Pi_z = -\frac{i\omega p_0}{8\pi^2} \frac{\epsilon_{//}}{\epsilon_{\perp}} \iint \frac{1}{n_p} e^{ik_0(lx+my+n_p|z|)} dl dm \quad (4.5)$$

In this expression, p_0 is the amplitude of the dipole moment, and the variables l , m , and n_p are the normalised components of the wavevector [i.e. $\mathbf{k} = k_0(l, m, n_p)$] of a plane wave propagating in the medium, such that $H_z=0$ (i.e p -polarised), and are related by,

$$\frac{l^2}{\epsilon_{\perp}} + \frac{m^2}{\epsilon_{\perp}} + \frac{n_p^2}{\epsilon_{//}} = 1 \quad (4.6)$$

We change the integral of equation (4.5), using a simple substitution, so that the variables of integration are in terms of in-plane wavevector, u , such that $l=ucos\phi$ and $m=usin\phi$, to obtain,

$$\Pi_z = -\frac{i\omega p_0}{4\pi} \frac{\epsilon_{//}}{\epsilon_{\perp}} \int_0^{\infty} J_0(k_0 u \rho) \frac{u}{n_p} e^{ik_0 n_p |z|} du \quad (4.7)$$

We now introduce two interfaces, at $z=t$ and $z=-b$, so that the emitter is positioned within a cavity, see figure 4.1. Using the previous expression (4.7) as a source term within the cavity, and by then considering additional terms due to reflection and transmission at the interfaces, a general solution to the fields in the system can be constructed. The exact forms for the additional terms are found through application of the boundary conditions; namely the continuity of tangential \mathbf{E} and \mathbf{H} fields across the interfaces. The resulting expressions are,

$$\Pi_z = -\frac{\omega p_0}{4\pi} \frac{\epsilon_{//}}{\epsilon_{\perp}} \int_0^{\infty} X(u, z) J_0(k_0 u \rho) du \quad (4.8)$$

where,

$$X(u, z) = \begin{cases} i \frac{u}{n_{p1}} B_{\perp \rho \uparrow} e^{ik_0 n_{p3}(z-t)+ik_0 n_{p1}t} & z > t \\ i \frac{u}{n_{p1}} \left[e^{ik_0 n_{p1}|z|} + A_{\perp \rho \uparrow} e^{ik_0 n_{p1}(z+2b)} + A_{\perp \rho \downarrow} e^{-ik_0 n_{p1}(z-2t)} \right] & -b < z < t \\ i \frac{u}{n_{p1}} B_{\perp \rho \downarrow} e^{-ik_0 n_{p2}(z+b)+ik_0 n_{p1}b} & z < -b \end{cases} \quad (4.9)$$

and,

$$n_{\rho i} = \sqrt{\varepsilon_{i//} \left(1 - \frac{u^2}{\varepsilon_{i\perp}}\right)} \quad (4.10)$$

The terms A and B are given in appendix **B**, and J_i is the i th order Bessel function.

Using these expressions \mathbf{H} and \mathbf{E} can be determined, from equations (4.4) and (4.2), which allows us to perform a Poynting vector calculation [Novotny (1997)] (equation (2.50)) to determine the power radiated by an emitter in the absence of any interfaces, $b_{0\perp}$. We find,

$$b_{0\perp} = \frac{1}{q} \frac{\rho_0^2 \omega k_0^3}{12\pi\varepsilon_0} \sqrt{\varepsilon_{1//}} \quad (4.11)$$

where q is the quantum efficiency of the emitter and is included to account for non-radiative decay of the emitter (see section 2.3).

Using a method in which the value of the reflected field at the emitter's position is used to calculate any modification to the decay rate of the emitter (section 2.3), we obtain an expression for the normalised decay rate for the emitter in the cavity system,

$$\frac{b_{\perp}}{b_{0\perp}} = (1-q) + q \frac{3}{2} \frac{\varepsilon_{1//}^{\frac{1}{2}}}{\varepsilon_{1\perp}^2} \operatorname{Re} \int_0^{\infty} \frac{u^3}{n_{\rho 1}} \left(1 + A_{\perp\rho\uparrow} e^{2ik_0 n_{\rho 1} b} + A_{\perp\rho\downarrow} e^{2ik_0 n_{\rho 1} t}\right) du \quad (4.12)$$

In addition we use a Poynting vector calculation [Novotny (1997)] to find the power that is radiated into the far field of region 3 (see figure 4.1), where region 3 is non-dissipative (lossless), and obtain,

$$\frac{b_{3\perp}}{b_{0\perp}} = q \frac{3}{4} \frac{\varepsilon_{1//}^{\frac{3}{2}}}{\varepsilon_{3//} \varepsilon_{1\perp}^2} \int_0^{\sqrt{\varepsilon_{3\perp}}} u^3 n_{\rho 3} \left| \frac{B_{\perp\rho\uparrow}}{n_{\rho 1}} e^{ik_0 n_{\rho 1} t} \right|^2 du \quad (4.13)$$

4.2.2 Horizontal orientation of dipole moment

A similar analysis is now performed for a dipole that is oriented perpendicular to the optical axis of the emissive medium, and parallel to the interfaces we will later include. Again the method of Clemmow (1966) is used to construct expressions for the fields of an emitter which has its dipole moment directed along the x -axis.

There are two orthogonal plane wave solutions for a birefringent medium. With our choice of the z -axis as the optical axis of our system, the orthogonal solutions are characterised as having electromagnetic fields with either $H_z=0$ or $E_z=0$, and we refer to these fields as being p -polarised and s -polarised respectively. As we have seen above, the dipole oriented parallel to the optical axis only produces p -polarised fields. For a dipole oriented perpendicular to the optical axis we can expect both p - and s -polarised field terms. We construct our solution accordingly, and explicitly write the \mathbf{H} field in terms of the linear contribution from each polarisation,

$$\mathbf{H} = \mathbf{H}_s + \mathbf{H}_p \quad (4.14)$$

where, upon inspection of the resulting field terms, the term for \mathbf{H}_s can be reduced to,

$$\mathbf{H}_s = \nabla \wedge \nabla \wedge \mathbf{M} \quad (4.15)$$

and \mathbf{H}_p can be reduced to a familiar Hertz vector representation,

$$\mathbf{H}_p = ik_0 \nabla \wedge \mathbf{\Pi} \quad (4.16)$$

The vectors \mathbf{M} and $\mathbf{\Pi}$ are both directed along the z -axis ($\mathbf{M} = M \hat{\mathbf{z}}$, and $\mathbf{\Pi} = \Pi \hat{\mathbf{z}}$) and are given by,

$$\mathbf{M} = -\frac{i\omega\rho_0}{8\pi^2} \iint \frac{m}{n_s(l^2 + m^2)} e^{ik_0(lx + my + n_s|z|)} dl dm \quad (4.17)$$

$$\mathbf{\Pi} = \pm \frac{i\omega\rho_0}{8\pi^2} \iint \frac{l}{l^2 + m^2} e^{ik_0(lx + my + n_p|z|)} dl dm \quad (4.18)$$

where the \pm corresponds to values of z greater or less than zero respectively. The term n_p is defined above (equation (4.6)) and corresponds to plane wave solutions where $H_z=0$ (p -polarised), the term n_s corresponds to an orthogonal plane wave solution, which has $E_z=0$ (i.e s -polarised), and is given by,

$$l^2 + m^2 + n_s^2 = \epsilon_{//} \quad (4.19)$$

Making the same substitution used above, to change the variables of integration in expressions (4.17) and (4.18) to be in terms of in-plane wavevector, u , such that $l = u \cos\phi$ and $m = u \sin\phi$, we obtain,

$$\mathbf{M} = \sin\phi \frac{\omega\rho_0}{4\pi} \int_0^\infty J_1(k_0 u p) \frac{1}{n_s} e^{ik_0 n_s |z|} du \quad (4.20)$$

$$\Pi = \mp \cos \phi \frac{\omega \rho_0}{4\pi_0} \int_0^\infty J_1(k_0 u \rho) e^{ik_0 n_p |z|} du \quad (4.21)$$

As before, we introduce two interfaces, at $z=t$ and $-b$, see figure 4.1. The expressions, (4.20) and (4.21), are now used as a source term within the cavity, and we again consider additional terms due to reflection and transmission at the interfaces, to form a general solution for the fields in the system. The exact forms for the additional terms are found through application of the boundary conditions; namely the continuity of tangential \mathbf{E} and \mathbf{H} fields across the interfaces. The resulting expressions, for the dipole oriented parallel to the interfaces, are,

$$M = \sin \phi \frac{\omega \rho_0}{4\pi_0} \int Y(u, z) J_1(k_0 u \rho) du \quad (4.22)$$

$$\Pi = \cos \phi \frac{\omega \rho_0}{4\pi_0} \int Z(u, z) J_1(k_0 u \rho) du \quad (4.23)$$

where,

$$Y(u, z) = \begin{cases} \frac{1}{n_{s1}} B_{//s\uparrow} e^{ik_0 n_{s3}(z-t) + ik_0 n_{s1} t} & z > t \\ \frac{1}{n_{s1}} \left[e^{ik_0 n_{s1} |z|} + A_{//s\uparrow} e^{ik_0 n_{s1}(z+2b)} + A_{//s\downarrow} e^{-ik_0 n_{s1}(z-2t)} \right] & -b < z < t \\ \frac{1}{n_{s1}} B_{//s\downarrow} e^{-ik_0 n_{s2}(z+b) + ik_0 n_{s1} b} & z < -b \end{cases} \quad (4.24)$$

$$Z(u, z) = \begin{cases} -B_{//p\uparrow} e^{ik_0 n_{p3}(z-t) + ik_0 n_{p1} t} & z > t \\ \mp e^{ik_0 n_{p1} |z|} - A_{//p\uparrow} e^{ik_0 n_{p1}(z+2b)} + A_{//p\downarrow} e^{-ik_0 n_{p1}(z-2t)} & -b < z < t \\ B_{//p\downarrow} e^{-ik_0 n_{p2}(z+b) + ik_0 n_{p1} b} & z < -b \end{cases} \quad (4.25)$$

The n_{pi} are defined in equation (4.10), and the n_{si} are given by,

$$n_{si} = \sqrt{\varepsilon_{i//} - u^2} \quad (4.26)$$

and the terms A and B are given in appendix B.

We next perform a Poynting vector calculation, similar to that used for the dipole oriented along the z -axis. Expressions (4.22-25) determine the values of \mathbf{H} from equations (4.14-16). \mathbf{E} can in turn be determined from equation (4.2). With expressions for \mathbf{E} and \mathbf{H} we can construct a Poynting vector calculation [Novotny (1997)] (equation (2.50)) to determine the power radiated by an emitter oriented in the xy -plane, in the absence of any interfaces, $b_{0//}$. We find,

$$b_{0//} = \frac{1}{q} \frac{\rho_0^2 \omega k_0^3}{12\pi\epsilon_0} \sqrt{\epsilon_{1//}} \left(\frac{3\epsilon_{1//} + \epsilon_{1\perp}}{4\epsilon_{1//}} \right) \quad (4.27)$$

Equations (4.27) and (4.11) are clearly equivalent if an isotropic material is considered ($\epsilon_{1//} = \epsilon_{1\perp}$). It is now possible, as in the case of the vertical emitter, to calculate the effect of the cavity environment on the decay rate of the horizontal emitter. From section 2.3 we know that a calculation of the component of the reflected electric field in the direction of the dipole, at the dipole site, can be used to determine the modified decay rate (equation (2.34)). The normalised decay rate is found to be,

$$\begin{aligned} \frac{b_{//}}{b_{0//}} &= (1-q) + q \left(\frac{3\epsilon_{1//}^{\frac{1}{2}}}{3\epsilon_{1//} + \epsilon_{1\perp}} \right) \text{Re} \int_0^{\infty} \frac{u}{n_{s1}} \left(1 + A_{//s\uparrow} e^{2ik_0 n_{s1} b} + A_{//s\downarrow} e^{2ik_0 n_{s1} t} \right) du \\ &+ q \left(\frac{3\epsilon_{1//}^{\frac{1}{2}}}{3\epsilon_{1//} + \epsilon_{1\perp}} \right) \text{Re} \int_0^{\infty} u n_{p1} \left(1 + A_{//p\uparrow} e^{2ik_0 n_{p1} b} + A_{//p\downarrow} e^{2ik_0 n_{p1} t} \right) du \end{aligned} \quad (4.28)$$

By constructing the appropriate Poynting vector, it is also possible to calculate the power radiated into the far field [Novotny (1997)]. Assuming region 3 is non-dissipative, then the power radiated into that region is,

$$\begin{aligned} \frac{b_{3//}}{b_{0//}} &= \frac{q}{2} \left(\frac{3\epsilon_{1//}^{\frac{1}{2}}}{3\epsilon_{1//} + \epsilon_{1\perp}} \right) \int_0^{\sqrt{\epsilon_{3\perp}}} u n_{s3} \left| \frac{B_{//s\uparrow}}{n_{s1}} e^{ik_0 n_{s1} t} \right|^2 du \\ &+ \frac{q}{2} \left(\frac{3\epsilon_{1//}^{\frac{1}{2}}}{3\epsilon_{1//} + \epsilon_{1\perp}} \right) \frac{1}{\epsilon_{3//}} \int_0^{\sqrt{\epsilon_{3//}}} u n_{p3} \left| B_{//p\uparrow} e^{ik_0 n_{p1} t} \right|^2 du \end{aligned} \quad (4.29)$$

Equations (4.13) and (4.29) give the power radiated into the far field by vertically and horizontally oriented emitters respectively. These expressions are in terms of integrals over a variable u corresponding to the in-plane wavevector. Radiation patterns can therefore be derived from these expressions, since values of in-plane wavevector correspond to angles of propagation of emitted radiation [Lukosz (1981)]. In section 4.4 we look at the effect dipole orientation and film birefringence have on radiation patterns by comparing the results of our model to experimental data.

The emission from organic thin layers is, to first order, often assumed to be Lambertian. Such behaviour can be explained simply by considering how light propagating within the emissive layer is refracted as it leaves the film

[Greenham et al. (1994)] (a description is given in section 4.4). However, our more detailed analysis shows that the angular variation of emission can depend on the anisotropy of the refractive index, and on the orientation of emitters in the film.

4.3 Experiment

To investigate the effect of anisotropy on the emission profile experimental measurements have been performed on the angular variation of the emission from two types of emissive layers. The first type studied were thin films of the conjugated polymer MEH-PPV. These films were prepared by spin coating from chlorobenzene solution onto silica glass substrates. As discussed in section 4.1, the dipole moment of these films is known to lie predominantly in the plane of the spun film, with no preferred direction in the plane [McBranch et al. (1995), Becker et al. (1997)]. We refer to this system as one comprising horizontal emitters. The second type of film studied were polycarbonate films doped with Lumogen Red (LR) dye molecules, also prepared by spin coating on glass substrates from tetrachloroethane solution. Again, as discussed in section 4.1, we expect the individual dipole moments to be randomly oriented and refer to this system as one comprising randomly oriented emitters.

The resulting samples were excited by the 488nm line from an argon ion laser, with a power of approximately 1mW. The prepared films had an optical density, at 488nm, of less than 0.1, so that the excitation profile within the emissive layer can be considered uniform in the direction perpendicular to the film surface. The back of the substrate was covered by black absorbent paint, in order to eliminate scattering and reflection from this surface. The photoluminescence spectra from the films were recorded at various angles of emission from the samples, by collecting light with a fibre optic cable connected to a CCD spectrometer. The samples were kept under vacuum in a cylindrical glass chamber, to avoid photo-oxidation of the polymer during the experiment. The design of the chamber allowed the end of the fibre cable, of 1mm diameter, to be rotated around the excitation spot with an accuracy of 1° . While the excitation laser beam had a certain degree of polarisation, the photoluminescence signal from both MEH-PPV and LR films recorded at normal

viewing angle was found to be un-polarised, which suggests that the excitation was equally distributed between differently oriented emitters.

The polymer system that we considered comprised a ~30nm thick layer of MEH-PPV that had been spin coated onto a silica substrate ($\epsilon=2.12$). The resulting emission from the polymer was then detected at fixed angles with respect to the normal of the sample and the emission spectrum recorded. Figure 4.2 shows the emission spectrum that was detected for a range of different emission angles. To obtain a radiation pattern, we plot the emitted intensity at a wavelength of 680nm as a function of emission angle, figure 4.3. This pattern was found to be independent of emission wavelength.

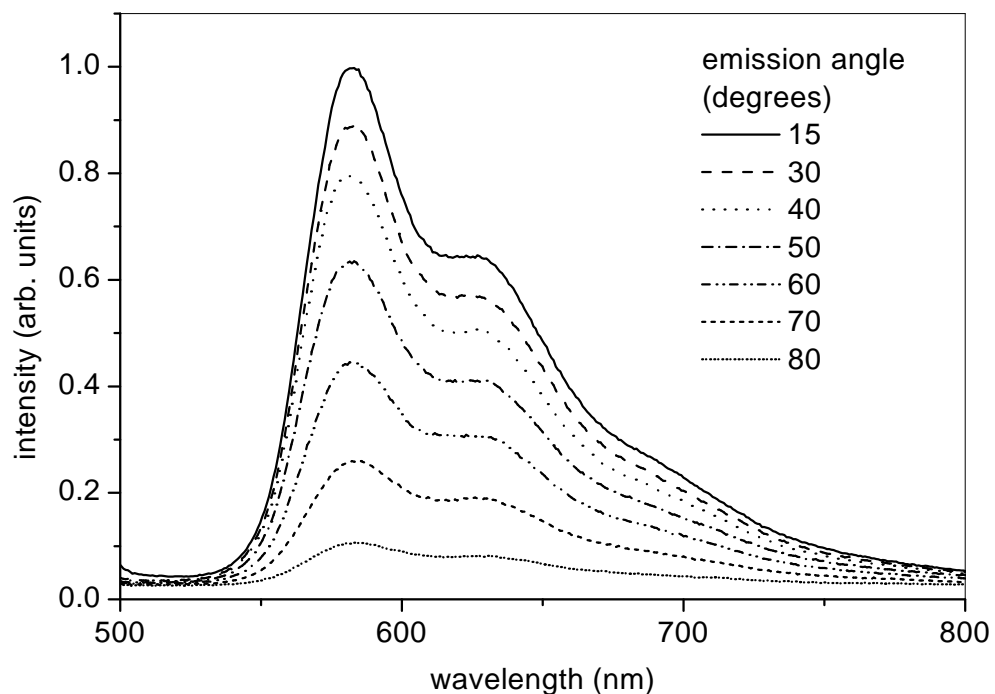


Figure 4.2 The photoluminescence spectra from a ~30nm thick MEH-PPV film on a black-backed silica substrate. Measurements were taken at several different angles with respect to the sample normal.

A similar experiment was also performed, where the emissive layer was a ~125nm thick layer of Lumogen dye doped polycarbonate, and the substrate was a section of microscope slide ($\epsilon=2.31$), the back of which had been painted black. Unlike MEH-PPV, the dye molecules are not expected to align in any

particular direction. Consequently, the emission from the film should appear to be due to an ensemble of randomly oriented emitters. The experimentally determined radiation pattern, for a wavelength of 650nm, is also shown in figure 4.3, and is noticeably different from the pattern produced by the conjugated polymer.

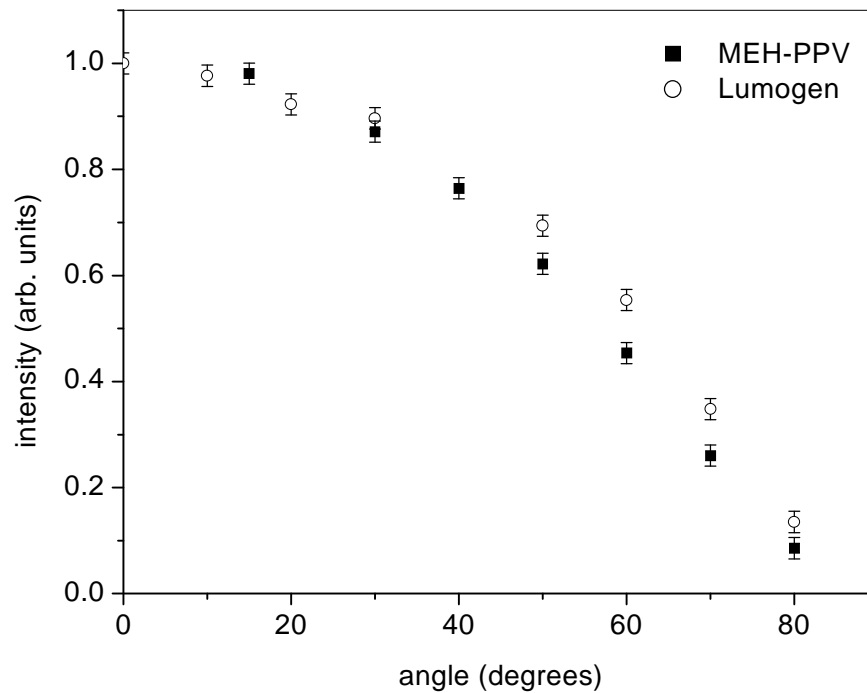


Figure 4.3 The experimentally determined emitted intensity as a function of emission angle for the MEH-PPV sample (at 680nm), and the Lumogen dye doped polycarbonate sample (at 650nm).

4.4 Discussion

The first issue to consider is how these experimental results compare with the Lambertian radiation pattern. This can be seen in figure 4.4(a) where we plot the experimentally determined radiation pattern from the MEH-PPV film at 680nm. For comparison we show a Lambertian distribution, which assumes a uniform emission associated with a randomly oriented emitter, and a modified Lambertian function.

The Lambertian distribution can be obtained by considering a 2-dimensional system wherein an element of energy, dE , is radiated by a source

into a direction θ_n within the emissive layer (of refractive index n), which is given by $dE=I_n(\theta_n)d\theta_n$, where $I_n(\theta_n)$ is the energy distribution (in the emissive layer) per unit of angle θ_n . By considering how this radiation is refracted (assuming all the energy is transmitted) through a planar interface into a region of air, we can equate this element of energy to the energy distribution (in the air) per unit of angle θ , $I(\theta)$, according to $dE=I(\theta)d\theta$, where θ is the angle of propagation in the air region. This gives the form of the energy distribution in the air that results from a source in the emissive layer as $I(\theta)=I_n(\theta_n)d\theta_n/d\theta$. By using Snell's Law ($n\sin\theta_n = \sin\theta$) we can eliminate $d\theta$ and $d\theta_n$, and by noting that $I_n(\theta_n)$ is a constant for uniform emission, we obtain the normalised Lambertian function, describing isotropic initial emission in an isotropic medium,

$$Lam_{iso}(\theta) = \frac{I(\theta)}{I(0)} = \frac{n \cos \theta}{\sqrt{n^2 - \sin^2 \theta}} \quad (4.30)$$

The modified Lambertian assumes a form of emission associated with emitters oriented in the plane of the layer (horizontal emitters). This was achieved by simply using the functional form for $I_n(\theta_n)$ corresponding to emission from a random distribution of horizontal emitters instead of the uniform distribution that describes emission from isotropic emitters. The modified Lambertian that accounts for purely horizontally oriented emitters is,

$$Lam_{hor}(\theta) = \frac{n \cos \theta}{\sqrt{n^2 - \sin^2 \theta}} \left[1 - \frac{1}{2n^2} \sin^2 \theta \right] \quad (4.31)$$

In figure 4.4(a) we see that the modified Lambertian is a better fit to the data than the standard Lambertian, although neither agree that well.

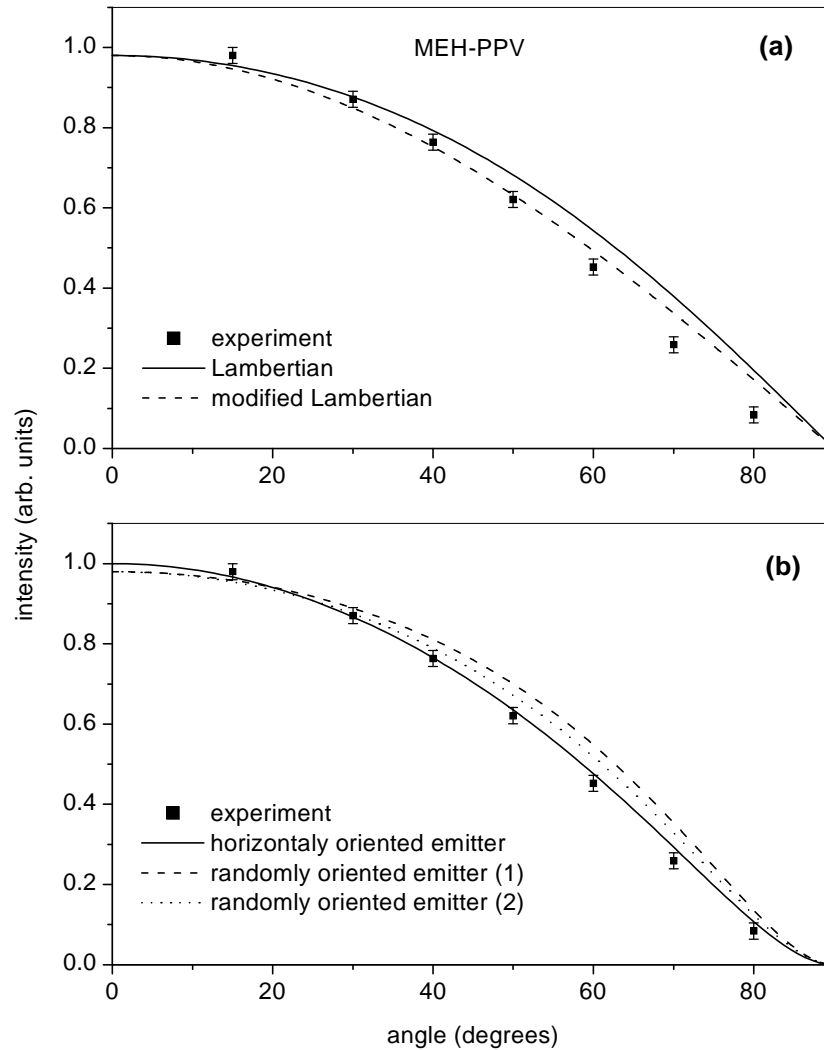


Figure 4.4 (a) The radiation pattern from the MEH-PPV sample at 680nm. This result is plotted along with a standard Lambertian distribution and a modified Lambertian distribution, the latter assumes the emission to be produced by dipoles oriented in the plane. **(b)** The same radiation pattern from the MEH-PPV sample as figure 4.4(a). Here we plot the results of our more comprehensive model, for horizontal emitters (this result has the same shape whether the emissive layer is birefringent or not), and for randomly oriented emitters when the emissive layer is (1) birefringent and (2) not birefringent.

In figure 4.4(b) we compare the experimental data with the results of our more complete model, as outlined in section 4.2. The cases of horizontally

oriented and randomly oriented emitters have both been considered. In each case the emissive layer has been treated both with birefringence ($n_{//}=1.8$, $n_{\perp}=1.6$ [Boudrioua (2000)]) and without ($n=1.8$). To model this system, it was assumed that the radiation pattern from an emitter located centrally within the emissive layer is similar to the pattern resulting from an emitter located anywhere else in the layer; calculations (not shown) for other emitter positions justified this assumption. The result of modelling this system for horizontal dipole moments agrees well with the experiment, and is independent of whether we treat the emissive layer with or without birefringence. For emitters with dipole moments oriented randomly the theory compares less favourably with experiment. In contrast to the case of the horizontal emitter just discussed, we now find that the randomly oriented system *is* affected by birefringence. This is because although birefringence does not significantly affect the shape of the radiation pattern for either a horizontally or vertically oriented emitter, it does affect the amplitude of the radiation pattern for each orientation differently. The shape of the radiation pattern due to dipole moments oriented randomly, which comprises contributions from both horizontal and vertical emitters, is therefore affected by birefringence. We thus see that we need to take account of the horizontal orientation of the dipole moment to successfully account for our results.

We return now to the case of the randomly oriented emitter. In figure 4.5 we again plot the radiation pattern from the Lumogen Red film, and also show a Lambertian distribution together with curves obtained using our model for both horizontal and randomly oriented emitters. The emissive layer is treated as an isotropic material with an index of $n=1.58$ (the index provided by the supplier for polycarbonate, which will not significantly be affected by the dye doping). To model this system, as with the conjugated polymer film, it is assumed that the radiation pattern from an emitter centrally located in the emissive layer is similar to the pattern resulting from an emitter located anywhere else in the layer. The result of modelling this system as a random distribution of dipole orientations gives very good agreement with the experiment, and is significantly better than the often assumed Lambertian [Greenham et al. (1994), Tsutsui and Yamamoto (1999)].

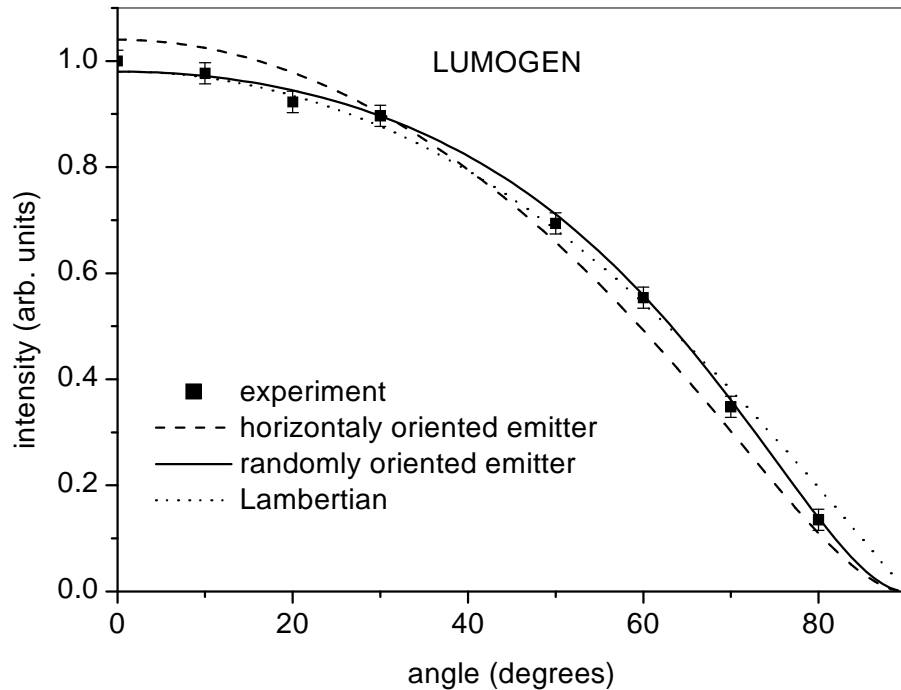


Figure 4.5 The radiation pattern from the Lumogen dye doped polycarbonate sample at 650nm. This result is plotted along with a standard Lambertian distribution, and the results of the model, for horizontal and randomly oriented emitters.

The experimental results shown above for emission from thin films of MEH-PPV and Lumogen dye doped polycarbonate, in conjunction with our model, clearly show up the effects of dipole orientation and birefringence. In particular, the results for modelling a thin film of MEH-PPV are in best agreement with experiment when the dipole moment associated with the emitters are considered to be oriented in the plane of the film. However, there is a negligible effect on this result, in terms of the shape of the radiation pattern we obtain, whether or not the birefringence of the film is taken into account. This insensitivity to birefringence is not surprising. Generally, it is only at larger angles of propagation (higher values of in-plane wavevector), usually beyond the critical angle for propagation in the air, that the effects of birefringence are significant. In general, the clearest effect of birefringence is upon the positions of TM-polarised modes that are either fully guided within birefringent films or

confined to nearby metal interfaces. These modes are not present in the systems we have looked at experimentally (the films were not thick enough to support waveguide modes and no metal was present). In addition, such modes would not be evident in a radiation pattern since they could not couple to light propagating in air without the use of some scattering mechanism.

4.5 Birefringence and mode dispersion

In this section, the effects of birefringence on the mode structure of a waveguide are highlighted. The validity of using an isotropic model to describe these polymer devices is investigated by comparing the results of modelling a simple anisotropic system with the results from modelling a comparable isotropic system.

With our model we can investigate the effects of anisotropy on an emitter. We now look at a single emissive layer bounded by air above and metal below (see figure 4.1 for example). This system is sufficient to consider the effects of anisotropy on the loss mechanisms typically available to an emitter; that is the coupling to far field radiation (in the air) and surface and fully guided modes. Any emission from within a high index region into air above corresponds to relatively small internal angles (within the high index layer). For such angles we expect the electric field of any wave propagating in the high index region to be more sensitive to the in-plane index of the high index emissive region. Therefore, it is the in-plane index of such a material that is generally used in making an isotropic approximation for high index uniaxial materials. As such, in the comparisons we make between anisotropic and isotropic materials in different structures, only the component of the permittivity of the emissive layer which lies perpendicular to the interfaces in the system (ϵ_{\perp}) is varied, and all other physical parameters are kept constant. This clearly results in the same phase relationships for s-polarised fields within both systems.

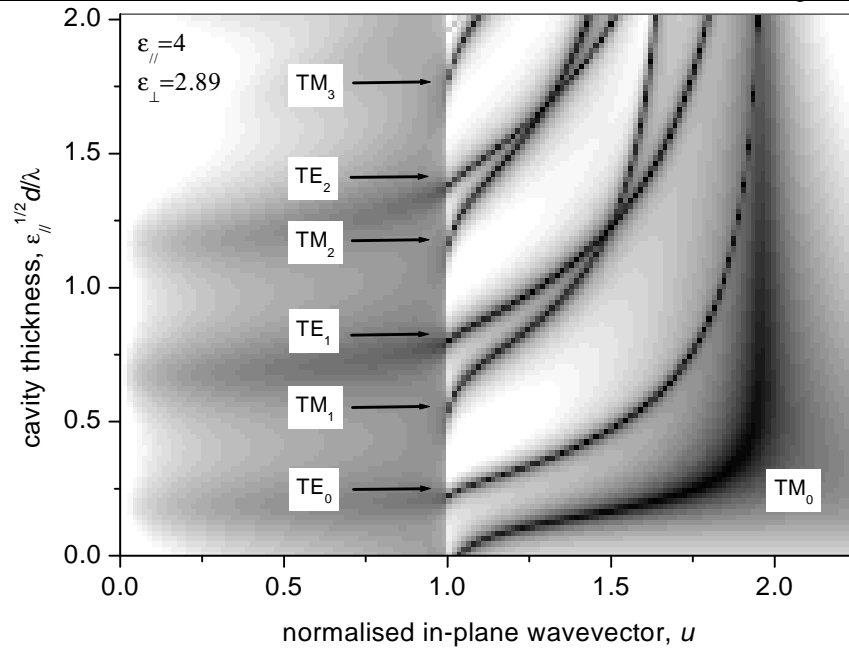


Figure 4.6 The dispersion of modes for a birefringent layer bound by regions of air and metal. The birefringent layer is described by $\epsilon_{||}=4$, $\epsilon_{\perp}=2.89$. The value $u=1$ corresponds to the magnitude of the wavevector in air.

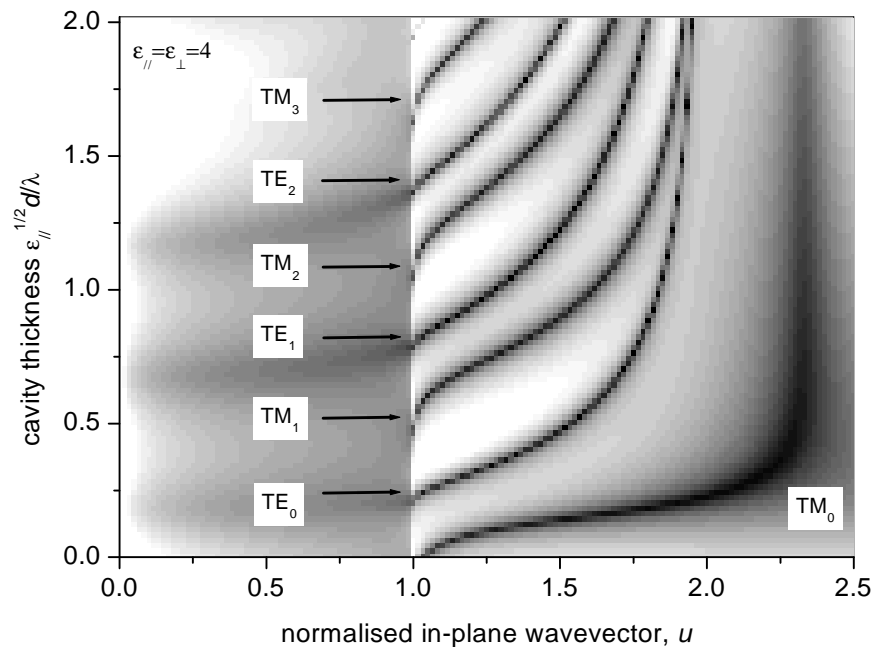


Figure 4.7 The dispersion of modes for an isotropic dielectric layer bound by regions of air and metal. The dielectric layer is described by $\epsilon=4$.

By considering the power lost, as a function of in-plane wavevector, by an isotropic emitter within a cavity structure, the modes for the cavity can be identified (as described previously in section 2.3.4). We plot the power lost by an emitter as a function of cavity thickness and in-plane wavevector (u), for an emissive layer bounded by semi-infinite regions of air ($\epsilon=1$) above and silver ($\epsilon=-15+1.5i$) below. In figure 4.6, the emissive layer is birefringent and described by $\epsilon_{//}=4$, $\epsilon_{\perp}=2.89$. We compare the results for the anisotropic layer with those for a comparable system with an isotropic emissive layer. In figure 4.7, the emissive layer is isotropic and described by $\epsilon=4$.

In comparing figures 4.6 and 4.7, we see that s -polarised modes are unaffected by changing ϵ_{\perp} , as expected, so the following discussion focuses on the effects of anisotropy on p -polarised modes. Mode position very near normal incidence ($u \approx 0$) is only affected by $\epsilon_{//}$, and so is independent of anisotropy. The range of in-plane wavevectors for which this holds true generally includes the region for which modes can propagate in the air. This means that the radiation pattern for each individual emitter orientation is largely unaffected by anisotropy, as was shown in section 4.4. Modes fully guided within the emissive layer are however significantly affected by ϵ_{\perp} , and the value of in-plane wavevectors for modes propagating within the layer has an upper limit of $u = \epsilon_{\perp}^{1/2}$. The higher the value of the in-plane wavevector for such a mode, the more of the perpendicular index it will experience, and so these modes are clearly affected by anisotropy. Surface modes bound at metal/dielectric interfaces are similarly affected by ϵ_{\perp} , where the position of such a mode, when each region is semi-infinite, is given by $u \rightarrow \epsilon_{\perp}^{1/2}$ as $\epsilon_{\text{metal}} \rightarrow -\infty$. The positions of p -polarised modes are clearly affected by anisotropy at higher values of in-plane wavevector, as expected.

4.6 Summary

We have established a suitable model for emission from thin birefringent films and successfully compared it with experimental data. This work has shown that we need to consider the orientation of the emissive dipole moments, and to a lesser extent the birefringence, when considering the radiation produced by thin conjugated polymer films. The method of spin coating the thin film of MEH-

PPV in the experimental samples appears to orient the polymer molecules predominantly in the plane of the film, in agreement with previous findings [McBranch et al. (1995)]. This accounts for both the birefringence of the layer and the in-plane orientation of the dipole moment (emitter orientation). For the thin film we investigated (~30nm) it was only the dipole orientation that needed to be accounted for to accurately model the measured results for emission from the MEH-PPV sample.

As noted in section 4.5, the effects of birefringence are notably more pronounced when fully guided and surface modes are present. This is the case in metal clad microcavities, an area that has been investigated experimentally at Exeter [Salt and Barnes (2000)], and is of importance in LED devices. Although the effects of birefringence have been considered in this chapter, the absorption that is also associated with the polymer materials that we are interested in has not so far been accounted for. Absorption in polymer films is a key issue that we address in the following chapter.

Chapter 5

Radiative efficiency of absorbing polymer films

5.1 Introduction

In this chapter we continue our investigation of the emission from thin planar films of light emitting conjugated polymers. Just as we have modelled emissive polymer layers in the preceding chapter, many workers do not include the absorption of the polymer in their modelling of emission from such films [Tessler (2000), Benisty et al. (1998)]. This may be an acceptable approximation for many systems, particularly where the absorption of the emissive layer is relatively low, but this is a simplification that is generally made because of the difficulties of including this absorption into a model. A new model for the radiative efficiency of the emission from a structure involving a polymer emissive layer is developed here. This specially developed model takes into account several factors including absorption in the emissive layer, a spread of emitter sites within the layer, and the broad emission spectrum associated with conjugated polymers. By calculating the efficiency of appropriate planar structures we can determine the scope for an increase in the efficiency of these systems, if energy lost to guided modes (energy that is confined to these structures) can be recouped.

The efficiency of radiative emission from LED structures, which are based on thin films of light emitting material [Dodabalapur et al. (1996), Friend et al. (1999), Samuel (2000)], is a key issue in device applications and is largely controlled by three factors; the efficiency with which excitons are generated [Shuai et al. (2000), Kim et al. (2000)], the efficiency with which excitons recombine to produce photons rather than non-radiative decay [Greenham et al. (1995)], and the efficiency with which the generated photons may escape the structure in which they are produced to yield useful radiation [Becker et al. (1997), Tessler (2000)]. Here we are interested principally in the last of these, i.e. the efficiency with which photons generated within the material emerge as useful radiation. Owing to the relatively high index of the majority of light

emitting materials, much of the energy emitted remains trapped in the emissive layer due to total internal reflection. A simple analysis based on ray optics (the $1/2n^2$ model described in chapter 4) for the case of a material of refractive index 2 shows that only $\sim 12.5\%$ of the energy is usefully radiated [Becker et al. (1997), Greenham et al. (1994), Benisty et al. (1998), Wasey et al. (2000)].

Various approaches have been adopted to overcome this limitation. One successful approach, which we have looked at in detail in chapter 3, is to place the thin film of emissive material between two mirrors so as to form a microcavity [Benisty et al. (1998)]. As we have seen in chapter 2, the boundary conditions imposed on the electromagnetic field by the microcavity limit the modes into which emission may take place. In general, microcavities possess two types of mode, leaky and fully guided (see section 2.2.2). Emission into a leaky mode of the microcavity structure produces useful radiation, though a fraction is lost to absorption. However, emission into fully guided modes cannot in general escape the microcavity and is thus absorbed by the microcavity materials. By restricting the number of fully-guided modes into which the emitters may lose their energy, the efficiency of radiation may be significantly increased, typically up to $\sim 50\%$ [Benisty et al. (1998), Wasey et al. (2000)], the remaining power being lost to absorption.

Several studies have sought to go beyond the simple planar microcavity in an attempt to increase the radiative efficiency still further. Their common theme has been to try and recover some of the power lost to fully guided modes. Schnitzer et al. (1993) achieved a radiative efficiency of 72 % by making use of photon recycling, an approach suited to materials with low waveguide losses. Tang et al. (1989) demonstrated that energy transfer from the electrically formed exciton to a dye molecule may also be used to improve efficiency. Several other investigations have revolved around the concept of scattering the guided light so as to convert it to from wasted guided modes to useful radiation. Gu et al. (1997) made use of emissive layers having angled side walls in an attempt to extract guided light macroscopically from the ends of the guide. Windisch et al. (1999) and Schnitzer et al. (1993) accomplished increased efficiency by using scattering from texture imposed on the superstrate, whilst Matterson et al. (1999) and Lupton et al. (2000) employed Bragg scattering from a periodically microstructured emissive layer.

What is the scope of these approaches of for increasing the radiative efficiency? This chapter concerns a study undertaken to address this question. We carried out a series of photoluminescence experiments to determine the different routes by which light leaves thin films of light emitting conjugated polymers, and to quantify the significance of each route. To understand our results we developed a theoretical model. Having verified our model against experimental data we were then able to quantify how much light remains trapped inside light emitting polymer films, and thus assess the extent to which the strategies mentioned above might be used to improve efficiency. We then turned our attention to electroluminescence, and discuss the efficiency of radiative emission from realistic light emitting diode structures. Finally we used our model to re-examine some controversial new results concerning the probability of singlet exciton formation undertaken by Kim et al. (2000). These authors undertook a fascinating study of electroluminescence from two LEDs based on conjugated polymers. Their experimental results, combined with their theoretical analysis, led them to a singlet exciton formation probability of 0.4 ± 0.05 , greater than the 0.25 expected from spin statistics [Shuai et al. (2000)]. Our re-analysis supports this high probability, though with several qualifications. We conclude this chapter by discussing the limitations of our model in predicting the performance of realistic light emitting diodes and indicate what further information is still required.

This chapter is structured as follows. Section 5.2 is concerned with the computational model we used, and the assumptions we made. In particular we discuss how we incorporated details of the spectral width of the emission from an excited molecule, and the spread of emitter locations throughout the emissive layer. The process by which we determine the intrinsic spectrum of emission from the conjugated polymer MEH-PPV is also described. We used this light emitting polymer for our study because it is a polymer whose optical properties have been characterised [Boudrioua et al. (2000)]. Furthermore, we describe the experimental approach we adopted to study the photoluminescence (PL) quantum yield of thin polymer films. The results of both our experiment and associated modelling are discussed in section 5.3. We then use our model to explore the extent to which trapped guided light limits the photoluminescence efficiency of light emitting polymer films, and discuss the

effects of accounting for the spectral width of emission upon these results, in section 5.4. In section 5.5 we extend our discussion to look at modelling electroluminescent devices and we examine the efficiency of radiative emission from such structures. In particular we use our model to reanalyse recent results on singlet exciton formation that rely for their interpretation on a good knowledge of radiative emission efficiency. In section 5.6 we summarise our results and discuss the limitations of present models, including our own, in predicting the performance of realistic light emitting diodes.

5.2 Modelling the emission

Our task here is to put together a model and verify it using experimental data so that we can simulate the radiative efficiency of light emitting conjugated polymer thin films. We wish to predict how much power is dissipated, and in what directions, by sources within the emissive polymer layer. Models suitable for use as a starting point are well developed [Chance et al. (1978), Tomas and Lenac (1997), Ford and Weber (1984), Barnes (1998)], and are based on treating the sources as driven, damped dipole-oscillators (see chapter 2). They are damped because they radiate and are driven by the fields that are reflected from the interfaces in the structure. Below we discuss how we extended one of the existing models to accommodate features pertinent to the polymer films of interest.

5.2.1 Assumptions made in the model

We made several important assumptions in constructing our model. These concern the birefringence and absorption of the conjugated polymer films and the orientation of the dipole moments responsible for the emission; these aspects are discussed below.

Dipole Orientation

Several previous works have shown that the orientation of the dipole moment associated with optical emission in spun films of conjugated polymers lies predominantly in the plane of the film, and this is verified in the results of

chapter 4. [Kim et al. (2000), Becker et al. (1997), Wasey et al. (2000), McBranch et al. (1995)]

Birefringence and Absorption

Conjugated polymers, such as MEH-PPV, provide a challenge as materials in which to model the emission of light since they are in general both birefringent *and* absorbing. It is not a priori clear to what extent these two factors are important in the present context. Ideally a suitable computational model would include both factors, since both the birefringence and the absorption have been experimentally determined [Boudrioua (2000)] and can be expected to have some effect. Previous authors have pursued the problem of emission in media that are both birefringent and absorbing. They found [Tomas and Lenac (1997), Barnett et al. (1996)] that it is not possible to fit both material properties into a coherent framework, owing to problems in dealing with the longitudinal field components. We have already indicated in chapter 4, that in computing the power radiated out of layers with optical properties characteristic of MEH-PPV, the birefringence has little effect [Wasey et al. (2000)]. Rather, the birefringence is important only if one wishes to determine the exact nature of the fully guided modes supported by the structure. In this chapter we are more concerned with the ratio of emitted power to the power that remains trapped. Consequently, in modelling thin layers of MEH-PPV, we chose to describe our emissive layer as isotropic and absorbing, this combination retaining the important physics in the present case, and having the merit of being amenable to computation. Absorption was included by making use of the complex in-plane refractive index of the material, as depicted in figure 5.1.

With these assumptions in place we followed the theory of Thomas and Lenac (1997) to model the cavity modification to the spontaneous emission rate of the excitons in the light emitting polymer. The theory of Tomas and Lenac (1997) is an extension of the classical model of the spontaneous emission of an emitter (as described in chapter 2) that accounts for the absorption of the emissive polymer layer. Essentially, the approach of Tomas and Lenac involves identifying the radiative decay rate of an emitter, which is achieved by removing the longitudinal (quasi-static) contribution to the overall decay rate that is calculated. It is assumed that any non-radiative contribution can be accounted

for by an appropriate choice of q , the quantum efficiency of the emitter [Chance et al. (1978)] (see section 2.3). For our experimental situation there were two key aspects that required us to further extend this driven, damped dipole oscillator model. Firstly, we need to include the broadband nature of the source, taking account of the emission spectrum. Secondly, we also need to take account of the distribution of emitters through the samples (assumed to be uniform) in conjunction with the spatial profile with which they are excited.

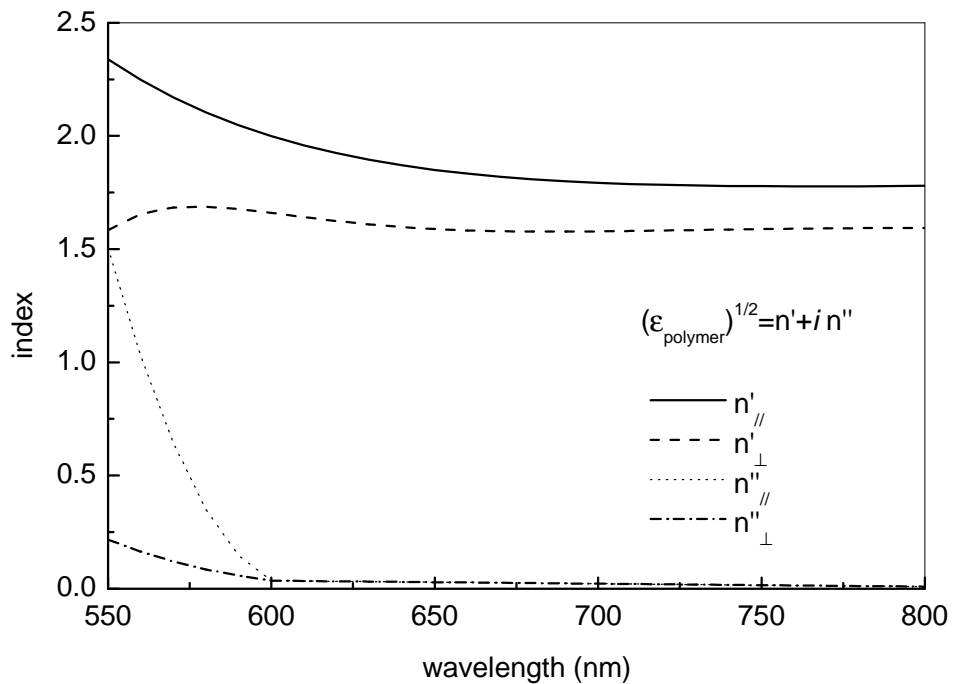


Figure 5.1 A functional representation of the complex refractive index for a spun film of MEH-PPV. The in-plane ($//$) and normal (\perp) values are both shown. The dispersion of the complex birefringent indices we used was determined using angle dependent reflectivity techniques [Boudrioua et al. (2000)]. The data were interpolated using polynomial fits to provide the required information for the modelling used here.

5.2.2 Spectral width

To account for the broad range of the MEH-PPV emission spectrum we model this broadband emitter by means of what we refer to as a composite emitter. The details of including the emission spectrum specific to MEH-PPV are

deferred to section 5.2.4. Here we simply introduce the concepts and assumptions needed to model a broadband rather than a narrowband spectrum. We present expressions for the total power dissipated in free space by a composite emitter, P_{tot} , the total power dissipated by such an emitter in a cavity environment, P'_{tot} , and the power such an emitter radiates into the far field from within a cavity environment, P_{rad} . The composite emitter comprises an appropriately weighted sum of single emitters, the i^{th} emitter having a free space emission wavelength of λ_i . In free space we define the total power dissipated by the composite emitter as,

$$P_{tot} = \sum_i Power_i(\lambda_i) \quad (5.1)$$

where $Power_i$ denotes the contribution to the total power dissipated by the i^{th} emitter (with free space wavelength λ_i), and effectively defines the intrinsic emission spectrum of the composite emitter.

Since each individual molecule has a broad emission spectrum, due to spread in both the excited energy levels of the molecule and the lower energy levels to which the molecule may then radiatively decay, we expect there to be an intrinsic (unperturbed) probability distribution for the wavelengths at which the molecule may radiatively decay (in free space). Such a probability distribution for the wavelength of emission allows us to define an intrinsic emission spectrum in terms of the power contributed to the emission (in free space) by each wavelength, equation (5.1). Furthermore, by noting that different transitions give rise to emission at different wavelengths, we expect that emission at one wavelength will not affect the emissive rate at other wavelengths (this also means that modification to the emissive rate at one wavelength does not affect the emissive rate at other wavelengths). Our model thus assumes the emission to be homogeneously broadened. We further assumed the emission spectrum could be represented by emitters equally spaced in wavelength, such that $(\lambda_{i+1} - \lambda_i) = \Delta\lambda_i$ is a constant for all i . The function $Power_i$ thus corresponds to some continuous function, $Power(\lambda)$, the continuous intrinsic emission spectrum. Placing the composite emitter in a cavity environment will result in a modified total dissipated power, P'_{tot} , which can be written as,

$$P'_{tot} = \sum_i c_i Power_i(\lambda_i) \quad (5.2)$$

where c_i represents the modification to the contribution from the emitter with free space wavelength λ_i induced by the local environment. From equation (5.2), we see that if the local optical environment modifies the emission at a single wavelength we may expect the emissive rate for the composite emitter to be altered. The values c_i can be found using our model for calculating the modification to the power dissipated by a single emitter when it is placed in a cavity environment (non-absorbing case) from chapter 4 [Wasey et al. (2000)]. The coefficient c_i is thus the power dissipated by the i^{th} emitter in the cavity, divided by the power dissipated by that emitter in free space. We can also construct an expression for the amount of power radiated out of the cavity by the composite emitter, P_{rad} , given by,

$$P_{rad} = \sum_i f_i Power_i(\lambda_i) \quad (5.3)$$

where f_i is the amount of power radiated out of the cavity by the i^{th} emitter, divided by the power dissipated by that emitter in free space.

We now have expressions for the total power dissipated and for the power radiated out of the cavity for just one, composite emitter in a cavity, equations (5.2) and (5.3) respectively. We now need to account for the spread of emitter positions through the emissive layer, where each position in the layer may have a different effect on the properties of an emitter placed there.

5.2.3 Excitation profile

To model the distribution of the excited emitters in the polymer layer we made several further assumptions. We assumed that the effects of the laser used to excite the emissive layer in the experiment are such that the laser intensity is well below that required to saturate the layer. We can then assume that the power available to emitters at a particular position in the emissive layer remains constant in time and corresponds to the total power dissipated by all the emitters at that position. We further assume that the decay of an excited emitter cannot result in the excitation of another emitter (i.e. no photon recycling effects [Schnitzer et al. (1993)]).

We can now define some function, $p(x)$, corresponding to the excitation profile in the layer, where x describes the position within the emissive layer, normal to the interface planes. We expect $p(x)$ to take an approximately exponential form where we have a laser directed at one side of the layer to provide the excitation, as in the PL experiments detailed here. To account for the continuous excitation profile we divide the emissive layer into a number of equal thickness sub-layers. We consider a single composite emitter located at the mid-point of each sub-layer. The position of the j^{th} emitter is given by x_j . We define the total power dissipated by a composite emitter at x_j as $p(x_j)$. As such, it should be clear that the total laser power dissipated by the emissive layer is given by $\sum p(x_j)$. For convenience we normalise $p(x)$ such that $\sum p(x_j)=1$. Making use of equations 5.2 and 5.3, we may also obtain an expression for the power radiated out of the cavity by the composite emitter at x_j , $R_j(x_j)$, given by,

$$R_j(x_j) = p(x_j) \left[\frac{\sum_i f_i \text{Power}_i(\lambda_i)}{\sum_k c_k \text{Power}_k(\lambda_k)} \right] \quad (5.4)$$

Summing over emitter sites, the total power radiated out of the emissive layer is given by $\sum R_j(x_j)$. Through our normalisation of $p(x)$, the value of $\sum R_j(x_j)$ corresponds to the fraction of power absorbed from the laser by the emissive layer that results in radiation out of the cavity.

5.2.4 Intrinsic emission spectrum of MEH-PPV

Before we can use equation 5.4 to model our polymer layers, we need to determine values for Power_i , which correspond to the intrinsic spectrum of the emissive species in question, i.e. the MEH-PPV emission spectrum. This may be done by measuring the spectrum of the radiation from a thin sample, for some fixed angle with respect to the sample normal. This layer must be sufficiently thin that the variations across the thickness of the emissive layer resulting from cavity effects are not important. This then enables us to use a single emitter, centrally located to adequately model the effects of the layer. Let us define the measured intensity distribution, $\text{Rad}(\theta, \lambda)$, from such a system, for radiation at some fixed polar angle, θ , by,

$$Rad(\theta, \lambda) \propto \frac{F(\theta, \lambda)}{P(\lambda) \sin(\theta)} Power(\lambda) \quad (5.5)$$

where $F(\theta, \lambda)$ is the power radiated per unit of solid angle from the sample by a single emitter in the structure, corresponding to a free space wavelength λ , $P(\lambda)$ is the total power dissipated by that single emitter, and $Power(\lambda)$ is the continuous form of $Power_i(\lambda_i)$ (i.e. the weighting that represents the intrinsic emission spectrum). Since both $F(\theta, \lambda)$ and $P(\lambda)$ can be calculated with our model, and $Rad(\theta, \lambda)$ can be measured experimentally, the form of $Power(\lambda)$ can be determined. By choosing an appropriate range in wavelength where the polymer is seen to emit (~500-800nm), and dividing this range into a number of equally spaced intervals, $Power_i(\lambda_i)$ can be determined.

The structure used to obtain the measurements by which the intrinsic spectrum was calculated comprised a ~30nm thick layer of MEH-PPV on a silica substrate (the system examined in section 4.3). The back of the substrate was painted with black absorbing paint to eliminate any scattering from the back face. A measurement for the spectrum of the emitted radiation from the sample was taken at an angle of 15 degrees to the sample normal and is shown in figure 5.2(a), the sample was excited by an Argon ion laser operating at 488nm. The term corresponding to the modification of the internal spectrum due to the cavity ($F(\theta, \lambda)/P(\lambda)$) is also shown, figure 5.2(b), and the resulting intrinsic spectrum ($Power(\lambda)$) that is determined using equation 5.5, is shown in figure 5.2(c).

In calculating $F(\theta, \lambda)$ the emissive layer was treated as birefringent and absorbing, since as noted in section 5.2.1, the radiative field components from a dipole source in such a medium *can* be modelled, even though the non-radiative components cannot. The dipole moment of the emitters was taken to be randomly oriented in the plane of the film [Wasey et al. (2000), McBranch et al. (1995)] (see chapter 4). Values for the intrinsic spectrum were determined every 10nm between 550 and 800nm to define $Power_i(\lambda_i)$. Looking at figure 5.2, the major difference between the intrinsic and measured radiation spectra is that the intrinsic spectrum is biased towards shorter wavelengths due to the increased absorption in this spectral region.

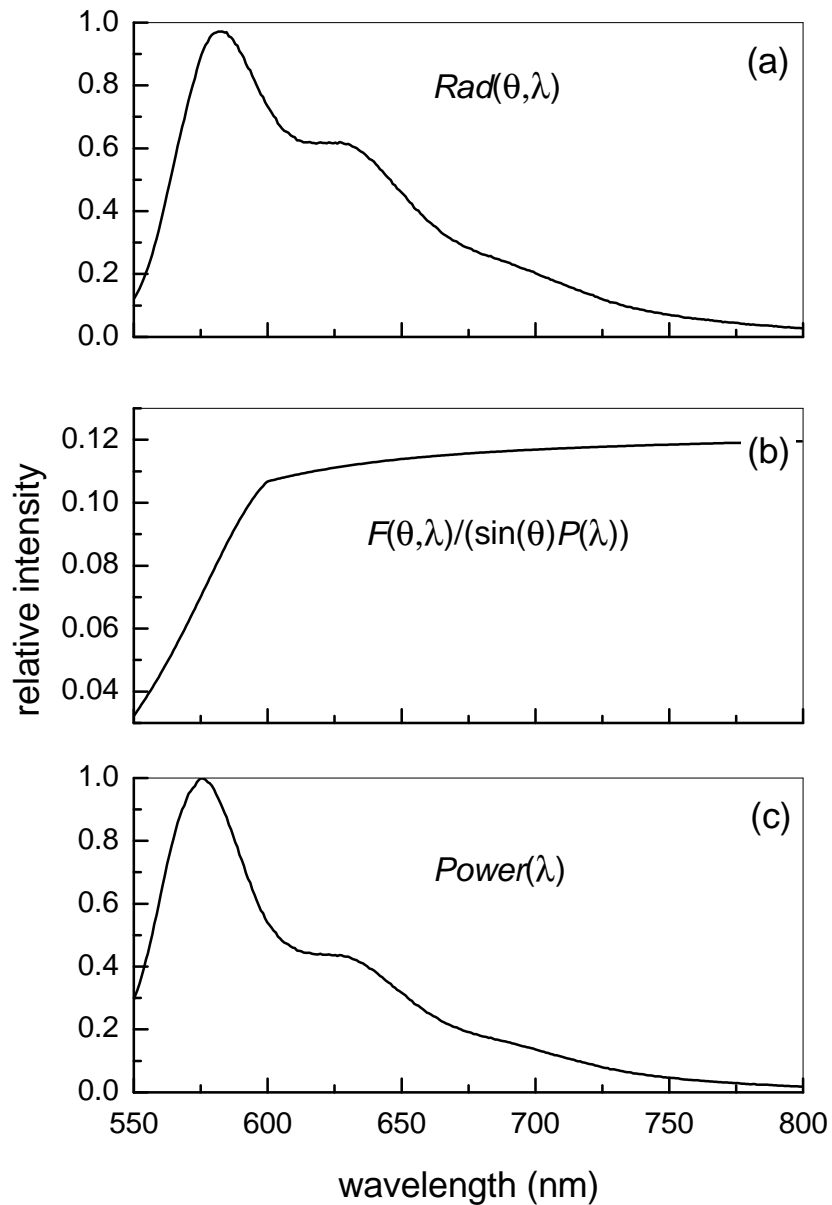


Figure 5.2 The steps of the calculation of the intrinsic emission spectrum of the polymer MEH-PPV. (a) The measured emission spectrum, at 15° , for a thin MEH-PPV film. (b) The calculated modification to the polymer's intrinsic spectrum. (c) The deduced intrinsic spectrum for MEH-PPV.

5.2.5 Emission pathways: experimental details

In this section we determine quantitatively the effectiveness of the different pathways by which light leaves the polymer films. We did this by

comparing the results of measurements with the predictions of the model already outlined in this chapter.

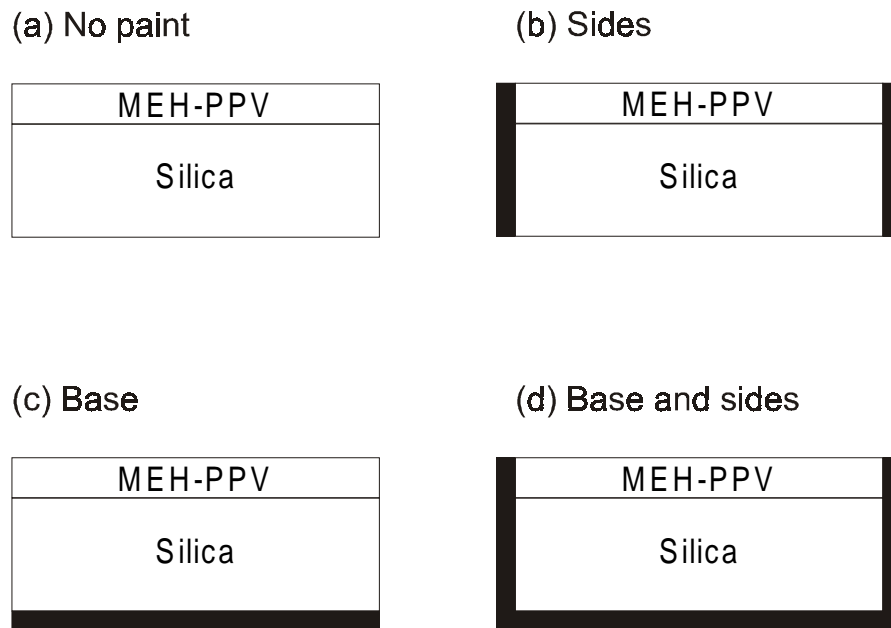


Figure 5.3 A schematic of the four types of sample used to examine the different emissive pathways, and the way in which they were coated with black paint.

Thin films ($80\pm 5\text{nm}$ thick) of the polymer MEH-PPV were deposited by spin coating onto silica glass substrates, 7mm square and 1mm thick. The polymer was excited using the 488nm line of an Argon ion laser at normal incidence to the sample. The beam covered an area 1mm wide and was positioned in the centre of the sample. In general, light generated in the emissive layer can escape through the back and front faces, and also through the sides of the sample. The experiment involved collection of the emitted radiation in an integrating sphere when the sample was (a) as made (bare), (b) painted black on the sides, (c) painted black on the back, and (d) painted black on the back and edges, see figure 5.3. The black paint used was an excellent absorber of light so that this strategy enabled us to identify the different directions into which the power was radiated, so providing a means of verifying the model we used. We measured the radiative emission with an integration sphere using techniques we have described in chapter 4 [Greenham et al. (1995)]. Briefly, the absorbed pump power was determined by comparing the

pump throughput of the sphere for the sample being measured with that of a blank substrate. A fibre coupled CCD spectrometer was then used to determine the emitted power.

Our results were as follows. We took the power emitted from the unpainted sample, sample (a), to be the reference level, assigning it the value 1. From the sample with black edges (b) we measured a power of 0.45-0.5, from the sample with black back (c) 0.2-0.3, and from the sample with both back and edges black (d) 0.17-0.25. These results are discussed in the following section.

5.3 Discussion

Using the model outlined earlier in this chapter we computed the power radiated from the different structures (the different painting strategies) as a function of emitter position within a polymer film 80nm thick. In the experiment, some of the light initially radiated towards the silica/air interface is reflected within the sample, and emerges instead through the sides. The model described previously assumes each interface to be infinite, and as such does not account for emission through the sides. We therefore accounted for light that emerges through the sides of the samples as follows:

- All light initially radiated directly towards the sides of the silica was assumed to emerge as radiation.
- Light that 'bounced' in order to get to the edge was accounted for, provided it encountered the polymer/silica interface no more than once. If it was reflected by this interface more than once it was assumed to have been absorbed. For the sample geometry used, light bouncing more often than this was in any case totally internally reflected at the side, rather than being partially transmitted.

In this geometry and for the indices of materials used, only ~1% of emission is both totally internally reflected from both the back face and totally internally reflected from the edges of the silica; we have not therefore included results for this small contribution to the emission process. The square shape of the sample, and the reflections from the sample sides for light guided in the

silica, were not accounted for since we estimated this would make a relatively small change. In terms of modelling the sample with black paint covering certain regions, any contribution to the total power impinging on a painted surface was assumed to be absorbed. The results, normalised with respect to those of the bare sample are shown in figure 5.4. From these data it is easy to compute the average value of the power radiated from the structures, averaged over all emitter locations, weighted to take account of the excitation profile. For the samples (b), (c) and (d) we find values of 0.45, 0.28 and 0.19 respectively.

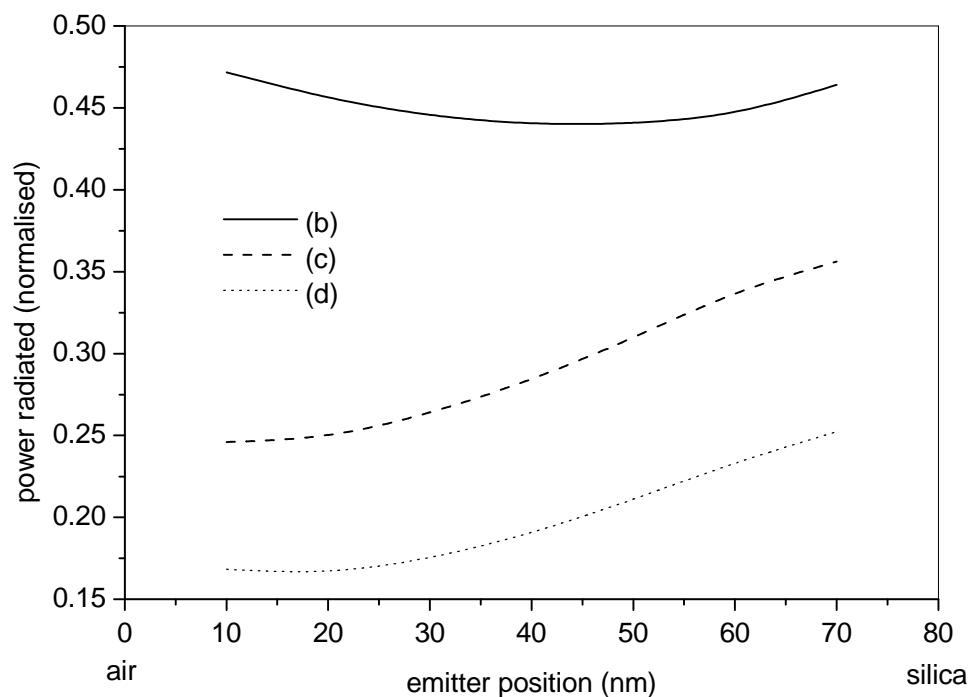


Figure 5.4 The calculated radiative efficiency of a single composite emitter, based on the intrinsic spectrum for MEH-PPV, for the different sample configurations shown in figure 5.3, as a function of emitter location within the polymer layer.

These data are compared with the experimental values in table 5.1 where we see that there is good agreement between experiment and theory. The model agrees well with the efficiency results obtained experimentally, and gives us confidence in using our model to investigate emission from such polymer layers. In the following sections we use the model we have developed

to explore the extent to which the efficiency from light emitting layers may be improved, and to consider the importance of including the spectral and spatial spread of emission in our model. Two types of system can be examined, photoluminescent structures and electroluminescent structures. Both are of practical interest, the former in such applications as single photon sources and the latter for light emitting diodes.

Sample	Emitted power (Experiment)	Emitted power (Theory)
(a) bare sample	1	1
(b) black edge	0.45-0.55	0.45
(c) black back	0.2-0.3	0.28
(d) black edge and back	0.17-0.25	0.19

Table 5.1 The power emitted by the different samples, normalised to the power emitted by the bare sample, i.e. the sample with no black paint. The range given for samples (b) - (d) is an indication of the measurement error in each case. Also shown are the results of the theoretical model.

5.4 Predictions of the model for photoluminescence (PL)

The model we have established enables us to make some predictions about the amount of power initially dissipated by sources in the polymer that does not escape from the polymer layer, instead being absorbed. Since we have assumed no photon recycling, the values we present must be considered as an upper limit on the power absorbed by the film. Similarly, the values we give for the power radiated out of the polymer film must correspond to a lower limit.

In figure 5.5, we plot the power directly emitted from the polymer layer into the silica substrate, P_{silica} , and the power emitted directly into the air, P_{air} . Since these results are normalised to the pump laser power absorbed in the film, the power absorbed in the polymer (P_{abs}) is given by $P_{abs} = 1 - P_{silica} - P_{air}$. In figure 5.5(a) we show the result of our model where we have included the intrinsic spectrum of the emitter (figure 5.2(c)) and an exponential form for the excitation profile through the polymer layer, decaying away from the polymer/air interface. For comparison, in figure 5.5(b) we plot the result of our model for a single emitter with a free space emission wavelength of 590nm that is at a fixed distance of 20nm from the polymer/air interface. For both systems the emitters are localised near the polymer/air interface and as such the value for P_{silica} will tend to zero as the polymer layer is continuously increased in thickness. This is seen in the general decrease in P_{silica} for an increase in polymer thickness, and is because any emission into the silica must first travel through an increasingly larger absorbing polymer region. Looking at figure 5.5(b) the periodic oscillations in power with thickness are expected and arise as new waveguide modes are introduced into the system. In comparison, figure 5.5(a) shows less evidence of these periodic oscillations, since they are further damped by the spectral width of the emission in this case. In comparing figure 5.5(a) and (b) it is clear that for the particular experimental geometry considered a good choice of a single emission wavelength and single emitter position, can make a good approximation for a broadband emitter, since the variation in results is seen to be ~10%.

We now focus on the results of the composite emitter model, figure 5.5(a). We can see that the model predicts a significant increase in the power absorbed by the film, from ~40% to ~75%, as the film thickness is increased from 40 to 120nm. This increase is due to the emergence of the first guided mode. This mode is initially a radiative (leaky) mode in the air and silica. As the thickness increases further, the mode becomes more confined to the polymer layer as it ceases to be radiative in the air. Finally, for sufficiently thick films the mode becomes totally guided in the polymer layer. By becoming more localised in the polymer, the mode is more effectively absorbed. Above a film thickness of 120nm, the absorbed power remains relatively constant, with a trend to slowly increase with polymer thickness, as explained above. The lack of features as

the thickness increases further, even though new modes become available, arises from a combination of the broad spectral width of the emission and the absorption of the polymer.

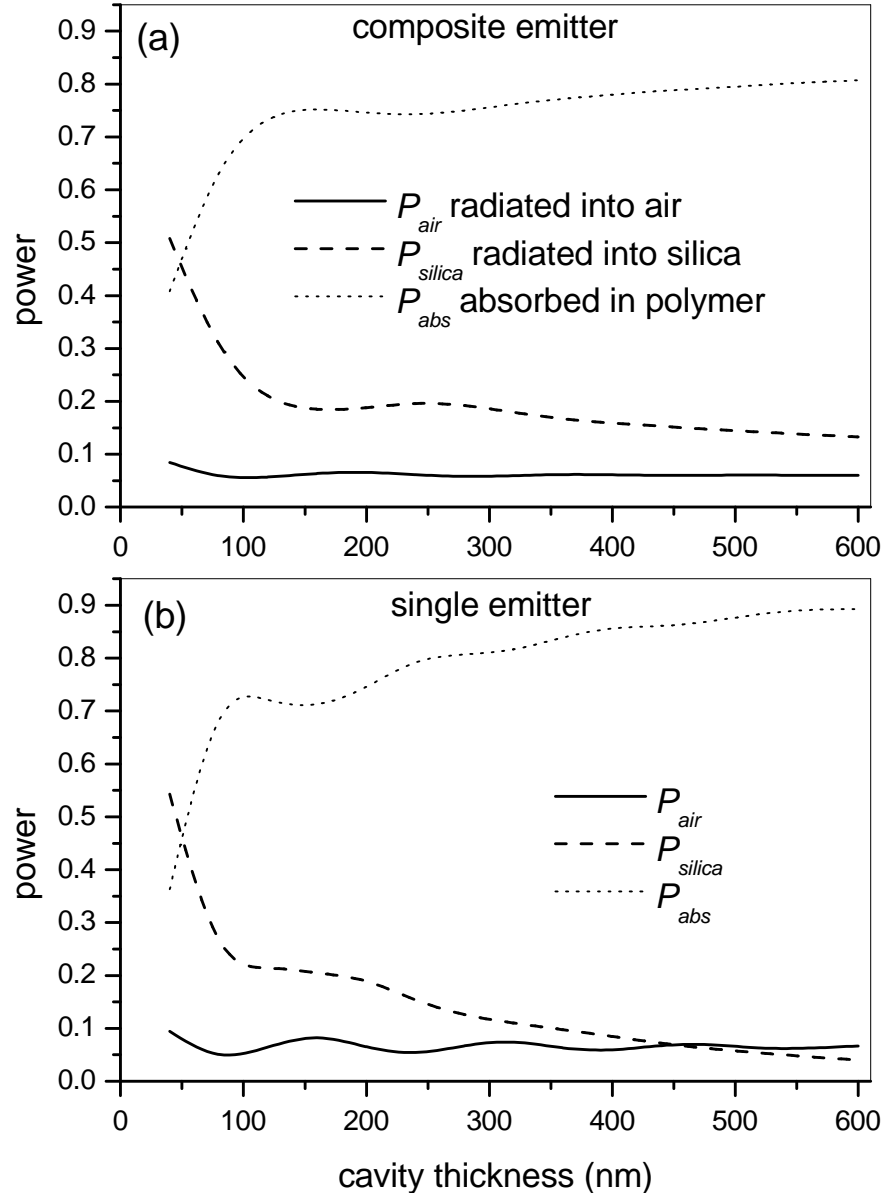


Figure 5.5 The calculated efficiency of the emission from the photo-excited air/MEH-PPV/silica system. (a) A spread of composite emitters with an exponential excitation profile that decays away from the polymer/air interface. (b) A single emitter with a free space emission wavelength of 590nm at a fixed position of 20nm from the polymer/air interface.

The model indicates that a significant proportion of power may be confined to the polymer, $\sim 75\%$, for any film thickness above 100nm. This is power that could be recovered through use of scattering mechanisms, such as gratings [Matterson et al. (1999), Lupton et al. (2000)] or surface roughness [Windisch et al. (1999), Schnitzer et al. (1993)]. An alternative strategy would be to inhibit the modes to which power is lost, perhaps through the use of photonic band gaps formed by using periodic texturing at the polymer interfaces [Salt et al. (2000)].

5.5 Using the model to explore electroluminescence (EL)

In this section we apply our model to a calculation of both the efficiency with which radiative singlet excitons may be produced by electrical injection, and the efficiency with which such excitons may produce useful radiation in an EL device. By working with the results of Kim et al. (2000), we use our model to find a value for the number of singlet excitons that are excited per electron flowing in the external circuit of their device and compare our result with theirs.

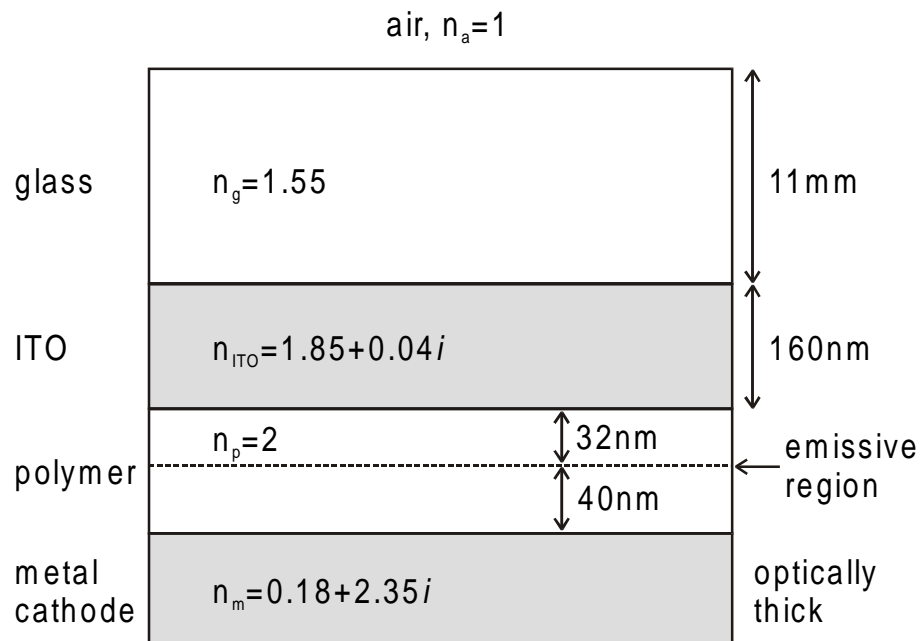


Figure 5.6 Schematic of the green emitting LED structure of Kim et al., which includes the optical parameters used in our modelling.

We consider the green emitting LED of Kim et al. The structure of the LED is identified as a glass substrate covered by a 160nm thick indium-tin oxide (ITO) layer upon which a 72nm thick emitting polymer layer is formed. The polymer was then coated with metal to form the top cathode. In an EL device the electron-hole recombination often occurs within a reasonably well defined layer within the polymer. This recombination layer is the region in the polymer where excitons are formed and from which emission may subsequently occur. As such, the problem of identifying an excitation profile (section 5.2.3) is simplified for an EL device, if a single position can be associated with all of the emission. Kim et al. identify the recombination zone in their green LED to be 40nm from the cathode. We use this value, as well as all the information they provide relating to the refractive indices of the materials of the LED, to model emission from their device. The structure and parameters used in our modelling are shown in figure 5.6, which is a schematic of the LED. Furthermore, we are restricted to considering emission for the single free space wavelength of 550nm, just as they used in their optical modelling, since we have no information on the intrinsic emission spectrum. This does however mean that our results can be compared directly to those of Kim et al.; as noted in section 5.4, this single wavelength approximation may be a good one, though it is not clear this is the case for this EL system.

We start with an expression, related to equations (8) and (11) of Kim et al., for the external EL quantum yield η_{el}^{ext} . This is the ratio of the number of photons radiated out through the diode surface to the number of electrons flowing in the external circuit, and was measured experimentally by Kim et al. for their green LED to be 6% \pm 0.5% (see table 1 of Kim et al.). The external quantum yield can be written as

$$\eta_{el}^{ext} = \gamma r_{st} \alpha \quad (5.6)$$

where γ is the probability that an electron flowing in the external circuit produces an exciton, r_{st} is the probability that the exciton so formed is a singlet, as opposed to a triplet (in general, singlets decay radiatively and triplets non-radiatively), and α is the probability of a singlet exciton decaying to produce a photon that is emitted from the diode surface. The probability α is equivalent to

the fraction of the total power that is lost by a radiative emitter that is subsequently emitted through the surface of the device.

Thus far we have not discussed the quantum efficiency, q , of the emission. This is the probability that a singlet exciton decays radiatively, rather than being directly lost to the polymer through, for example, the excitation of local phonon modes. In considering our photoluminescence results of section 5.4 we did not discuss the effects of the quantum efficiency. This was justified since there we were only concerned with how the emitted radiation was distributed among the various emission pathways, which is not a result significantly affected by q . However, in considering electroluminescence we need to take specific account of the quantum efficiency. The factor α in equation (5.6) depends on the quantum efficiency in two ways. Firstly, the higher the value of q the greater the EL efficiency will be since a greater proportion of singlet excitons may decay radiatively. Secondly, a high value of q means that the cavity has a greater influence over how effectively radiative emission competes with non-radiative emission. Non-radiative decay is unaffected by the cavity, thus, if the cavity is able to enhance the radiative decay rate, non-radiative decay will become less significant.

We model the singlet exciton as a dipole emitter with a dipole moment oriented in the plane of the polymer layer. Treating the emissive layer as isotropic and loss-less with a refractive index of 2, in the fashion of Kim et al., we obtain values for the power emitted from the face of the diode and total power lost by the emitter as 0.292 and 2.87 respectively (these quantities are scaled to the total power radiated by an emitter in an unbounded region of polymer), thus giving α as 0.1. Here we have assumed that $q = 1$, the effect of changing q is discussed next.

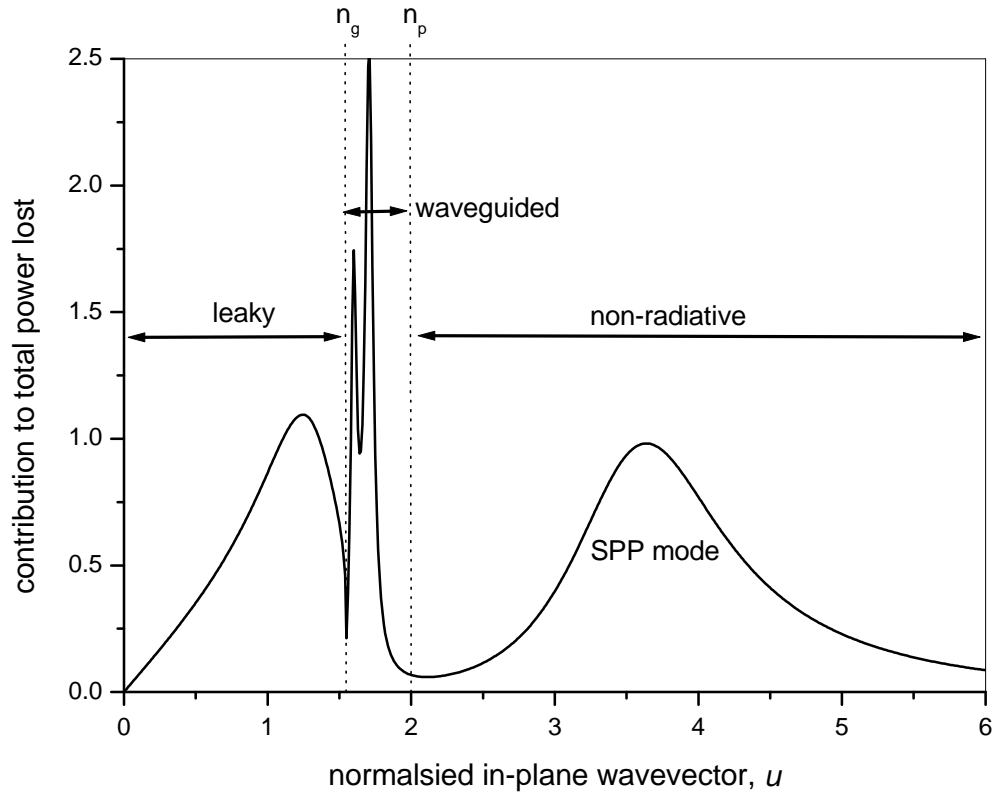


Figure 5.7 Contributions to the total power lost by an emitter as a function of the normalised in-plane wavevector u (normalised by the magnitude of the wavevector in free space $k_0=2\pi/\lambda$, where $\lambda=550\text{nm}$). The emitter is a horizontally oriented electric dipole located in the LED structure (as depicted in figure 5.6). Power components with a normalised in-plane wavevector $u < n_g$ may radiate into the silica (and/or air if $u \leq 1$), those with $n_g < u < n_p$ are confined to the polymer and ITO layers, and those with $u > n_p$ are non-radiative (dominated in this regime by coupling to the SPP mode).

The contribution to the total power lost by the emitter as a function of the normalised in-plane wavevector, u , is shown in figure 5.7. The strong features in the figure correspond to coupling between the emitter and modes of the structure. The area under the whole curve gives the total power lost by the emitter. The area under that part of the curve associated with a particular mode is a measure of the power lost through coupling to that mode. That a significant amount of power is lost by the emitter to the waveguide and surface (SPP)

modes of the structure is evident from the figure. The strength of these modes means that they have a significant effect upon the decay of the emitter and must therefore be properly accounted for to describe the behaviour of the emitter, an aspect assumed to be unimportant by Kim et al.

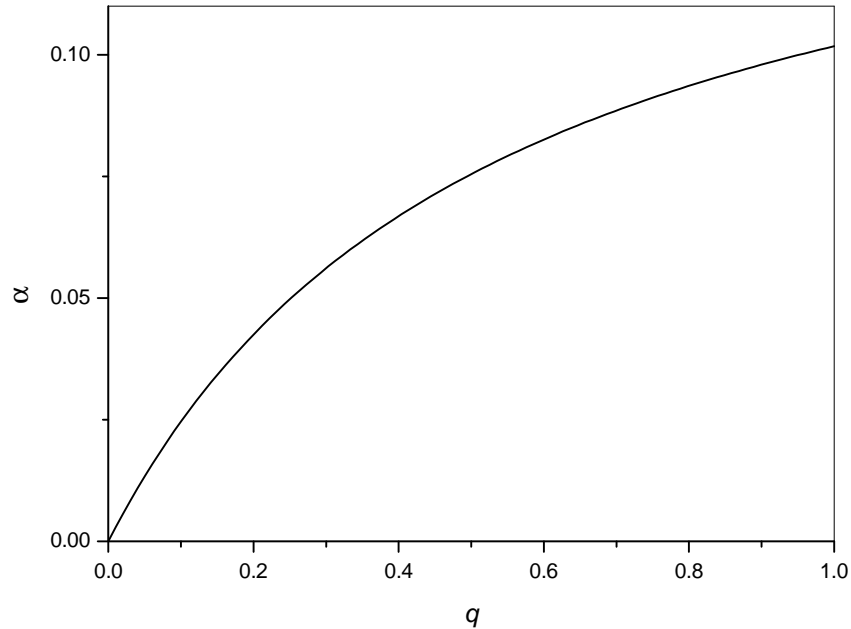


Figure 5.8 The probability of a singlet exciton decaying to produce a photon that is emitted from the diode surface, α , is shown as a function of the quantum efficiency, q , of the emitter.

We now consider the effect of the quantum efficiency, q . In figure 5.8 we show how α depends on q by calculating the power emitted from the face of the diode and total power lost by the emitter for different values of q . As expected, the value of $q = 1$ gives the maximum value for α (10%), and as q is decreased we see that α decreases. Since Kim et al. have measured $\eta_{\text{el}}^{\text{ext}}$ for their green LED as ~6%, we can now use equation (5.6) to obtain an estimate for the product γr_{st} , which corresponds to the ratio of singlet excitons formed to electrons in the external circuit. Kim et al. found this product to be 40%, a result that is surprisingly high when compared to the 25% expected from simple spin statistics. However, as noted by Kim et al. their ‘half-space’ model does not take full account of the guided modes of the LED structure. Our model specifically

takes account of these modes (as shown in figure 5.7) and so it is interesting to see what our model will predict for the product γ_{st} . Using the value of $q = 0.33$ quoted by Kim et al. (something they refer to as the free-space photoluminescent yield) we find α to be 6% so that the resulting value for γ_{st} is 100%. This remarkably high value depends critically on the value used for q in the calculation. In the limit of $q = 1$ ($\alpha = 10\%$) we obtain a lower limit for γ_{st} of 60%. Thus the probability that an electron flowing in the external circuit produces a singlet exciton (γ_{st}) would appear to lie between 60% and 100%. Our result supports the findings of Kim et al. that γ_{st} is greater than the 25% expected from spin statistics, a matter discussed in the following section.

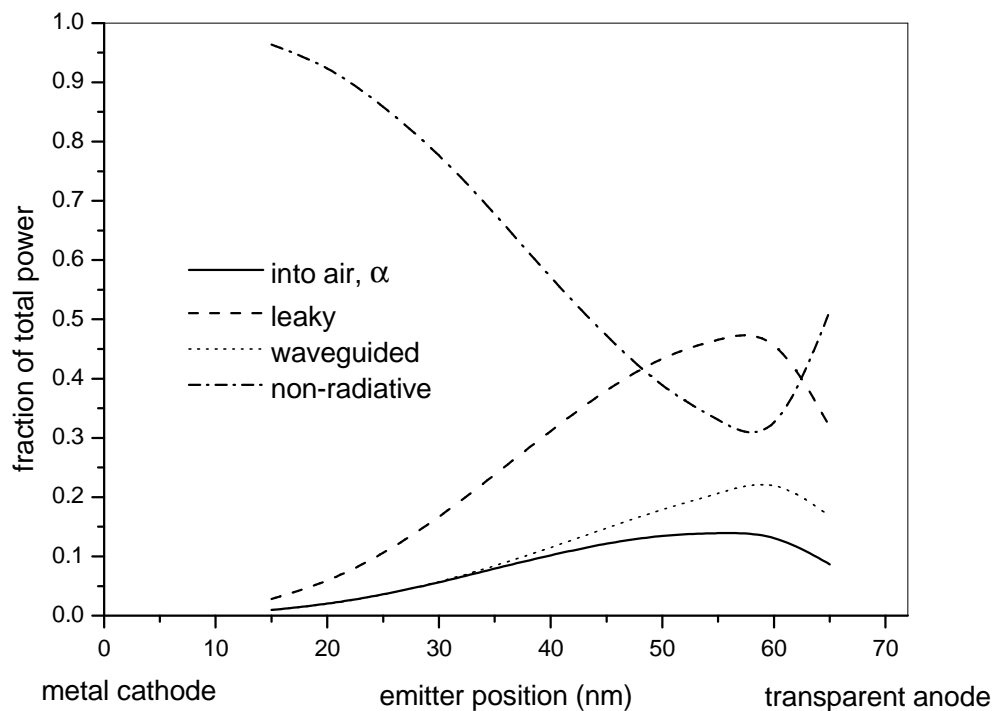


Figure 5.9 The variation of α and the contributions to the total power lost by a singlet exciton, as a function of emitter position in the polymer layer for $q=1$.

It is worth noting that the modelling we have undertaken here, though it takes account of guided modes, still has limitations. One limitation is a lack of information concerning the spatial distribution of the emitters. In figure 5.9 we

show the change in the value for α , and the different contributions to the decay of singlet states, as a function of emitter position in the polymer layer. The strong variation of α with emitter position indicates that accounting for a spread of emitter positions, corresponding to a potentially broad recombination zone [Tessler (2000)], may be necessary to properly model the EL device structure.

The absorption of the polymer layer is another factor absent from our study of this EL device. However, further modelling, for the single emission wavelength and for the single emitter position (as given by Kim et al.), but with a polymer index of $n_p=2+0.1i$ (an arbitrary choice), yielded values for the power emitted from the face of the diode and total power lost by the emitter of 0.218 and 2.29 respectively. The associated value for α is then $(0.218/2.29)=\sim 9.5\%$, which is not very different to the 10% result obtained for the non-absorbing polymer case, and indicates that accounting for absorption does not appear to significantly affect our present result. However, without knowing accurately the complex index of the polymer, the result may still depend on the value of absorption for the polymer used in the model. We note that a complete account of all pertinent details has yet to be made in any realistic modelling of an EL device. To do this one needs not only a comprehensive model (as outlined in this chapter), but also accurate information on all relevant parameters, especially the complex refractive index of all materials and their dispersion.

5.6 Summary

We have presented a model for the radiative emission of sources embedded within a thin polymer film. This model accounts for the broad spectral width of the emission from light emitting polymers and also accounts for an excitation profile that may be necessary to describe the emissive region of the polymer.

By analysing the emission measured from a very thin MEH-PPV layer with our model, the intrinsic spectrum for this polymer was calculated, account being taken of self absorption. Incorporating this intrinsic spectrum into our model allowed us to examine where the emission from an experimental sample, comprising a polymer film on a silica substrate, is directed (either radiated from

the top, bottom or sides of the sample). Having found good agreement between the experiment and our model, we proceeded to make some predictions about the power that is lost to absorption in the polymer for a simple photo-excited MEH-PPV film on a silica slide, as a function of film thickness. Our model showed that for such MEH-PPV films of sufficient thickness (>100nm) approximately 75% of radiative emission never escapes the emissive layer, and is lost to absorption in the polymer. This represents a significant proportion of power that, if recovered, would produce a large increase in efficiency.

Finally, we looked at the results of Kim et al. for an EL green emitting polymer LED that they had fabricated. Using our model, and relying on the parameters that Kim et al. provided for their system, we found the maximum radiative efficiency of the device (α) to be ~10%. We then went on to estimate the number of singlet excitons formed per electron flowing in the external circuit as lying between 60% and 100%. This result is very high compared to the 25% expected from simple spin statistics, it is also significantly greater than the value of ~40% that Kim et al. calculated for their structure. Our higher value results primarily from the fact that our model indicates a significant amount of power is lost to guided modes, an aspect not fully dealt with by Kim et al. However, as we have noted in the preceding section, our model also has limitations and these can only be overcome by a more thorough knowledge of the system. Though both our analysis and that of Kim et al. are limited, it does seem as though the value of γ_{st} is greater than the 25% value predicted by simple spin statistics. Our results thus lend support to the theoretical work of Shuai et al. (2000), where they calculate a higher value using a molecular orbital perturbation approach.

For both EL and PL systems there is clear scope for a considerable improvement in efficiency, if recovery of wasted, guided light were to be successfully implemented. In the following chapter, we investigate a possible method for recovering such wasted light as we look at the effects of introducing periodic corrugation to emissive polymer systems.

Chapter 6

Effects of corrugation on polymer emission

6.1 Introduction

In this chapter we analyse measurements of photoluminescence from corrugated thin films of a light-emitting polymer. We find that various non-radiative optical modes guided by the structure Bragg scatter off the corrugation to produce useful, far-field radiation. Analysis of the angle dependence of this far-field emission, together with theoretical modelling enables us to establish the nature of the optical modes guided by the structure. We show that the dispersion of the modes supported by corrugated polymer films depends on the depth of modulation of the corrugation and find that if the periodic corrugation is strong enough photonic band gap effects may be induced. We also address the question of whether Bragg scattering of the non-radiative guided modes, including surface plasmon polariton modes may increase the efficiency of the emission. We measure and compare the efficiency with which radiation is produced by planar and corrugated structures, finding the corrugated structures to be up to a factor of 2.6 more efficient. We indicate how our results may be used in the search for ways to improve the efficiency of devices based on light emitting thin films.

The efficiency of organic light emitting diodes (LEDs) based on light emitting polymers is further investigated in this chapter. As noted in chapter 5, the overall efficiency of such devices primarily involves two aspects, the efficiency with which photons may be generated [Shuai et al. (2000)] and the efficiency with which they may be extracted from the light emitting material [Benisty et al. (1998)]. Similar to the work of chapter 5, it is the second of these aspects that we focus upon here. In the previous chapter we were interested in calculating the potential for any increase in polymer LED efficiency (by determining the fraction of power wasted into guided modes of a planar device). However, in this chapter we look at a specific method that could provide a mechanism for increasing the radiative efficiency of a structure.

As we have already observed, photons may be produced when the excitons that form as a result of injecting electrons and holes into the device recombine. Owing to the high refractive index of most light emitting polymer films [Boudrioua et al. (2000)], many photons remain trapped by total internal reflection in the organic film as waveguided light [Benisty et al. (1998), Greenham et al. (1994), Gu et al. (1997)]. This waveguided light is in general wasted since it is either absorbed by the polymer film or emitted from the edge of the device in a way that does not easily allow it to be converted to useful radiation.

Several approaches have been explored to overcome this problem, these include the incorporation of the light emitting material into an optical microcavity [Friend et al. (1999), Tang and VanSyke (1987), Dodabalpur et al. (1996), Slusher and Weisbuch (1994)], scattering of waveguided light via roughness [Schnitzer et al. (1993), Windisch et al. (1999)], and modifying the edges of the LED structure [Gu (1997)]. Here we explore an alternative by looking at how periodic microstructure can be used to Bragg scatter waveguided light into the forward (useful) direction [Adams et al. (1982)]. We do this by incorporating a corrugated profile into the thin polymer film. In particular we deposit our emissive polymer layer on top of a metallic diffraction grating. Light trapped as waveguide modes in the polymer layer may then Bragg scatter off the periodic corrugation to produce useful radiation. In previous work by Lupton et al. (2000) it was shown that using a corrugated polymer LED system resulted in an increase of 2.0 ± 0.2 in the external efficiency of the device as compared with a planar structure. Optimising efficiency using this approach will require a thorough knowledge of the way in which guided modes interact with periodic corrugations. In this chapter we focus on the nature of these guided modes and how their dispersion is affected by introducing corrugations of varying amplitude.

Our investigation looks at how Bragg scattering from periodic corrugations modifies the spectrum of the emitted light, and how the dispersion of the optical modes associated with the structure can be found by analysing the angle dependence of the emitted spectra. In particular, Bragg scattering allows modes that would otherwise be confined to the polymer layer to couple to

far field radiation, and thus be seen in the emission spectra. The propagation angle (θ) in air produced via the Bragg scattering of a guided mode is given by,

$$\mathbf{k}_0 \sin \theta = \mathbf{k}_m \pm j \mathbf{k}_g \quad (6.1)$$

where \mathbf{k}_0 is the free space wavevector of light at the emission frequency in question, \mathbf{k}_g is the Bragg vector, the magnitude of which is equal to $2\pi/\lambda_g$, with λ_g being the pitch of the corrugation; \mathbf{k}_m is the in-plane wavevector of the unscattered mode and j is an integer indicating the order of the Bragg scattering. We investigate how both the spectra and dispersion of the optical modes depend on the modulation depth of the periodic microstructure.

To build up a picture of the Bragg scattering process in light emitting polymer layers and the dispersion of the modes involved, we fabricated a variety of polymer film/metal samples including both planar structures and structures that were periodically corrugated (with varying depths). Sample fabrication is discussed in section 6.3. For each sample we measured the emission spectrum for normal emission, the emission spectrum as a function of emission angle, and the emission spectrum integrated over all emission angles. Details of these measurements are given in section 6.4, where we discuss the results obtained, making use of two theoretical models for the emission from such structures. The theoretical models we make use of in this chapter are; the planar theory for dipole emission of chapter 4, and a diffractive optics model that describes the reflection of light from corrugated structures (outlined in section 6.2). In section 6.5 we summarise our findings.

6.2 Method of Chandezon et al.

In this section we briefly outline the differential method of Chandezon et al. (1982) that accounts for the diffraction of planar electromagnetic waves from gratings [Harris et al. (1996), Tan et al. (1998), Tan et al. (1999), Barnes et al. (1996)]. This method is the basis for the modelling of the reflectivity of the corrugated systems that we study in this chapter. In modelling the reflectivity of these structures the dispersion of the modes of these structures is often evident. This is because the reflectivity drops when the frequency and angle of incidence of light incident on the structure matches that of a guided mode. The

approach of Chandezon et al. fundamentally involves using a co-ordinate transformation that maps the corrugated interfaces onto planes. For example, given the equation of an interface, in Cartesian co-ordinates (x,y,z) , as

$$y = a(x) \quad (6.2)$$

where the function $a(x)$ gives the shape modulation of the interface, a simple transformation to a new co-ordinate system (u,v,w) is used where

$$\begin{aligned} u &= y - a(x) \\ v &= x \\ w &= z \end{aligned} \quad (6.3)$$

The interface is clearly a plane in this new basis, and this considerably simplifies the solution of the boundary conditions, where the tangential components of the \mathbf{E} and \mathbf{H} fields need to be matched at the interface. However, this transformation results in a more complex form for Maxwell's equations, which must be satisfied. The solution involves making an appropriate Fourier expansion of these equations in the v -variable to produce a set of coupled differential equations which, after truncation, can be solved as an eigenvalue problem [Chandezon et al. (1982), Preist et al. (1995), Harris et al. (1996), Tan et al. (1998), Tan et al. (1999), Barnes et al. (1996)].

6.3 Experimental

Figure 6.1 shows a schematic of our corrugated samples. The samples studied were fabricated on fused silica substrates that were covered by a layer of photoresist deposited by spin coating. One half of the photoresist was corrugated with a period of ~ 400 nm and the other half was left planar. Three different corrugations were investigated, one with an amplitude of ~ 13 nm, another with an amplitude of ~ 20 nm, and the other with an amplitude of ~ 90 nm, we refer to these samples as A, B and C respectively. Corrugation profiles were determined by measuring the angle-dependent reflectivity of each sample, details of which are given below. The corrugation was made by exposing the photoresist layer to an interference pattern produced using an Ar^+ laser, followed by wet chemical development [Kitson et al. (1996)]. Approximately 50 nm of gold was deposited by evaporation onto both the corrugated and flat areas of each of the samples, this was followed by deposition of a film of the

conjugated polymer MEH-PPV by spin-coating from a chlorobenzene solution. By adjusting the spin speed and temperature of deposition, the thickness of the resulting film could be controlled. For each of our samples the polymer thickness was ~ 190 nm.

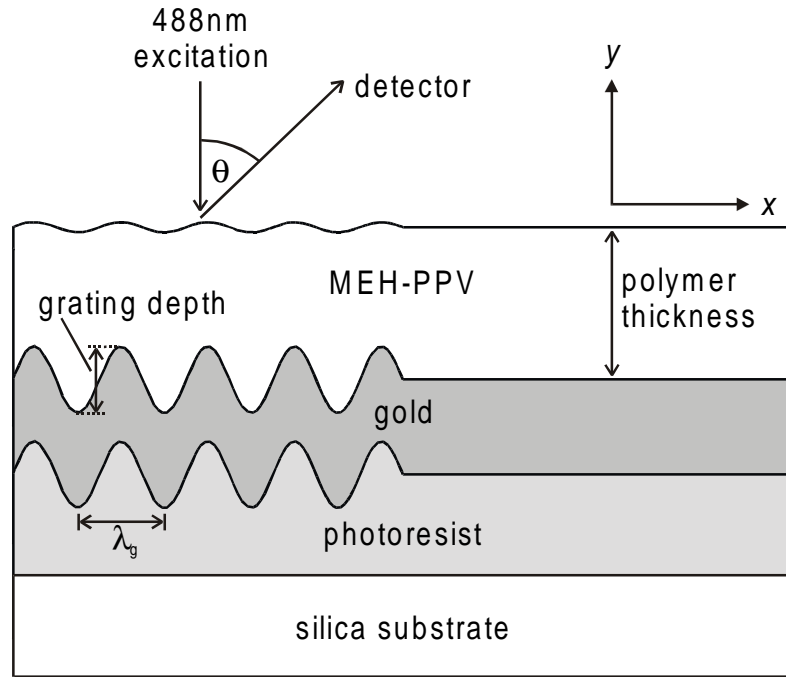


Figure 6.1. A schematic of the sample structures we fabricated. One half of the sample was corrugated and the other half was left flat. The grating depth corresponds to approximately twice the amplitude of the fundamental Fourier component describing the corrugation ($\sim 2a_0$).

In order to characterise the surface profile of the corrugated regions a small area of the sample was left uncovered by the polymer and was subsequently coated with a gold film of thickness 150 nm by thermal evaporation. The reflectivity of TM polarised light from this region was then measured as a function of the angle of incidence. The presence of the corrugated surface enables the incident light, at an appropriate incident angle, to couple to surface-plasmon polariton (SPP) modes at the gold/air interface. Coupling of incident radiation to these SPP modes produces sharp dips in the angle dependent reflectivity. By matching suitable theoretical models of the reflectivity (based on the diffractive optics model outlined in section 6.2), the corrugation profile and dielectric permittivity of the gold may be obtained [Wood

et al. (1995)]. The values for the dielectric constant are in good agreement with published values [Innes and Sambles (1987)]. It is convenient to represent the profiles of the corrugated surfaces as a Fourier series, i.e. $y(x) = a_0 \sin(k_g x) + a_1 \sin(2k_g x + \phi_1) + \dots$, and it is with this approach that we found our corrugation profiles, as given in Table 6.1.

SAMPLE	a_0 (nm)	a_1 (nm)	ϕ_1 (deg)	pitch, λ_g (nm)
A (weak)	13 ± 1	-	-	388 ± 1
B (weak)	20 ± 1	7 ± 1	90	400 ± 1
C (strong)	90 ± 4	-	-	400 ± 1

Table 6.1. The parameters defining the corrugation profiles for our three samples, as derived by fitting theory to the measured reflectivity data obtained from of a region of corrugated photoresist coated only by an optically thick layer of gold.

6.4 Results and discussion

Photoluminescence (PL) measurements were carried out at room temperature, with excitation provided by the 488 nm line of an Argon-ion laser. The resulting emission was collected by a fibre bundle and the spectrum of the emission recorded using a spectrometer and CCD array detector. By positioning the fibre at different angles with respect to the excitation spot on the sample, emission spectra were recorded as a function of emission angle. Furthermore, measurements of the emission spectrum integrated over all angles, using an integrating sphere, were also made to measure any overall changes in the emission efficiency as a result of using a corrugation in the sample structure.

6.4.1 Weak corrugation (samples A and B)

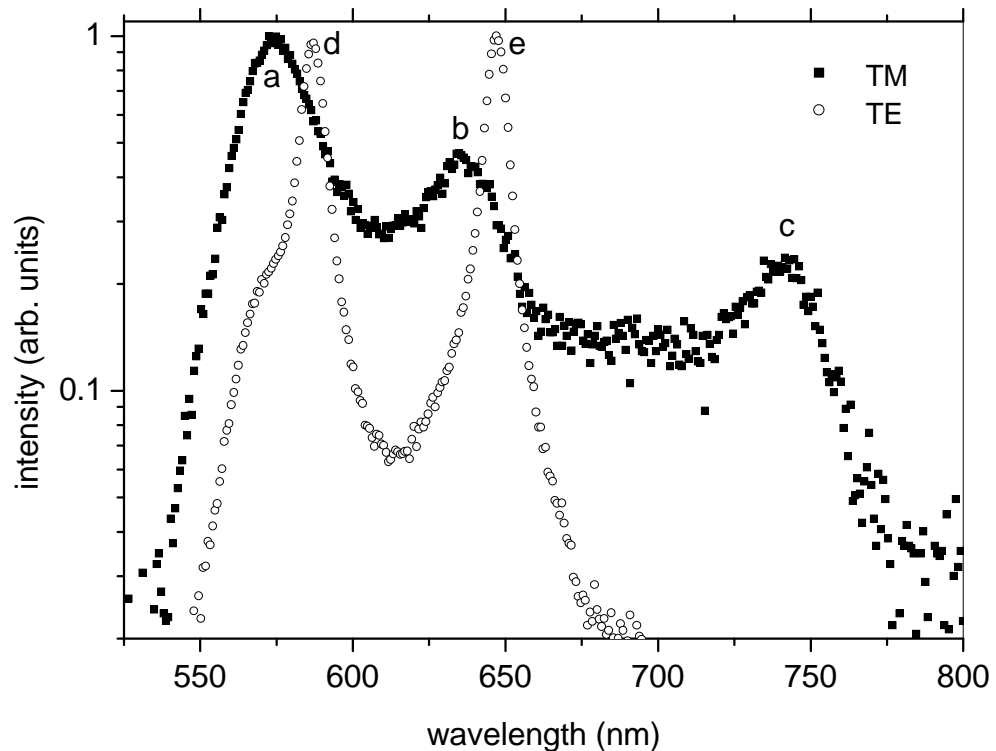


Figure 6.2. An example of the angle dependent emission spectra measured from our samples. This data is for emission from the corrugated region of sample B, at an angle of 12° to the sample normal. The peak features are labelled for each polarisation and correspond to the points that we plot to identify the dispersion of Bragg scattered modes in the structure. The feature labelled a corresponds to a natural peak in the emission from the polymer at ~ 570 nm, and as such will show little angle dependence.

Figure 6.2 shows an example of the angle dependent emission data obtained for sample B (a sample with a relatively weak corrugation, depth to pitch ratio of $\sim 7\%$) for emission at an angle of 12° to the sample normal. The MEH-PPV polymer we have used has a main emission peak at ~ 570 nm (clearly indicated in the emission data from the planar region of each sample, see figure 6.9) that is seen most clearly in the TM polarised data of figure 6.2, and is labelled a. The data from the corrugated regions of the samples shows

'extra' peaks that are also labelled; b and c for the TM polarisation, d and e for the TE polarisation. The spectral position of these peaks depends on the emission angle at which the spectrum is recorded, a characteristic of Bragg scattered modes. The Bragg scattered nature of these 'extra' modes becomes clearer when we investigate the spectral position of the peaks as a function of emission angle. In figure 6.3 we show how the dispersion of the modes associated with a flat (un-corrugated) sample region behave. This schematic is of the waveguided and SPP modes we would find in such a structure where the polymer film is birefringent [Boudrioua et al. (2000)], with a greater in-plane index than normal index.

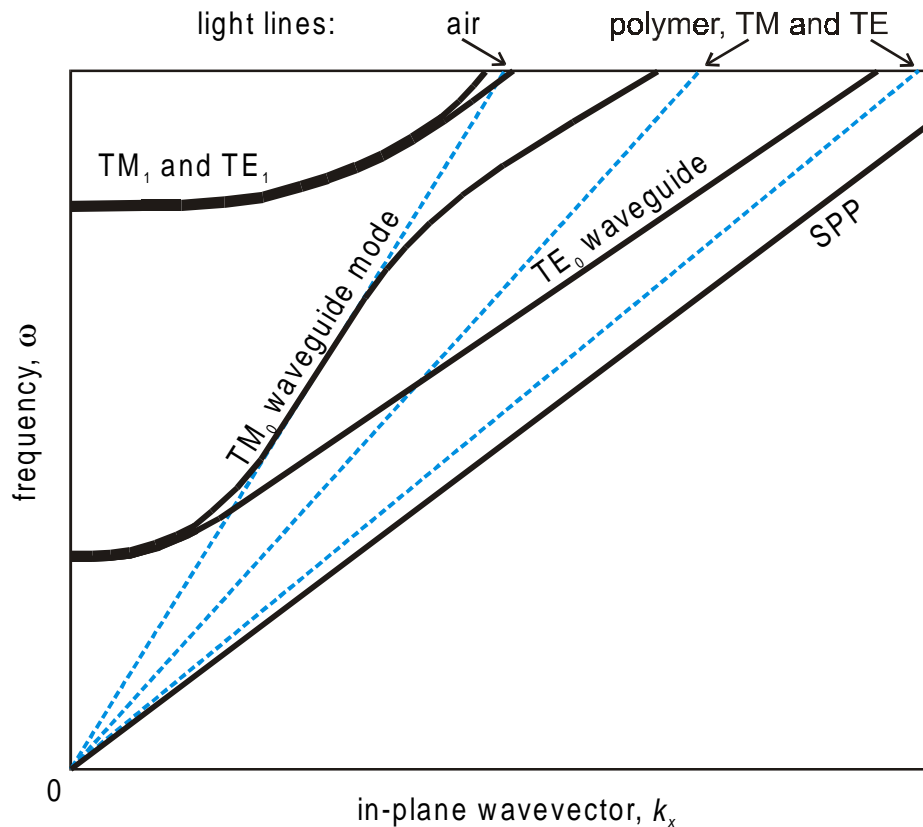


Figure 6.3. A schematic of the mode dispersion that we expect for the flat sample region. The polymer is birefringent, the in-plane index being higher than the normal to the plane index. The SPP mode of the polymer/gold interface is shown as well as the lowest order TE and TM polarised waveguide modes of the polymer layer.

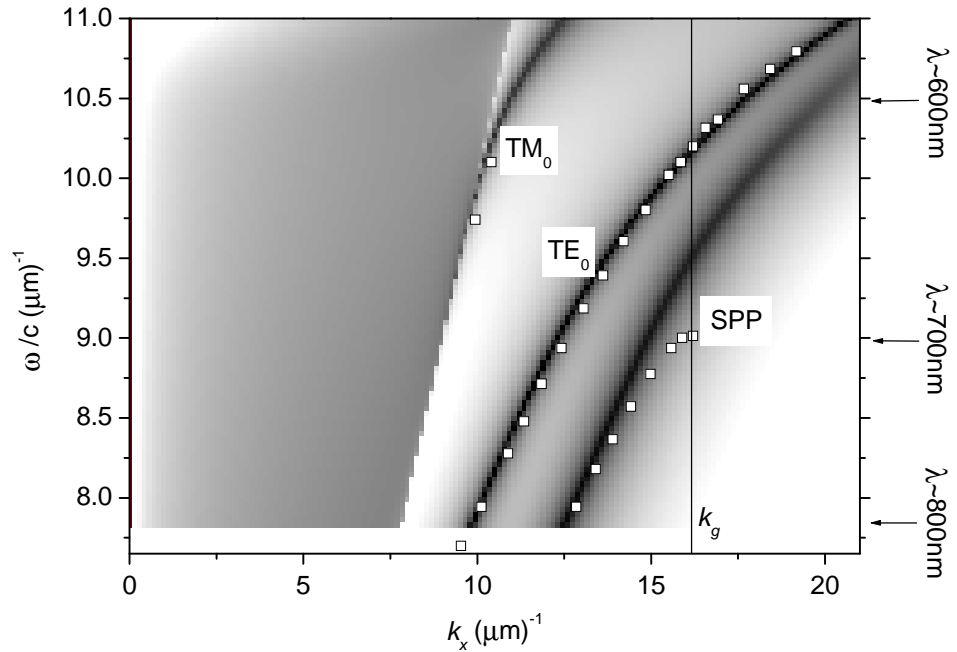


Figure 6.4. The grey scale indicates the mode dispersion for the flat sample region, based on a model describing the strength of coupling between an emitter in the polymer coupling to modes of the structure. The hollow square data is based on the emission data for the corrugated region of sample A, and corresponds to peaks in the detected emission, that has been adjusted so as to be represented in the extended zone.

Let us now switch our attention to sample A. In figure 6.4 we have plotted the positions of the measured emission peaks for sample A, determined in a manner similar to that shown for sample B in figure 6.2, in the form of a dispersion diagram, i.e. as a function of their frequency and in-plane wavevector. In plotting the data we have taken account of the different Bragg scattering processes indicated in equation 6.1. In this way we were able to ensure that the data are represented in the extended zone, rather than the reduced zone. The benefit of doing this is that it allows us to make a comparison with a theoretical model that helps identify the nature of the modes involved.

One way to theoretically model the modes associated with a given structure is to calculate the rate at which power is lost from an emissive dipole embedded within the structure in question (see section 2.3.4) [Ford and Weber (1984), Salt and Barnes (1999)]. This we have done for a structure corresponding to the planar part of sample A - the results are shown in figure 6.4, the power dissipated by the dipole is evaluated as a function of in-plane wavevector and emission frequency, and is represented as a grey scale map in the figure. Dark regions in the figure correspond to strong power dissipation and are thus indicative of a mode of the structure to which the dipole couples. The strength with which different modes appear in this type of calculation depends on both the location and orientation of the dipole source within the multi-layer structure. Importantly however, the position of the modes on the dispersion diagram does not depend on either the location or orientation of the dipole source. For our calculations we chose the dipole source to be located in the polymer layer 90 nm above the gold interface and used only the total thickness of the polymer layer as an adjustable parameter in matching the results of our calculation to the data shown in figure 6.4. The polymer was assumed to be birefringent, the optical constants and their dispersion being taken as those published elsewhere [Boudrioua et al. (2000)]. We also assumed that the polymer was lossless, and took the dispersion of the gold parameters from the literature [Innes and Sambles (1987)]. In matching this theory to the experimental data we deduced the thickness of the polymer in sample A to be 190 nm.

Figure 6.4 also shows the experimental data for the Bragg scattered peaks from sample A. It can be seen that there are three modes responsible for the Bragg scattered peaks seen in the emission spectra from sample A. One of these modes is the surface plasmon polariton mode whose existence is associated with the gold/polymer interface, and is labelled as SPP in the figure. The other two modes are the lowest order TE and TM modes of the gold/polymer/air waveguide, labelled TE_0 and TM_0 in the figure. An analysis of the polarisation of the emitted radiation (not shown) confirms the polarisation assignments made here. We note that the optical parameters we have assumed for the media involved, notably the birefringence and dispersion of the polymer, and the dispersion of the gold, seem well able to account for the measured

modal dispersion patterns, despite the model being based on a planar structure. That the experimental data for the corrugated region of sample A should agree with the planar model indicates that for this corrugation amplitude the modes are Bragg scattered, but otherwise unaffected by the corrugation. The possible exception appears to be the SPP mode where a difference between experiment and theory is seen where the SPP mode meets the Brillouin zone boundary at $k_x=k_g$. This is indicative of a band gap arising from the Bragg scattering of the SPP mode. We would expect band gaps to appear when modes cross (same energy and in-plane wavevector) if the corrugation is effective in providing coupling between them.

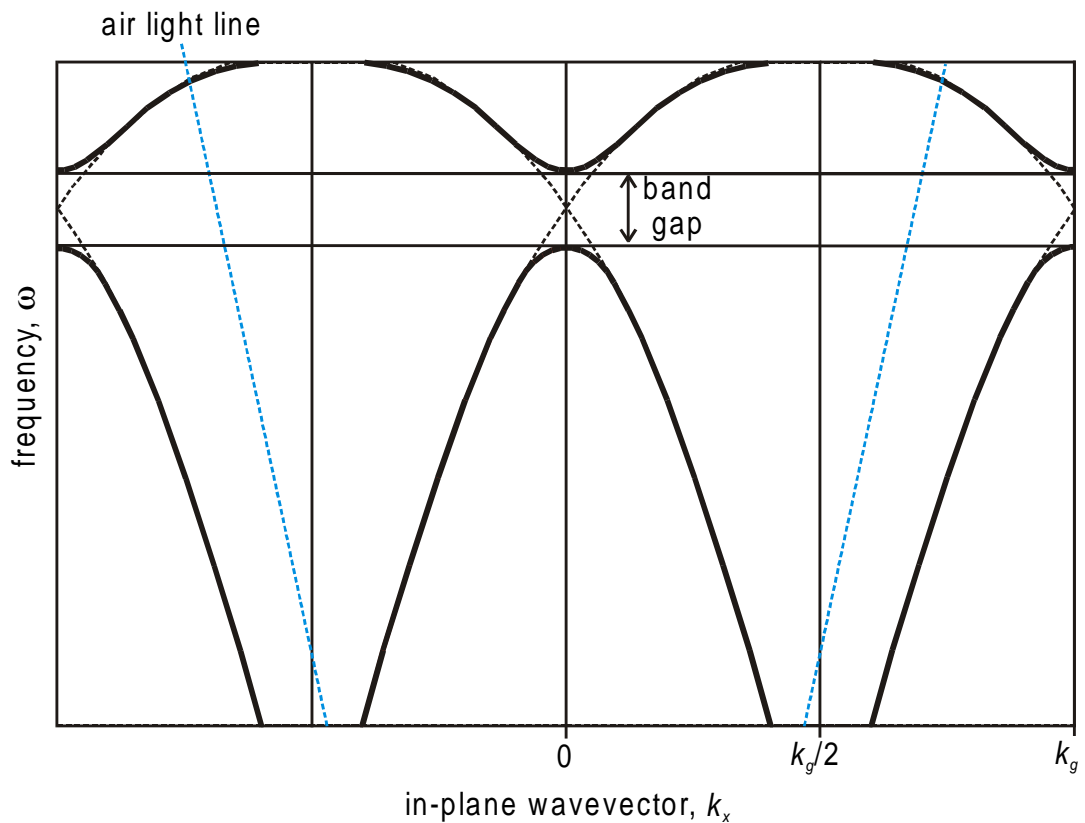


Figure 6.5. A schematic of the effects of Bragg scattering of the SPP mode in our samples. The possible band gap generation where modes cross is indicated.

In figure 6.5 we present a schematic of the mode structure associated with a Bragg scattered SPP mode, and how we would expect band-gaps to appear

when the modes cross if there is sufficient coupling between them. To examine this aspect in more detail we need to switch to a theoretical model that allows us to directly assess the influence of the corrugation.

Unfortunately, no good model yet exists that allows us to predict the emission spectrum of a broadband source embedded in a corrugated structure [Amos and Barnes (1999)]. As an alternative we have used a diffractive optics modelling approach (briefly outlined in section 6.2) that allows the reflectivity of corrugated structures to be determined [Chandezon et al. (1982), Harris et al. (1996), Tan et al. (1998), Tan et al. (1999), Barnes et al. (1996)]. As with the characterisation of the corrugation profile technique mentioned in section 6.3, the reflectivity drops when the frequency and angle of incidence of light incident on the structure matches that of a guided mode.

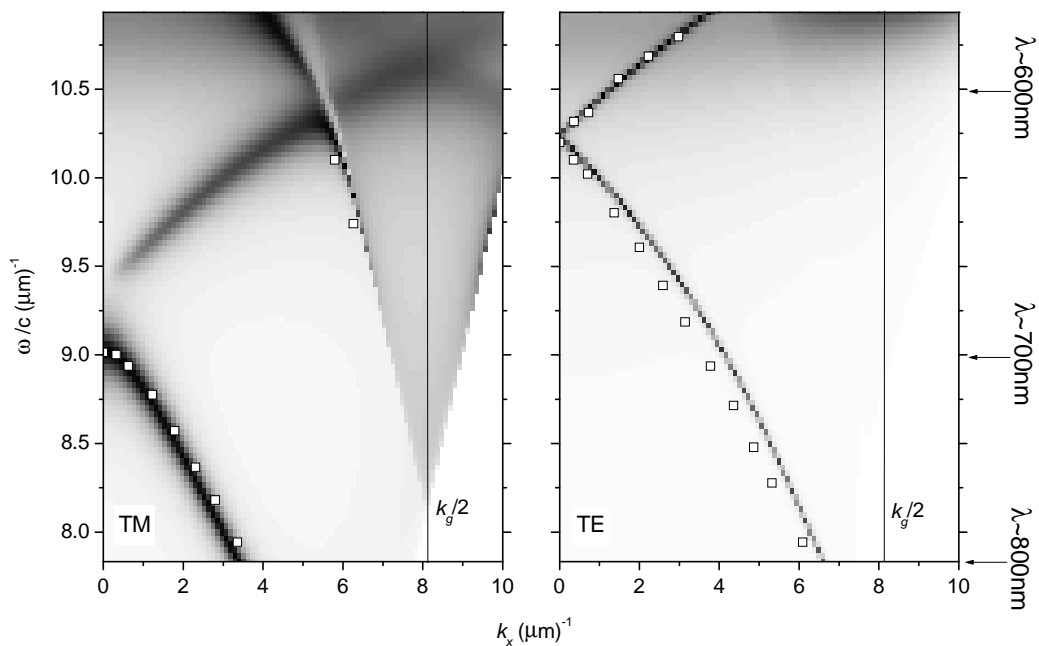


Figure 6.6. The grey scale indicates the mode dispersion for the corrugated region of sample A, based on a reflectivity model of the system. The hollow square data corresponds to peaks noted in the angle dependent emission spectra measured for the sample. The parameters describing the corrugation in the model are $a_0=13$ nm, $a_1=3$ nm, $\phi_1=90^\circ$.

In figure 6.6 we have re-plotted the peak position data shown in figure 6.4, shown now 'as measured' rather than projected into the extended zone, displaying it as a function of frequency and in-plane wavevector. The grey scale data plotted this time has been produced using the diffractive optics modelling procedure mentioned in section 6.2. This model again incorporates the birefringence and dispersion of the polymer, and the dispersion of the gold parameters. In this model the corrugation profile of the polymer/air interface and the polymer thickness were used as adjustable parameters, based on the data shown in table 6.1. Here, dark regions represent low reflectivity and correspond to the coupling of incident light to a mode of the structure. This procedure has been undertaken for both TE and TM polarisations. As with figure 6.4, figure 6.6 shows a good agreement in the mode positions determined by experiment and predicted by theory. We can also see here that the deviation in the dispersion of the SPP mode is now well accounted for, it arises due to a second order Bragg scattering process producing a band gap in the dispersion of the SPP mode [Barnes et al. (1996)]. Such band gaps are discussed in more detail in the section 6.4. For now we again note that the polarisation of the different modes as shown in figure 6.6 agrees well with the assignments we made in figure 6.4.

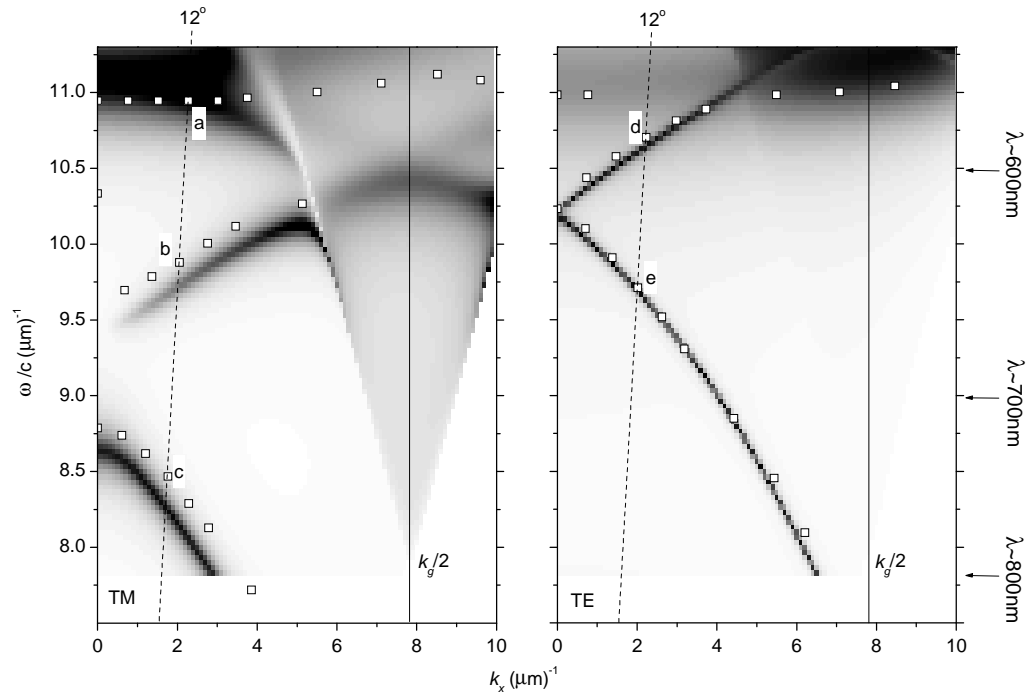


Figure 6.7. The grey scale indicates the mode dispersion for the corrugated region of sample B, based on a reflectivity model of the system. The hollow square data corresponds to peaks noted in the angle dependent emission spectra measured for the sample. The parameters describing the corrugation in the model are $a_0=19$ nm, $a_1=6$ nm, $\phi_1=90^\circ$, and a polymer average thickness of 170 nm. A dashed line marks the 12° angle in air for which sample emission data is shown in figure 6.2, and the features labelled a, b, c, d, and e correspond accordingly. The feature labelled a corresponds to a natural peak in the emission from the polymer at ~ 570 nm.

As with sample A, in figure 6.7 we plot the dispersion of the features seen in the emission from sample B. The points corresponding to the peaks seen in the emission spectrum recorded at 12° from the sample (figure 6.2) are clearly marked in figure 6.7. For sample B the band gap evident in the dispersion of the SPP mode is larger than for sample A, although there is still no band gap induced in the lowest order TE waveguide mode. To see such effects still stronger modulation is required and this is discussed in the next section

6.4.2 Stronger corrugation (sample C)

As we have seen in the previous section, the weak corrugation of sample A had only one significant effect on the light emitted by the film, the presence of Bragg scattered modes. The effects of Bragg scattering were also the main features of the results for sample B, but a very clear band gap in the SPP mode was also evident. To address the question of whether other effects occur for stronger modulations we next examined a third sample with a deeper corrugation, having an amplitude of 90 nm. The emission spectra from sample C were analysed in a similar fashion to those of samples A and B, as indicated in figure 6.2. This analysis showed that there are two main differences that arise as a result of the increased corrugation amplitude. These changes are best illustrated through a comparison of the position of the measured modes and the reflectivity of the structures, based on the profiles and materials involved, just as was undertaken for the weaker corrugations in figures 6.6 and 6.7. The results for the stronger corrugation, sample C, are shown in figure 6.8. We first note that the TE mode has been significantly distorted in the region of the Brillouin zone boundary at $k_x=0$; a photonic band gap has opened up for this mode due to the increased strength of the Bragg scattering afforded by the stronger corrugation. Such features are a well known phenomenon [Yablonovitch (1987), Boroditsky et al. (1999), Salt and Barnes (1999), Kitson et al. (1996)]. This modification to the dispersion of the modes is important in that it allows us to do more than simply couple guided modes to radiation using Bragg scattering. The introduction of photonic band gaps and band edges alters the photo-physics of the emission process and may be valuable in increasing the functionality of emissive devices, an aspect we discuss in section 6.4. For the TE case, we note in particular how the predicted reflectivity provides a fair match to the mode positions measured via emission. This shows that knowledge of the details of the corrugation profiles of the interfaces involved is vital if a proper understanding of corrugated light emitting structures is to be acquired.

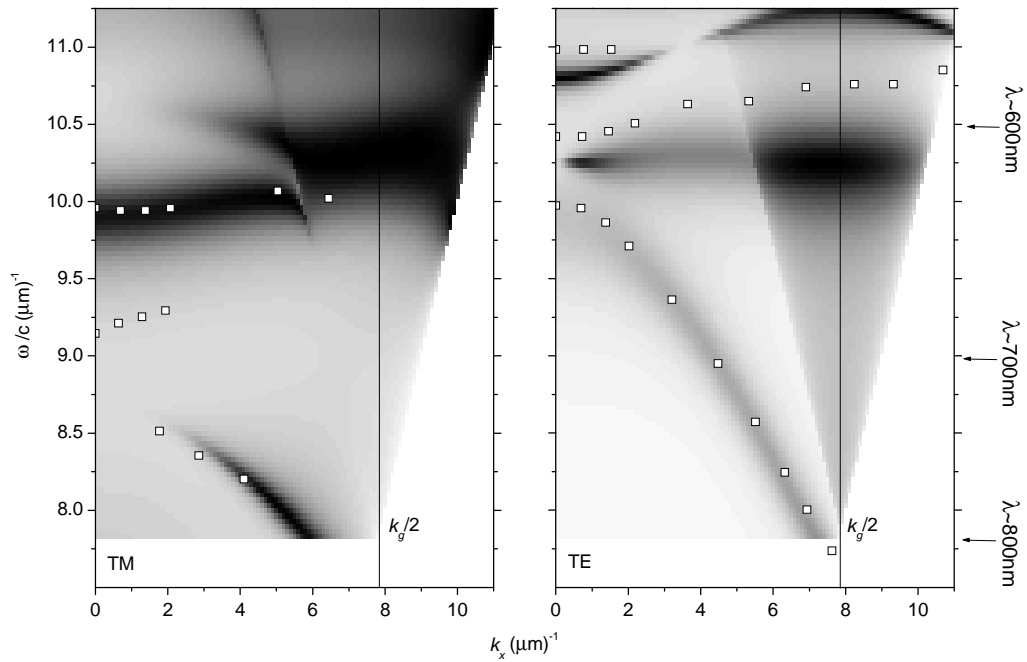


Figure 6.8. The grey scale indicates the mode dispersion for the corrugated region of sample C, based on a reflectivity model of the system. The hollow square data corresponds to peaks noted in the angle dependent emission spectra measured for the sample. The parameters describing the corrugation in the model are $a_0=90$ nm, $a_1=5$ nm, $\phi_1=90^\circ$, and a polymer average thickness of 190 nm.

These results compliment those recently reported for the modes of light emitting polymers in metal-clad microcavities [Salt et al. (2000)]. There too, photonic band gap effects were observed. The results shown here demonstrate that a well confined optical microcavity is not required in order that photonic band gap effects be observed. The samples examined here had only one high reflectivity mirror, the polymer/gold interface, yet still showed photonic band gap effects.

The TM polarised results for the emission from sample C (figure 6.8) also show some very good agreement with the reflectivity model, although one particular feature in the emission spectra (at $\omega/c = \sim 9$ ($\mu\text{m})^{-1}$ in figure 6.8) does

not appear to correspond to any feature seen in the model. This may be a result of the fundamental difference between the coupling conditions for external radiation to the modes of the structure (the reflectivity model) and the coupling conditions for emission from within the structure to these modes (the experiment). That is to say, though an embedded emitter may couple to a given mode of a structure, the coupling of incident light to that mode may be very weak. In the absence of an appropriate theoretical model for emission in corrugated structures this situation can not be resolved.

The significance of these results is twofold. Firstly, wavelength scale corrugation produces Bragg scattering that allows some of the light that would otherwise be trapped in the polymer to be scattered out as far-field radiation. Secondly, the same corrugation, if strong enough, may alter the dispersion of the allowed modes through the introduction of photonic band gaps. First let us concentrate on the Bragg scattering. From a device point of view it is important to be able to ascertain whether the corrugation provides a net increase in the efficiency of the light emitted by the structure. The answer to this question is not obvious; waveguide light may be Bragg scattered out, but light that would have been directly radiated can presumably be Bragg scattered into waveguide modes and thus not emerge in the far field, instead being lost to absorption. To address this question we undertook measurements of the integrated photoluminescence spectra by placing the sample within an integration sphere. The results of these measurements are the subject of the following section.

6.4.3 Integrated emission intensity

To determine the integrated photoluminescence intensity from our samples, we recorded emission spectra with the samples mounted in an integrating sphere [Greenham et al. (1995)]. In this way all the emission into the far field could be accounted for. The system used allowed the amount of pump power absorbed by the polymer layer to be accounted for. Briefly, the absorbed pump power was determined by comparing the pump throughput of the sphere for the samples being measured with that of a blank substrate.

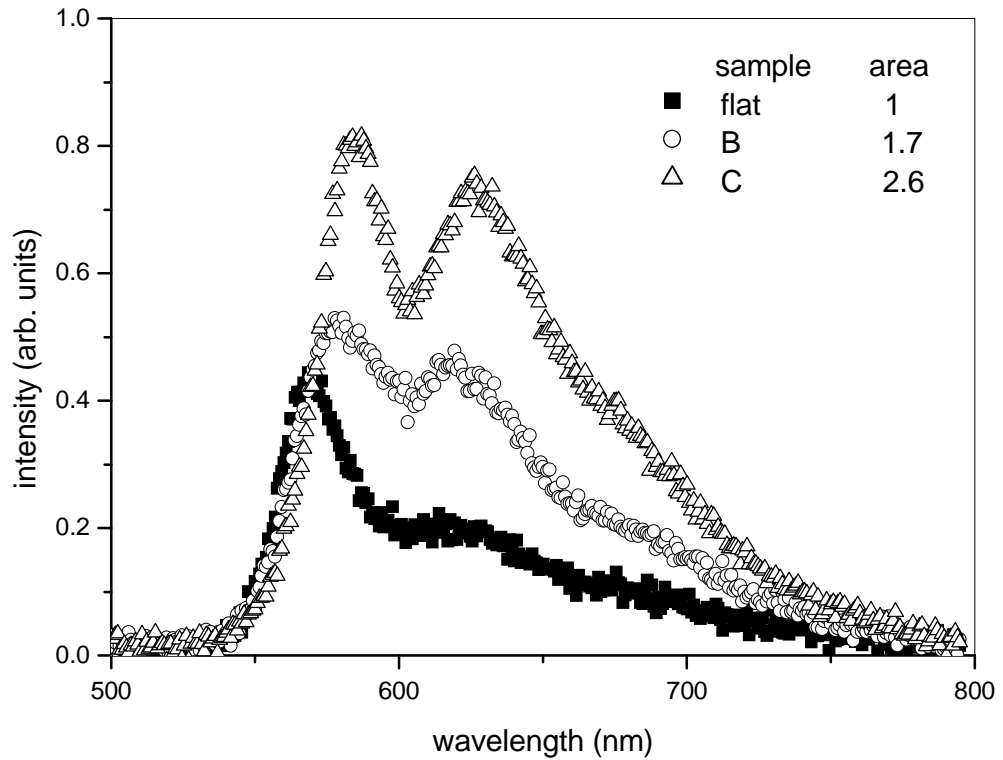


Figure 6.9. The emission spectrum integrated over all angles, for the corrugated regions of samples B and C, and for a flat sample region for comparison. The area under each plot gives a measure of the total intensity of the emission from each sample; the values given are normalised to the flat sample case.

The results for different structures, a flat sample region and the corrugated regions of samples B and C, are shown in figure 6.9. We see that as hoped, the integrated emission intensity is indeed greater for the corrugated samples. By relating the areas under each plot, we obtain a measure of the total intensity of the emission from the corrugated samples, relative to the emission from the flat structure. The relative total intensity for the emission from samples B and C, with respect to the flat system, is 1.7 ± 0.2 and 2.6 ± 0.2 respectively. From these results it is clear that we need to do more to investigate the enhancement in output as a function of amplitude of the corrugation. It is expected that there will be an optimum depth, just as there is an optimum depth for corrugations used to couple incident radiation into waveguide and surface

modes [Ræther (1998)], and that the optimum depth will depend on the details of the structure.

6.5 Summary

We have investigated the effect of corrugating thin films of light emitting polymers on the emission characteristics. By measuring their emission spectra for a range of emission angles, and comparing these data with those of theoretical models we have been able to identify the modes involved. For the structures examined we found that emission from the polymer was coupled to two waveguide modes and one surface-plasmon polariton mode, these modes were in turn coupled to radiation by Bragg scattering resulting from the corrugated nature of the films. For the most weakly modulated sample, sample A, we found that the dominant effect of the corrugation was simply to allow trapped modes to couple to radiation. There was also an indication of a band gap being generated in the SPP mode. This band gap is evident in the curvature of the low energy branch of the mode near $k_x=0$, although no features were seen in the data that corresponded to the high energy branch of this mode, the band gap is clearly seen in the theoretical reflectivity plot (figure 6.6). The band gap in the SPP mode is clear (and also greatly increased) in the data from sample B, a sample with a greater corrugation depth.

For the most strongly modulated sample, sample C, we found additional effects. The modes in this sample, in addition to being coupled to radiation via Bragg scattering, had their dispersion modified to the extent that photonic band gaps were opened up in both the SPP and TE waveguide modes. The presence of such band gaps raises an interesting possibility, that of controlling the emission of light emitting microcavity devices by 'band engineering' [Dowling et al. (1994)]. In this way we might, for example, expect to alter the angle dependence of the colour of emission from devices incorporating wavelength scale microstructure such as corrugations. Another important aspect of our findings is that we have shown that emission from within the light emitting polymer does couple to the SPP mode of a nearby metallic surface *and* that this SPP mode, usually considered a loss mechanism, can, at least in part, be

recouped by Bragg scattering. The significance of these findings rests in the fact that LED structures commonly employ a metal cathode.

We also saw that corrugating the films produced an increase in the overall emitted intensity, up to a factor of 2.6 for the deepest corrugation we investigated. These results, in conjunction with those recently reported on electroluminescence from corrugated polymer LEDs [Lupton et al. (2000)], shows that the wavelength scale microstructure approach may be an important technique in the quest for improved device efficiency. Based on the previous work of chapter 5, we expect that the factor of 2 reported by Lupton et al. may be significantly improved upon, if all guided light were to be scattered out from the structure.

The corrugation in our structures is performing two tasks, the scattering of modes into far field radiation and perturbing the dispersion of the modes. Identifying appropriate corrugation profiles to optimise both aspects will require considerable further investigation. In particular, care will need to be taken to ensure that modulation depths are kept at a level that allows efficient coupling between guided modes and far field radiation.

An important aspect that we have so far not discussed is the limitations that our 1-dimensional corrugations impose. We have only examined the case of emission in a plane that includes the Bragg vector of our corrugation. However, emission from the polymer will take place in all in-plane directions. It has already been shown that by making use of 2-dimensional texturing (bi-gratings), the photonic band gap effects mentioned above can be retained for all in-plane propagation angles [Salt and Barnes (2000)]. The work on 2-dimensional texturing has been carried out for passive microcavities, and we expect it should apply just as well to those incorporating light emitting materials such as the polymer used here.

The use of corrugations to control light emitting properties has been established and some of the opportunities identified. Work on these fascinating aspects of corrugated light emitting structures will be the subject of future work. Additionally, the development of a model to describe emission from within corrugated structures would be of immense benefit in furthering our understanding of the types of corrugated device we have studied in this chapter.

Chapter 7

Summary and future work

7.1 Summary

In chapter 3 we used expressions for calculating the total power dissipated by an emitter in a cavity and the power radiated into the far field by such an emitter (based on equations from chapter 2) to investigate how well different microcavity structures perform in controlling emission from sources within them. Microcavities can clearly be used to improve the radiative efficiency of thin film emissive systems, and the nature of the materials used for the confining mirrors has been shown to noticeably affect this result. Our modelling showed that a structure with metal mirrors, though not as efficient, still compared well with DBR mirror structures, despite the much greater losses associated with metals. In assessing device performance the importance of considering dipole orientation and position within the cavity for optimisation was also highlighted.

In chapter 3 we focused our attention on emissive layers with refractive indices typical of organic polymers, however, we had not accounted for the often significant birefringence of thin films of such materials. In chapter 4 we established a suitable model for radiative emission from thin birefringent films and successfully compared it with experimental data. We concluded that the method of spin coating the thin films of MEH-PPV in experiments orients the polymer molecules predominantly in the plane of the film (which also corresponds directly to the birefringence of these layers), this is in agreement with previous findings [McBranch et al. (1995)]. To model the measured emission results from our thin MEH-PPV film (~30 nm) we found it was only the dipole orientation that needed to be accurately accounted for, birefringence had no significant effect.

In chapter 5 we presented a more comprehensive model for the radiative emission of sources embedded within thin polymer films. This model accounts for the broad spectral width of the emission from light emitting polymers and

also accounts for an excitation profile that may be necessary to describe the emissive region of the polymer. By using the intrinsic spectrum that we had calculated and the dispersion of the complex permittivity for MEH-PPV we modelled the emission measured from a photo-excited MEH-PPV film (~80nm) on a silica slide and found good agreement. We then used our model to predict how much power is lost to guided modes (and finally to absorption) in similar structures. We found that for films >100nm thick ~75% of radiative emission never escapes the emissive layer. We next applied our model to an EL device. Using the results of Kim et al. for their EL green emitting polymer LED our modelling predicted the maximum radiative efficiency of the device to be ~10%. We estimated the number of singlet excitons formed per electron flowing in the external circuit of the device as lying between 60% and 100%. This is an interesting result in that it greatly exceeds the 25% expected from simple spin statistics, it is also significantly larger than the value of ~40% that Kim et al. calculated.

Finally in chapter 6 we assessed the effectiveness of using periodic corrugation (in 1-dimension) to increase the efficiency of a PL device. By measuring the emission spectra for a range of emission angles from ~190nm thick MEH-PPV films on gold (corrugated and flat regions), and comparing these data with those of theoretical models we have been able to identify the guided modes of the structures. The effect of the corrugation on these modes, in addition to coupling them to radiation via Bragg scattering, is to modify their dispersion to the extent that photonic band gaps are opened up in both the SPP and waveguide modes if the corrugation is sufficiently deep. We found that corrugating the films produced an increase in the overall emitted intensity; up to a factor of 2.6 for the deepest corrugation we investigated. This clearly indicates the effectiveness of employing corrugation as a means for increasing device efficiency, and, based on the results of chapter 5, we may expect further increases in efficiency to be possible if this method is optimised.

7.2 Future work

The research reported here naturally suggests several avenues for further exploration.

Emission in 1-D corrugated structures

We have considered the effects of emission from within a structure that involved a periodic corrugation and how this may be used to increase the radiative efficiency of a device (chapter 6). To optimise systems like this will require considerable further investigation, since corrugation profiles and other system parameters would need to be chosen that provide the appropriate modifications to mode dispersion and the appropriate scattering. The use of a model that accounts for emission from within such corrugated structures would be invaluable in this regard. The development of such a model will be a major focus for us in the future. The approach we will take to develop such a model would closely follow the method of Chandezon et al. for determining the electromagnetic response of a grating structure [Chandezon et al. (1982), Harris et al. (1996), Tan et al. (1998), Tan et al. (1999), Barnes et al. (1996)] (see appendix **D**). The effects of placing an emitter within a corrugated microcavity are clearly much more complicated than those of a planar system, due to the diffractive orders involved. In particular, the calculation of a decay rate for an emitter in a corrugated cavity would require evaluating the response of this complex system for an appropriately detailed portion of 2-dimensional \mathbf{k} -space (not reduced to a 1-dimensional problem as in the planar case). Furthermore, for a layer of emitters in the planar structure each emitter will possess the same environment, this will not generally be the case in a corrugated structure. As such, any modelling of a realistic corrugated structure will be a task that is several orders of magnitude more computationally demanding than any of the modelling performed in this work.

Emission in 2-D corrugated structures

As we remarked in section 6.4 there are limitations in using just a 1-dimensional corrugation. Clearly emitters can couple to guided modes that propagate in all directions in the plane of the device, and so there must be coupling to modes that can not be scattered by the corrugation. By making use of 2-dimensional texturing (bi-gratings), scattering and maybe photonic band gap effects can be retained for all propagation directions in the plane [Salt and

Barnes (2000)]. As such, this is very likely to result in even more significant increases in device efficiency. As a long-term goal (due to further computational demands) it would be desirable to develop a model of such systems to help with our understanding of them.

Energy transfer

Since there is presently great interest in the field of energy transfer within microcavities [Andrew and Barnes (2000), Basko et al. (2000)] it will be useful to apply the model outlined in section 2.3 to study this process. The energy transfer processes is fundamental in photosynthesis and is of such interest because of its increasing importance in improving LED and laser efficiency. Typical systems studied involve well-defined layers of ‘donor’ and ‘acceptor’ molecules separated by a region of inert spacer molecules, all within a microcavity. By calculating the power flux through planes that are positioned immediately above and below the absorbing acceptor region, the power lost by radiatively decaying donor molecules to the acceptor molecules could be determined.

Publications and presentations

“Efficiency of spontaneous emission from planar microcavities”

J.A.E. Wasey and W.L. Barnes

J. Mod. Opt. **47** (2000) 725-741

“Birefringence and light emission from the polymer LED”

J.A.E. Wasey and W.L. Barnes

Synth. Met. **111** (2000) 213-215

“Effects of dipole orientation and birefringence on the optical emission from thin films”

J.A.E. Wasey, A.N. Safonov, I.D.W. Samuel and W.L. Barnes

Opt. Comm. **183** (2000) 109-121

“Rate and efficiency of spontaneous emission within metal-clad microcavities”

P.T. Worthing, J.A.E. Wasey and W.L. Barnes

J. Appl. Phys. **89** (2001) 615-625

“Efficiency of radiative emission from thin films of light emitting conjugated polymer”

J.A.E. Wasey, A.N. Safonov, I.D.W. Samuel and W.L. Barnes

Accepted for publication in Phys. Rev. B, 2001

“Controlling the optical emission from the polymer MEH-PPV using corrugated thin films”

J.A.E. Wasey, A.N. Safonov, M.G. Salt, B.J. Matterson, M.J. Jory, I.D.W. Samuel and W.L. Barnes

Submitted to Eur. J. Phys., 2001

“Birefringence and light emission from the polymer LED”

J.A.E. Wasey, W.L. Barnes, A.N. Safonov and I.D.W. Samuel
poster at **ICEL2**, Sheffield, U.K., May 1999.

“Optical properties of the light emitting polymer MEH-PPV”

A. Boudrioua, P.A. Hobson, J.A.E. Wasey, W.L. Barnes, B.J. Matterson and
I.D.W. Samuel
poster at **ICEL2**, Sheffield, U.K., May 1999.

“How much energy is lost to which mode when spontaneous emission takes
place inside a metal clad microcavity?”

P.T. Worthing, J.A.E. Wasey and W.L. Barnes
poster at **QE14** Manchester, U.K., September 1999.

“Modification of spontaneous emission from thin polymer films”

A.N. Safonov, B.J. Matterson, J.M. Lupton, I.D.W. Samuel, J.A.E. Wasey, M.G.
Salt and W.L. Barnes
poster at **QE14** Manchester, U.K., September 1999.

“Modelling emission from birefringent polymer films”

J.A.E. Wasey, A.N. Safonov, I.D.W. Samuel and W.L. Barnes
poster at **QELS** 2000, California, May 2000.

References

- Abram I, Robert I and Kuszelewicz R 1998 IEEE J. Quantum Electron.
34 71
- Adams A, Moreland J, Hansma PK and
Schlesinger Z 1982 Phys. Rev. B. **25** 3457
- Amos RM and Barnes WL 1999 Phys. Rev. B. **59** 7708
- Andrew P 1998 PhD Thesis, University of
Exeter
- Andrew P and Barnes WL 2000 Science **290** 785
- Baba T, Hamano T, Koyama F and Iga
K 1991 IEEE J. Quantum Electron.
27 1347
- Barnes WL 1998 J. Mod. Opt. **45** 661
- Barnes WL, Preist TW, Kitson SC and
Sambles JR 1996 Phys. Rev. B. **54** 6227
- Barnett SM, Huttner B, Loudon R and
Matloob R 1996 J. Phys. B - At. Mol. Opt.
29 3763
- Becker H, Burns SE and Friend RH 1997 Phys. Rev. B **56** 1893
- Benisty H, DeNeve H and Weisbuch C 1998 IEEE J. Quantum Electron.
34 1612
- Benisty H, DeNeve H and Weisbuch C 1998 IEEE J. Quantum Electron.
34 1632
- Bororditsky M, Krauss TF, Coccioli R,
Vrijen R, Nhat R and Yablonovitch E 1999 Appl. Phys. Lett. **75** 1036
- Boudrioua A, Hobson PA, Matterson B,
Samuel IDW and Barnes WL 2000 Synth. Met **111** 545
- Brorson SD, Yokoyama H and Ippen E 1990 IEEE J. Quantum Electron.
26 1492
- Bulovic V, Khalfin VB, Gu G, Burrows 1998 Phys. Rev. B **58** 3730

- PE, Garbuzov DZ and Forrest SR
Chance RR, Prock A and Silbey R 1978 Adv. Chem. Phys. **37** 1
Chandezon J, Dupuis MT, Cornet G and Maystre D 1982 J. Opt. Soc. Am. **72** 839
Chigrin DN, Lavrinenko AV, Yarotsky DA and Gaponenko SV 1999 Appl. Phys. A **68** 25
Clemmow PC 1966 *The Plane Wave Spectrum Representation of Electromagnetic Fields* (Pergamon Press, Oxford)
Dodabalapur A 1997 Solid State Comm. **102** 259
Dodabalapur A, Rothberg LJ, Jordan RH, Miller TM, Slusher RE and Phillips JM 1996 J. Appl. Phys. **80** 6954
Dowling JP, Scalora M, Bloemer MJ and Bowden CM 1994 J. Appl. Phys. **75** 1896
Drexhage KH 1974 Prog. Opt. **12** 165
Fink Y, Winn JN, Fan S, Chen C, Michel J, Joannopoulos JD and Thomas EL 1998 Science **282** 1679
Ford GW and Weber WH 1984 Phys. Rep. **113** 195
Friend RH, Gymer RW, Holmes AB, Burroughes JH, Marks RN, Taliani C, Bradley DDC, Dos Santos DA, Bredas JL, Logdlund M and Salaneck WR 1999 Nature **397** 121
Greenham NC, Friend RH and Bradley DDC 1994 Adv. Mater. **6** 491
Greenham NC, Samuel IDW, Hayes GR, Phillips RT, Kessener YARR, Moratti SC, Holmes AB and Friend RH 1995 Chem. Phys. Lett. **241** 89
Gu G, Garbuzov DZ, Burrows PE, Venkatesh S, Forrest SR and Thompson ME 1997 Opt. Lett. **22** 396

- Gymer RW, Friend RH, Ahmed H, Burn PL, Kraft AM and Holmes AB 1993 *Synth. Met.* **57** 3683
- Harris JB, Preist TW, Sambles JR, Thorpe RN, and Watts RA 1996 *J. Opt. Soc. Am. A.* **13** 2041
- Innes RA and Sambles JR 1987 *J. Phys. F – Met. Phys.* **17** 277
- Kim JS, Ho PKH, Greenham NG and Friend RH 2000 *J. Appl. Phys.* **88** 1073
- Kitson SC, Barnes WL and Sambles JR 1996 *IEEE Phot. Tech. Lett.* **8** 1662
- Kitson SC, Barnes WL and Sambles JR 1996 *Phys. Rev. Lett.* **77** 2670
- Kuhn H 1970 *J. Chem. Phys.* **53** 101
- Lukosz W 1980 *Phys. Rev. B* **22** 3030
- Lukosz W 1981 *J. Opt. Soc. Am.* **71** 744
- Lupton JM, Matterson BJ, Samuel IDW, Jory MJ and Barnes WL 2000 *Appl. Phys. Lett.* **77** 3340
- Matterson BJ, Salt MG, Barnes WL and Samuel IDW 1999 *Synth. Met.* **101** 250
- McBranch D, Campbell IH, Smith DL and Ferraris JP 1995 *Appl. Phys. Lett.* **66** 1175
- Meschede D 1992 *Phys. Lett.* **211** 202
- Milonni PW 1994 *The Quantum Vacuum* (Academic Press, San Diego, CA)
- Novotny L 1997 *J. Opt. Soc. Am. A* **14** 91
- Pedrotti FL and Pedrotti LS 1993 *Introduction to Optics* (Prentice-Hall, New Jersey)
- Persson BNJ and Persson M 1980 *Surf. Sci.* **97** 609
- Purcell EM 1946 *Phys. Rev.* **69** 681
- R  ther H 1988 *Surface Plasmons* (Springer-Verlag, Berlin)
- Russell P St. J, Tredwell S and Roberts 1999 *Opt. Comm.* **160** 66

PJ

- Salt MG and Barnes WL 1999 Opt. Comm. **166** 151
- Salt MG and Barnes WL 2000 Phys. Rev. B. **61** 11125
- Salt MG, Barnes WL and Samuel IDW 2001 J. Mod. Opt. **48** 1085
- Samuel IDW 2000 Phil. Trans. R. Soc. Lond. A. **358** 193
- Schnitzer I, Yablonovitch E, Caneau C and Gmitter TJ 1993 Appl. Phys. Lett. **62** 131
- Schnitzer I, Yablonovitch E, Caneau C, Gmitter TJ and Scherer A 1993 Appl. Phys. Lett. **63** 2174
- Shuai Z, Beljonne D, Silbey RJ and Brédas JL 2000 Phys. Rev. Lett. **84** 131
- Sipe E 1981 Surf. Sci. **105** 489
- Slusher RE and Weisbuch C 1994 Solid State Commun. **92** 149
- Sommerfeld A 1949 *Partial Differential Equations* (Academic Press, New York)
- Tan WC, Preist TW, Sambles JR and Wanstall NP 1999 Phys. Rev. B. **59** 12661
- Tan WC, Preist TW, Sambles JR, Sobnack MB and Wanstall NP 1998 J. Opt. Soc. Am. A. **15** 2365
- Tang C and VanSyke S 1987 Appl. Phys. Lett. **51** 913
- Tang CW, VanSlyke SA and Chen CH 1989 J. Appl. Phys. **65** 3610
- Tessler N 2000 Appl. Phys. Lett. **77** 1897
- Tomas MS and Lenac Z 1997 Phys. Rev. A **56** 4197
- Tomas MS and Lenac Z 1993 Opt. Comm. **100** 259
- Tsutsui T and Yamamoto K 1999 Jpn. J. Appl. Phys. **38** 2799
- Wasey JAE and Barnes WL 2000 J. Mod. Opt. **47** 725
- Wasey JAE, Safanov AN, Samuel IDW and Barnes WL 2000 submitted to Phys. Rev. B
- Wasey JAE, Safonov AN, Samuel IDW 2000 Opt. Comm. **183** 109

and Barnes WL

- | | | |
|---|------|----------------------------------|
| Welford KR and Sambles JR | 1988 | J. Mod. Opt. 35 1467 |
| Windisch R, Heremans P, Knobloch A,
Kiesel P, Dohler GH, Dutta B and
Borghs G | 1999 | Appl. Phys. Lett. 74 2256 |
| Wood EL, Sambles JR, Cotter NP and
Kitson SC | 1995 | J. Mod. Opt. 42 1343 |
| Yablonovitch Y | 1987 | Phys. Rev. Lett. 58 2059 |
| Yeung MS and Gustafson TK | 1996 | Phys. Rev. A 54 5227 |

Appendices

A) From chapter 2. The values R and T are given by

$$R_{//,\uparrow} = \frac{r_{12}(r_{13}e^{2in_1t} \pm 1)}{1 - r_{12}r_{13}e^{2in_1d}} \quad (\text{A1})$$

$$R_{//,\downarrow} = \frac{r_{13}(r_{12}e^{2in_1b} \pm 1)}{1 - r_{12}r_{13}e^{2in_1d}} \quad (\text{A2})$$

$$T_{//,\downarrow} = \frac{t_{12}(1 \pm r_{13}e^{2in_1t})}{1 - r_{12}r_{13}e^{2in_1d}} \quad (\text{A3})$$

$$T_{//,\uparrow} = \frac{t_{13}(1 \pm r_{12}e^{2in_1b})}{1 - r_{12}r_{13}e^{2in_1d}} \quad (\text{A4})$$

where $n_1 = \sqrt{\varepsilon_1 k_0^2 - u^2}$, and u is the in-plane wavevector, and the subscript s or p (which denotes the polarisation) has been dropped, and the t_{ij} and r_{ij} are the Fresnel reflection and transmission coefficients of the appropriate polarisation (defined in section 2.2.4), and the \pm sign corresponds to the $//$ and \perp dipole orientations respectively.

B) From chapter 4, referring to birefringent materials. Amplitude reflection and transmission coefficients for s and p polarised light incident on an interface, travelling from region a towards region b , are conveniently expressed in terms of the wavevector component normal to the plane and the relative permittivities. For p polarised radiation we consider the amplitude coefficient for the \mathbf{H} field, and for the s polarisation we consider the amplitude coefficient of the \mathbf{E} field. They are given by,

$$r_{s,ab} = \frac{n_{sa} - n_{sb}}{n_{sa} + n_{sb}} \quad (\text{B1})$$

$$t_{s,ab} = \frac{2n_{sa}}{n_{sa} + n_{sb}} \quad (\text{B2})$$

$$r_{p,ab} = \frac{n_{pb}\epsilon_{a//} - n_{pa}\epsilon_{b//}}{n_{pb}\epsilon_{a//} + n_{pa}\epsilon_{b//}} \quad (\text{B3})$$

$$t_{p,ab} = \frac{2n_{pa}\epsilon_{b//}}{n_{pb}\epsilon_{a//} + n_{pa}\epsilon_{b//}} \quad (\text{B4})$$

where the n_{si} and n_{pi} have been defined previously (equations (4.10) and (4.26)).

The values A and B are then given by,

$$A_{//,\perp\uparrow} = \frac{r_{12}(r_{13}e^{2ik_0n_1t} \pm 1)}{1 - r_{12}r_{13}e^{2ik_0n_1d}} \quad (\text{B5})$$

$$A_{//,\perp\downarrow} = \frac{r_{13}(r_{12}e^{2ik_0n_1b} \pm 1)}{1 - r_{12}r_{13}e^{2ik_0n_1d}} \quad (\text{B6})$$

$$B_{//,\perp\downarrow} = \frac{t_{12}(1 \pm r_{13}e^{2ik_0n_1t})}{1 - r_{12}r_{13}e^{2ik_0n_1d}} \quad (\text{B7})$$

$$B_{//,\perp\uparrow} = \frac{t_{13}(1 \pm r_{12}e^{2ik_0n_1b})}{1 - r_{12}r_{13}e^{2ik_0n_1d}} \quad (\text{B8})$$

where the subscript s or p , which denotes polarisation, has been dropped, and the t_{1j} and r_{1j} are the reflection and transmission coefficients of the appropriate polarisation, defined above (equations B1-B4), and the \pm sign corresponds to the $//$ case and the \perp case respectively. The value d is given by $d=t+b$.